
EXPERIMENTS WITH BOSE-EINSTEIN CONDENSATES
IN OPTICAL TRAPS

Giuseppe Smirne

A thesis submitted in partial fulfilment of
the requirements for the degree of
Doctor of Philosophy at the University of Oxford



Balliol College
University of Oxford
Hilary Term 2005

ABSTRACT

Experiments with Bose-Einstein Condensates in Optical Traps

Giuseppe Smirne, Balliol College, University of Oxford
D.Phil thesis, Hilary Term 2005

This thesis presents an account of experimental investigations performed on a Bose-Einstein condensate (BEC) of ^{87}Rb atoms trapped in an optical potential. The BEC itself is created by evaporative cooling in a Time-Orbiting Potential magnetic trap, in which more than 10^5 atoms are cooled to temperatures below 300 nK in about one minute.

The arrangement for two kinds of optical trap for neutral atoms is described: a standing wave, which creates a 1-D optical lattice, and a crossed-beam optical dipole trap. These two systems are used in the investigation of a Feshbach resonance that occurs in ^{87}Rb at magnetic field strengths of 1007 G. This resonance is identified and information on the rate of three-body collisions in a BEC in the vicinity of the resonance is extracted and compared with the theory.

The presence of a Feshbach resonance provides a tool with which to control the strength of the interatomic interactions, opening the way to a wide range of applications from atomic and molecular physics to quantum information processing.

In the vicinity of this specific Feshbach resonance the dependence of the rate of three-body collisions with the magnetic field was investigated. The tunability of the interactions can be exploited in order to associate ultracold atoms into diatomic molecules. In order to investigate this possibility, the losses of atoms from the BEC while ramping the magnetic field across the resonance were measured and results in this direction are presented. No conclusive evidence of molecule formation is observed, and we find the most likely cause of this to be the limitations of the experimental apparatus. The validity of the experimental approach, however, was demonstrated in the meantime by another group who successfully made molecules with a slightly different apparatus.

ACKNOWLEDGEMENTS

The last three years have been full of important events in my life, and all of these contributed, in my opinion, to help me get through the research that led to this thesis. For these reasons there are many people to whom I feel indebted with gratitude. I must start the list of people I want to acknowledge with a thought and a dedication to my mum. After having supported and encouraged me through my studies in Pisa, she expressed the natural desire that all these efforts would not be in vain and that I should try to work as a physicist. The wish not to let her down encouraged me to keep up with it, therefore this thesis is also dedicated to her memory.

Now I want to thank all those people who have helped, in many different ways, during these three years. I must start by thanking my supervisor Prof. Chris Foot for the opportunity to work on an interesting experiment, for the many useful discussions, and for having proof read the whole manuscript of this thesis, giving numerous and helpful comments and suggestions.

These years at the Clarendon Laboratory have been important in my education as a physicist, and I am greatly indebted to the three post-docs with whom I was fortunate enough to share the challenge of the research and who taught me so many things. I must start by saying thank you to Rachel Godun for the infinite patience with which she has for three years corrected my English, described English customs, and explained physics (again and again!). Donatella Cassettari welcomed me on my arrival to Oxford, and together we have had many physics discussions and long data taking afternoons and evenings all of which have been an invaluable source of learning. I must thank her also for having rescued the experiment from a *rather large accident!* Vincent Boyer joined us in the summer of my first year in Oxford, and ever since has been a source of ideas, as well as a lunch companion for a few months. I must also thank the three of them for reading different chapters of my thesis and for giving me many important and helpful comments.

All this work would not have been possible without the skilful contribution of the Clarendon Laboratory technical staff. Therefore a big thank you goes to Graham Quelch, our technician, to both the research and mechanical workshops, to Chris Goodwin for making our special mirrors, and to David Smith for the electronic components.

I am grateful to the BEC people in the Clarendon Laboratory, both theorist and experimentalists, for having contributed to make the daily routine lighter through

their cheerful mood at tea-breaks and for the many helpful physics discussions. Starting with the basement people who, at different times, have been here during these years, I thank Onofrio Maragò, who encouraged me to apply to come to study in Oxford, Nathan Smith and Zhaoyuan Ma who have shared the office with me, and Zhaoyuan also for having taught me some Chinese words, luckily now I remember the most important: xie xie (thank you!). Then Michael d'Arcy, who has been an excellent mentor at Balliol College and football team captain, Chandrashekar, Eleanor Hodby, Angharad Thomas, Simon Cornish, Andrian Harsono, Will Heathcote, Eileen Nugent, Gerald Hechenblaikner, Gil Summy, Peter Baranowski, Min Yoon, Amita Deb, all for making the basement such a lively and friendly place. From the theory-top-floor people I must start with the two *dot-tori* Thorsten Köhler and Krzysztof Góral, whom I have to thank for providing me with some theoretical plots, for long interesting discussions, and Thorsten also for having read the theoretical parts of my thesis giving invaluable comments and explanations. A big thanks also to the other members of the KBG who have often contributed to relaxing tea-breaks. I want to acknowledge also Oliver Morsch, in Pisa, for having always been available, since the time of my application, for advice, encouragement, and useful discussions. I would also like to thank my tutor in Balliol College, Dr. Jonathon Hodby for his guidance and for giving me the opportunity to demonstrate on his practical course of Electricity and Magnetism.

My time in Oxford would not have been so enjoyable without being a member of the Balliol College MCR. So I must thank the whole Holywell Manor community and the very friendly and helpful porters who have always tried to make our students life easier. But the biggest thank you goes to the Holywell Manor Italian Society: Rachel Ahern (a.k.a. la Consigliera), Isabelle Avila (Apo), Victor Campbell (Don Vito), Leonora Fitzgibbons, Fok-Shuen Leung (Falcon), Alan Smillie, Alessandro Tricoli (GF111), and Paul Yowell. With them all I share memories of nice Sunday afternoons spent watching Italian movies and eating Italian food. Again on the Italian side, gratitude goes to Mariella and Edward Bliss for their warm friendship (and delicious Italian dinners!). I want to thank also my sisters, Nicoletta and Stefania, my brother in law Giuseppe, and my two lovely little nieces Claudia and Camilla for their love and for making my holidays in Calabria so relaxing. The same gratitude goes to Arianna's family for being supportive and for the holidays in Tuscany.

And now I must come to the one acknowledgement that I feel I owe the most, and this is to my wife Arianna, for having always believed that I would get to the end of this thesis even when I didn't believe it myself. And more importantly, for putting up daily with me when I was particularly moody, for her sacrifices, for having visited me in Oxford so often before our wedding and for having come to a foreign country to stay with me for a year and a half now, after becoming my wife, and for having succeeded in settling down and learning the language at a speed that amazes me every day. But most of all for her daily smiles and constant love,

that have been a real source of energy to keep me working. For all these reasons she must share the dedication with which I started these acknowledgments, and my thanks and love will never be enough.

I also acknowledge financial support for my studies from the EU through the Cold Quantum Gases Research Network.

*The search for truth is more precious than its possession.
Everything should be made as simple as possible, but not simpler.*
Albert Einstein

CONTENTS

1	Introduction	1
1.1	Bose-Einstein Condensation	1
1.2	Making cold molecules	3
1.3	Overview of our approach	5
1.4	Thesis layout	6
2	Theoretical foreword	9
2.1	Laser cooling techniques	9
2.1.1	Optical molasses	10
2.2	The Magneto-Optical Trap	11
2.3	Magnetic Trapping	12
2.3.1	TOP trap	13
2.3.2	Effect of gravity	15
2.4	Dilute Bose gas in a harmonic trap	16
2.4.1	The ideal Bose gas	16
2.4.2	Theory of a weakly interacting Bose gas	18
2.5	Evaporative cooling	19
2.5.1	Radio frequency evaporation	20
2.5.2	Evaporation in a TOP trap	21
2.6	Optical trapping	22
2.6.1	1D Optical Lattice	24
2.6.2	Crossed-beam dipole trap	26
2.7	Feshbach resonances	27
2.7.1	Feshbach Resonances in ^{87}Rb	29
2.8	Formation of ultracold molecules exploiting a Feshbach resonance	30
2.8.1	Landau-Zener approach	32
3	Experimental apparatus	37
3.1	Vacuum system	37
3.1.1	Rubidium dispensers	39

3.2	Laser sources	40
3.2.1	Master lasers	40
3.2.2	Frequency stabilization	41
3.2.3	Slave lasers	42
3.3	Optical bench layout	43
3.4	Magnetic fields	46
3.4.1	Pyramid quadrupole	46
3.4.2	Shim coils	47
3.4.3	TOP coils	48
3.4.4	RF coils	49
3.4.5	Quadrupole and Feshbach bias field coils	49
3.5	Pyramid MOT	56
3.6	Science MOT	58
3.7	Imaging system	59
3.7.1	Absorption pictures	62
3.7.2	CCD camera	62
3.7.3	Magnification and calibration	63
3.8	Computer control	63
4	Obtaining BEC	65
4.1	Loading the TOP trap	65
4.1.1	Mode matching	66
4.1.2	Optical molasses	67
4.1.3	Optical pumping	68
4.1.4	Parameters of the initial trap	70
4.2	Evaporative path to BEC	71
4.2.1	Increasing the collision rate	72
4.2.2	Evaporation with the rotating potential	72
4.2.3	Radio-frequency evaporation	73
4.3	Additional measurements with the BEC	74
4.4	Summary	76
5	1-D Optical lattice	77
5.1	The standing wave	77
5.2	Alignment procedure	80
5.3	Loading of the atoms into the lattice and lifetime	81
5.4	Measurement of the depth of the lattice	83
5.5	Measurement of the radial trap frequencies	85
5.6	Summary	86

6	Crossed-beam dipole trap	87
6.1	The horizontal beam	87
6.2	Alignment procedure	89
6.3	Loading parameters and lifetime of the trap	89
6.4	Measurement of the trap frequencies	90
6.4.1	The effect of gravity	92
6.5	Summary	93
7	Observing a Feshbach resonance	95
7.1	RF transfer	95
7.2	Localizing the resonance	97
7.3	Measurement of the 3-body loss rate	99
7.4	Summary	102
8	Search for Molecules	103
8.1	Introduction	103
8.2	Burst ramps	106
8.3	Molecular ramps	108
8.4	Separation methods	111
8.4.1	Diffraction	111
8.4.2	Stern-Gerlach experiment	112
8.5	Experimental protocols	113
8.6	Limitations of the experimental setup	115
8.7	Summary	116
9	Conclusions and outlook	117
A	Rubidium data	121
B	Image analysis	123
C	Calculation of the number density per lattice well	125
D	Stabilization of the magnetic field	129

Introduction

The experimental work presented in this thesis lies at the boundary of two important topics in atomic and laser physics: Bose-Einstein Condensation (BEC), and the production and study of molecular quantum gases. Bringing the two topics together means being able to exploit the unique properties of Bose-Einstein condensates to gain deeper insight into the physics of atom-atom interaction and molecular physics. In this chapter I will briefly introduce the two subjects, and then give an overview of our approach on how to create molecules starting from an atomic condensate.

1.1 Bose-Einstein Condensation

Although it is a relatively recent experimental research field, BEC is already a very well studied property of bosonic particles, and its first experimental achievement in 1995 [1] opened an entirely new era in atomic physics. Since then, this field has drawn the attention of a large portion of the scientific community working on atomic physics, and the important achievements of this community have been acknowledged with two Nobel prizes awarded to six of the pioneering contributors. This section, although dedicated to BEC, is far from being a complete review of the techniques and concepts involved; these are described more fully in [2] and [3].

The phenomenon of BEC was predicted in 1925 when Albert Einstein [4] extended a study published the year before by S. Bose [5] on Planck's law of black-body radiation, to describe a peculiar behaviour of all bosons (i.e. also those with a mass, and not only photons as in Bose's study), by which, below a certain temperature, they accumulate in the lowest energy state. Einstein's result was derived from the laws of statistical mechanics and, although well defined in theory, some scepticism as to its practical realization was advanced even by Einstein himself.

For about 20 years the phenomenon was almost entirely neglected by the scientific community, until Bogoliubov in 1947 [6] established a connection between BEC and superfluidity in *liquid* helium, which had already been predicted by F. London [7] nine years earlier. The strong interactions present in this system, however, greatly complicate the phenomenon in *liquid* helium, so that the simple theory of the ideal gases could not be applied. In the case of ideal gases the theory predicted that the population of the ground state of the system is macroscopically populated when the deBroglie wavelength λ_{dB} associated with the particles becomes comparable to the separation between them. The threshold of quantum degeneracy was predicted to occur, for an ideal gas, when:

$$\rho = n\lambda_{\text{dB}}^3 = 2.612 \quad (1.1)$$

where ρ is the phase space density, and n is the number density of the gas. In the kinetic theory of the gases the thermal deBroglie wavelength can be expressed as:

$$\lambda_{\text{dB}} = \frac{h}{\sqrt{2\pi mk_B T}} \quad (1.2)$$

where h is Planck's constant, m is the mass of one particle, and T is the temperature of the gas.

For a gas at room temperature the phase space density is much smaller than 2.612, and compressing the gas does not help because at high densities the interactions are so strong that ordinary condensation occurs long before reaching the quantum degeneracy. The research, therefore, moved towards dilute gases with simple interactions. The first gas to be involved in experiments of this kind was spin polarized atomic hydrogen, which was cooled down using cryogenic techniques. The phase space density did not go above 0.05 in those experiments because of three-body recombination, and this prevented the atomic gas from reaching quantum degeneracy [8].

The group at MIT had to work for 12 years before they observed a condensate of hydrogen [9]. The key elements that made this further step possible were the development of magnetic trapping and evaporative cooling techniques. In the meantime laser cooling techniques were developed for alkali atoms, that allowed caesium atoms to be cooled to temperatures of the order of a few μK without the constraints of cryogenic techniques. The combination of laser cooling, magnetic trapping, and evaporative cooling led to the real breakthrough of obtaining BEC in a weakly interacting alkali gas. In this type of experiments, atoms were first collected and cooled in a magneto-optical trap (MOT) [10]; subsequent transfer into a magnetic trap, where they were further cooled by means of radio frequency evaporation [11], allowed the first three alkali atoms (Rb, Na, Li) to be condensed [1, 12, 13] in 1995, 70 years after Einstein's prediction of the phenomenon.

Since those initial experiments, the field has grown rapidly and, to date, over 40 BECs have been produced worldwide. The technique used to obtain condensates

initially was based on evaporative cooling in a magnetic trap, while now BEC produced using all-optical traps are becoming more and more common. Condensates have been obtained with several different atomic species: H, He*, ^7Li , ^{23}Na , ^{41}K , ^{85}Rb , ^{87}Rb , ^{133}Cs , and recently, ytterbium [14] and chromium, which have both been condensed by means of evaporation in a crossed-beam dipole trap.

Making a BEC means having a source of coherent atoms, in the same way as developing a laser means having a source of coherent photons. The coherence of the atoms accumulated in the lowest energy state of the trap implies that they evolve together with a definite phase and therefore can be described by a single wave function. Since 1995, BEC has found many diverse applications in different directions such as coherent atom optics, many-body physics (superfluidity), quantum computing, and molecular quantum gases.

I shall list here some crucial experiments which have been possible since the achievement of BEC. Atoms from a condensate have been made to diffract and to interfere [15, 16] in the same way as laser light does. In the early days, the macroscopic properties of the condensates were among the main subjects of investigation. Various types of continuous and pulsed atom lasers have been demonstrated [16, 17, 18, 19]. The superfluid nature of the condensates has been studied as well as the propagation of sound and creation of vortices inside the condensate [20, 21, 22, 23]. BEC loaded into a 3-D lattice has been used to realize the quantum transition to a Mott insulator phase [24]. Studies have been made in many different directions, and many more are currently being pursued. Properties of condensates trapped in an array of optical traps are studied in view of a future realization of logic gates for quantum computation [25]. Far from being complete, this list of experiments, that has meant to explore the potential of this rapidly growing field, gives just the flavour of the ferment that is still, after nearly ten years, animating the field.

A remarkable achievement recently has been the observation of BEC made with molecules of $^{40}\text{K}_2$ and $^6\text{Li}_2$ at the crossover of the BCS-BEC regimes [26, 27, 28]. Among the motivations behind this research there is the interest that atomic physicists have always had in molecular gases and, with the advent of BEC, in molecular quantum gases.

1.2 Making cold molecules

Condensation of molecules cannot be obtained by applying the same techniques that are used with atoms, due to the complex internal vibrational and rotational structure. What is possible, however, is to create molecules from atoms that have already formed a condensate.

The formation of cold molecules is an older research field than BEC. Photo-association (PA) of ultra-cold atoms, proposed in 1987 [29], revealed a powerful tool to improve spectroscopic measurements, by creating molecules with low trans-

lational velocity ($\simeq 10$ mK), which permits high-resolution free-bound molecular spectroscopy. The molecular states near the dissociation limit, that could not be explored by traditional methods, are accessible with this technique. When applied to a MOT of sodium atoms in 1993, it proved successful in exploring long-range molecular states near the dissociation limit, thanks to the high resolution of the spectra obtained with low kinetic energy (≤ 1 mK) collisions [30]. These spectra can be used to deduce atomic lifetimes and atomic ground-state scattering lengths (among other things). At the beginning of 2000, at the University of Texas, PA of molecules from atoms in a BEC, with temperatures of the order of 100 nK, improved the precision of the measurement of binding energies by 4 orders of magnitude compared to any other previous measurement [31].

We will now look, in simple terms, at how cold molecules can be formed. This description will serve to introduce some terminology, and show that intrinsically, behind the process, there are at least two ways of making cold molecules: using photo-association, as outlined in this section, or with the assistance of a Feshbach resonance, as introduced in the next section, which is the one adopted in this research (and is described further at the end of the next chapter).

The collision between two free atoms is the central process needed to make molecules. When photo-association is used, the absorption of light induces the formation of the molecule. A schematic description of the process is given in fig. 1.1. The pair of ground-state free atoms has potential energy described by the asymptotic value of the ground-state molecular potential that varies as $V = -C_6R^{-6}$. For large internuclear distances this van der Waals potential has decayed and become effectively flat. Under the influence of the laser light, one of the two atoms is promoted to the excited state, so that the coupling is now dominated by the long range resonant dipole interaction varying as $V = -C_3R^{-3}$, and therefore becoming flat at much larger distances than the ground state potential. For a given frequency of the photo-associating laser (but lower than the separation of the two long-range asymptotes), the transition happens, in a semiclassical picture, around a distance R_C , called the Franck-Condon point. There the energy of the radiation equals the energy gap between the ground state potential curve and a bound state of the excited level. The bound atom pair can then decay to produce two untrapped hot atoms or a bound ground-state molecule (dashed line in the picture).

Photo-association for colliding neutral atoms had been used already before the advent of laser cooling, but its usefulness as a spectroscopic tool was very limited by the large thermal energy of the colliding free-atoms. The spread in the collisional energy is of the order of the thermal energy of the colliding pair, which for room temperature is about 10 THz. This is very large even compared to the Doppler widths ($\simeq 1$ GHz), while for laser cooled atoms the thermal energy can be reduced to below the natural line width of free atoms, making the resolution of free-bound spectroscopy comparable with that of bound-bound spectroscopy. The

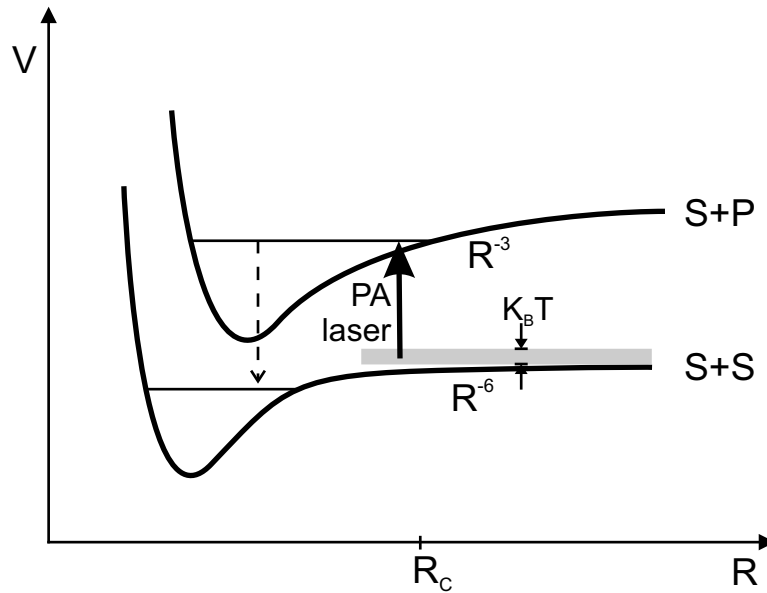


Figure 1.1: Schematic of the photo-association process in which a free ground-state pair of atoms gets promoted to a bound state of the excited molecular potential around the Condon point R_C .

additional advantage of free-bound spectroscopy with laser cooled atoms is that also purely long-range states can be observed as well as other states very close to the dissociation limit, which makes this technique very suitable to measure scattering properties and parameters.

The theory outlined above is taken mainly from a review paper by Paul Lett et al. [32], to which the reader should refer for further details and references.

1.3 Overview of our approach

The mechanism by which the PA of two atoms produces a molecule is better understood in the interaction configuration picture: the energy of the bound state in the excited molecular potential comes into resonance with the energy of two ground state atoms which collectively absorb a photon and form a bound excited-state dimer; this may eventually decay to two untrapped atoms or to a bound ground-state molecule. Two-photon or Raman spectroscopy can also be used to produce doubly excited or ground-state molecules.

A similar description applies to the formation of molecules in the electronic ground state using a Feshbach resonance. Details of the production mechanisms will be given in section 2.8, but the general idea is briefly introduced here.

In the presence of a magnetic field, the relative difference in energy between the s-wave potentials, sketched in fig. 1.2, varies in such a way that the energy of

the free atom pair in the incident channel can become resonant with the energy of a bound level of the molecular potential. When this happens, coupling due to intrinsic spin-dependent forces can form a quasi-bound dimer. This, by further tuning of the magnetic field, can be brought into resonance with the first bound state of the incident channel to form a ground state molecule. This type of resonance is called a Feshbach resonance, to distinguish it from the optical resonances where the coupling is optically induced as in PA. A main difference is that the two potential curves labelled F_a and F_b in fig. 1.2 correspond to two different hyperfine levels of the ground state and not two electronic levels as in PA, therefore their energy difference is much smaller and resonances can be found for relatively small DC magnetic fields.

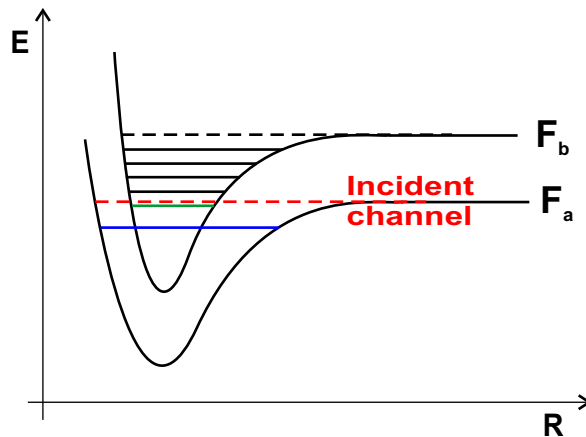


Figure 1.2: Schematic of interatomic potentials involved in the formation of molecules via a Feshbach resonance. F_a and F_b are the two different hyperfine states involved in the resonance.

Experimentally, we start with a sample of about 10^5 ^{87}Rb atoms that form a Bose-Einstein condensate, so that their translational energy is minimum, and then we trap them in an optical potential where the atoms are spin-flipped into the hyperfine state $|F = 1, m_F = +1\rangle$, which cannot be magnetically trapped, and where the occurrence of a Feshbach resonance has been predicted and demonstrated [33, 34]. The atoms thus trapped are exposed to a uniform magnetic field which, for a specific value, generates the resonance that is exploited for the formation of molecules. The different techniques explored in this research for the production and detection of ultracold molecules are discussed in the next chapter.

1.4 Thesis layout

The second chapter gives an overview of the theory behind most of the experimental techniques adopted in this research; further references that will provide more

complete accounts of the subjects examined will be given where necessary in later chapters.

The third chapter describes the setup used to acquire the experimental measurements. It gives a detailed account of some of the equipment employed, pointing out the technical limitations of the apparatus.

Chapters 4 through to 8 present the experimental results. Each of the five chapters describes a different step towards the association of molecules from an optically trapped BEC. Chapter 4 describes the different stages that led, during the first few months of this experimental work, to the creation of a ^{87}Rb BEC. Chapter 5 and chapter 6 describe the alignment of a 1-D standing wave and a crossed optical dipole trap respectively, and their main features as optical traps for our condensates. Chapter 7 is dedicated to the search and measurements of a Feshbach resonance at about 1000 G, and it also describes our determination of the three-body collision rate constant close to the resonance. Finally, chapter 8 describes the study performed on the effect of the magnetic field being swept up and down through the resonance in the search for evidence of molecule formation, and the reasons why this search did not provide direct observations are discussed. Conclusions of this work are given in chapter 9 and what has been learned from this experimental work is summarized. Future prospects are also outlined.

There are four appendices at the end of the thesis: appendix A contains some physical information on ^{87}Rb , relevant to this thesis; appendix B explains how we extract the information from the images of our atom clouds; appendix C reports how the density of atoms in the standing wave is obtained; and, lastly, appendix D is dedicated to the magnetic field stabilization electronics.

Theoretical foreword

This chapter provides the theoretical basis for the experimental work described in the rest of this thesis. The laser cooling techniques that we employed are a standard tool in this field, and are briefly reviewed in the first two sections. Magnetic trapping and evaporative cooling are also well known techniques, and hence, sections 2.3, 2.4, and 2.5 just go through the basic concepts, in order to introduce the necessary formalism for the experimental chapters.

The last three sections give a more detailed analysis of features of the experiments. Section 2.6 reviews optical trapping techniques, paying particular attention to the two kind of optical traps employed in this research: the 1-D optical lattice and the crossed-beam dipole trap. The last two sections deal with the physics of Feshbach resonances and their use in making cold molecules from a BEC.

2.1 Laser cooling techniques

Laser cooling was conceived around 1975 by Hansch, Schawlow, Wineland, Dehmelt and Itano [35, 36, 37] as a way of producing samples of gases at temperatures well below those achievable with cryogenic techniques. The interaction between atoms in a gas and the photons in a beam of laser light, through a succession of absorptions and spontaneous emissions, can reduce the mean velocity of the gas resulting in a lower energy.

Strictly speaking, to be able to talk about *temperature*, it is necessary to have a closed system in thermal equilibrium with a thermal bath. In laser cooling the role of the thermal bath is played by the photons. Although they do not give the thermal contact and heat exchange required, the reduction of the entropy of the system is achieved at the expense of the entropy of the photons. Therefore, although it is not very rigorous, the use of the term temperature is a convenient way to characterize the width of the Maxwell-Boltzmann velocity distribution.

Two main temperatures can be identified in laser cooling. The first is the Doppler temperature, related to the natural width of the atomic transition Γ (FWHM), involved in the cooling process:

$$k_{\text{B}}T_{\text{D}} \equiv \frac{\hbar\Gamma}{2} \quad (2.1)$$

where k_{B} is Boltzmann's constant. This gives the lowest temperature that can be achieved with a simple laser cooling scheme for a two-level atom. However, experimental evidence was found that temperatures lower than this Doppler limit could be achieved; the mechanisms leading to sub-Doppler cooling were explained by Dalibard and Cohen-Tannoudji [38]. The key feature of their models, which were able to describe the cooling processes more accurately, was to take into account the fact that alkali atoms are not two level atoms, but have a more complex hyperfine structure and Zeeman magnetic sub-levels. Once these structures are included in the theory, optical pumping among the different levels explains the new cooling mechanisms.

The second temperature is the one associated with the recoil of a single photon via the relationship:

$$k_{\text{B}}T_{\text{r}} \equiv \frac{\hbar^2 k^2}{M}. \quad (2.2)$$

This is as cold as you can get for a specific atom of mass M interacting with a photon of wavenumber k in the simple scheme of absorption and emission of standard laser cooling. Two velocity-selective schemes have been devised, however, which overcome this limit by making use of dark states [39] and Raman transitions [40].

The scheme adopted to perform laser cooling in this thesis is one of the models described in [38], and specifically it makes use of three pairs of laser beams with orthogonal circular polarization that generate a polarization gradient; the total electric field is linearly polarized and uniform in time, but rotates in space around the propagation axis over the period of a wavelength. As an atom moves through such a light field, and for negative frequency detunings of the beams, its quantization axis rotates and the atoms are optically pumped to sub-levels with lower energy. This model provides also the equilibrium temperature for these sub-Doppler cooling mechanisms which, in the limit $|\delta| \gg \Gamma$, where $\delta = \omega_L - \omega_0$ is the angular frequency detuning of the laser frequency ω_L from the resonant frequency ω_0 of the transition, is found to be

$$k_{\text{B}}T \simeq 0.1 \frac{\hbar\Omega^2}{|\delta|}. \quad (2.3)$$

2.1.1 Optical molasses

When an atom absorbs a photon with a given wavevector \vec{k} from a laser beam, it receives a kick in the direction of propagation of the photon, of momentum $\hbar\vec{k}$.

Over a large number of successive absorption/spontaneous emission processes, and because spontaneous emission averages to zero, the net effect on the atom is a force pushing it in the direction of the travelling photons.

If the photon has red frequency detuning from the resonance of the atomic transition, it will be Doppler shifted towards resonance when the atom is moving towards the incoming photon, and away from resonance when it is moving in the same direction of the photon. This way, atoms moving towards a red detuned laser beam are slowed down with a force $\vec{F} = \hbar\vec{k}\gamma$, where the scattering rate γ depends on the natural linewidth Γ of the transition through the Lorentian relationship

$$\gamma = \frac{\Gamma}{2} \frac{s_0}{1 + s_0 + [2(\delta + \omega_D)/\Gamma]^2}, \quad (2.4)$$

where $\omega_D = -\vec{k} \cdot \vec{v}$ is the Doppler shift seen by the atom, and s_0 is the saturation parameter given by the ratio of the light intensity I and the saturation intensity I_s of the transition. The force reaches its maximum value $\vec{F}_{\max} = \hbar\vec{k}\frac{\Gamma}{2}$ as $I \rightarrow \infty$. For a derivation of all these expressions see [41].

It is clear that if 3 pairs of counter-propagating beams are used, all having a red frequency detuning δ , whichever is the direction in which the atom is moving, it will find photons Doppler shifted to the resonance of the transition and will absorb them, thus being slowed down in all directions. As a result, the atom finds itself in a viscous medium that reduces its velocity down to a few cm/s compared to ~ 240 m/s of room-temperature rubidium atoms. This technique, named optical molasses, was first demonstrated in 1989 [42].

2.2 The Magneto-Optical Trap

The Magneto-Optical Trap (MOT), which is the starting point of most BEC experiments with alkali atoms as the pre-cooling and trapping mechanism (among other numerous applications), was first demonstrated in 1987 [10]. It provides a trap capable of accumulating billions of atoms, after which the magnetic field is turned off to leave the atoms in optical molasses, where sub-Doppler cooling mechanisms lower their temperature.

The scheme of the MOT is shown in fig. 2.1. It makes use of three pairs of laser beams of opposite circular polarization σ^+/σ^- , and of a magnetic field gradient provided by a pair of anti-Helmholtz coils.

At the middle of the trap the net radiation force acting on the atoms is zero; away from the centre the Zeeman shift of the magnetic sub-levels creates an imbalance in the radiation pressure exerted by the σ^+ and σ^- waves. The simple 1D scheme of fig. 2.2 considers a cooling transition between hyperfine levels with $F = 0$ and $F = 1$. The Zeeman shift along the direction of the beams (z) is given by:

$$\Delta E_{m_{F,e}}(z) = \mu_B g_F m_{F,e} B(z) \quad (2.5)$$

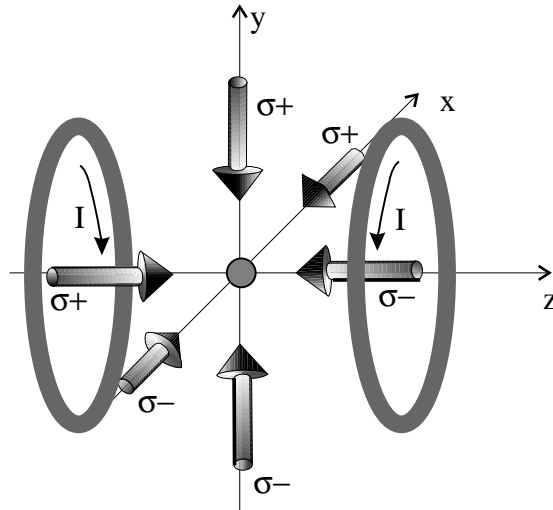


Figure 2.1: The Magneto-Optical Trap.

where μ_B is the Bohr magneton and g_F is the Landé g-factor. From the relationship 2.5 it follows that for $z > 0$ and $\delta < 0$ the atom absorbs preferentially from the σ^- beam and is pushed towards the centre of the trap. For $z < 0$ the same is true with the σ^+ beam. The magnetic field gradient introduces a dependence of the magnitude of the Zeeman shifts on the coordinate z , thus giving spatial confinement.

2.3 Magnetic Trapping

BEC has not yet been achieved by means of laser cooling only, but evaporative cooling in a magnetic trap has proven to be a very powerful technique to bring the energy of the atoms down to the threshold for BEC and beyond. The advantage of this technique with respect to laser cooling is that there is no lower limit, due to photon recoils, to the temperatures achieved for the trapped atoms.

Although there are many configurations of magnetic traps, they can be broadly divided into two main classes: the Time-Orbiting Potential (TOP) and Ioffe-Pritchard traps. A description of both can be found in [43]. Here I will only describe the one that has been used for this research, namely the TOP trap.

Why can we trap atoms in a magnetic potential, and what quantum states can we trap? To answer the first question we have to consider the Zeeman effect. The Zeeman splitting of the magnetic hyperfine levels for weak fields (that give splittings small compared to the hyperfine structure (hfs)) varies linearly with the field, and the proportionality constant is the component of the magnetic moment of the atoms along the direction of the field. The magnetic energy can be expressed as $U = -\vec{\mu} \cdot \vec{B} = g_F \mu_B m_F B$. When the component of the magnetic moment

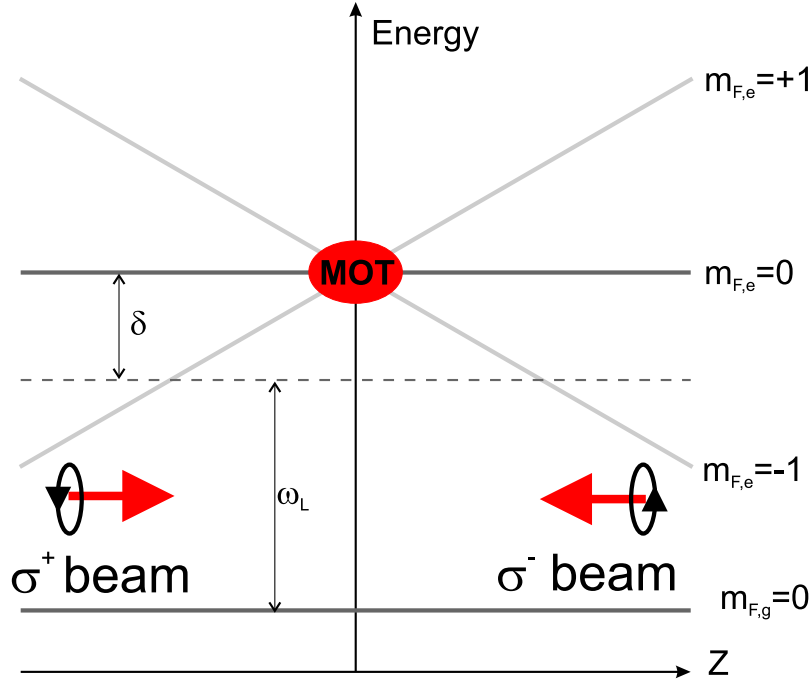


Figure 2.2: Energy diagram illustrating the MOT's cooling and trapping scheme. The indices g and e indicate the ground and the excited level respectively.

of the atoms along the direction of the field is positive, the atoms are driven towards large magnetic fields (*high-field seekers*), while, when it is negative, the atoms are driven towards regions with a lower magnitude of the magnetic field (*low-field seekers*). Since Maxwell's equations do not allow a local maximum in free space for a d.c. magnetic field [44], we need atoms in states where they are low-field seekers, i.e. magnetic states for which $g_F m_F > 0$. The maximum energy the atoms can have in order to be trapped in the magnetic potential depends on the depth of the trap, whose order of magnitude is given by B times the ratio $\mu_B/k_B \simeq 67 \mu\text{K}/\text{G}$ between the Bohr magneton and Boltzmann's constant. In BEC experiments typical magnetic fields value are of the order of 300 G at the border of the trap, therefore a typical depth is of the order of 20 mK, and hence the atoms need to be pre-cooled before being transferred into the magnetic trap.

2.3.1 TOP trap

The TOP trap is obtained by superimposing a rotating uniform magnetic field on a static quadrupole magnetic field. The diagram in fig. 2.3 illustrates a view of the magnetic fields in the TOP trap at a certain instant of time. The geometry of the resulting potential depends on the relative direction of the axis of the quadrupole field and the plane on which the uniform field rotates. With the configuration

adopted in our experiment, where the quadrupole axis is vertical, and the uniform field rotates on the horizontal plane, the contours of the potential, as we shall see presently, has the shape of a pancake with the vertical direction squeezed 8 times more than the horizontal one.

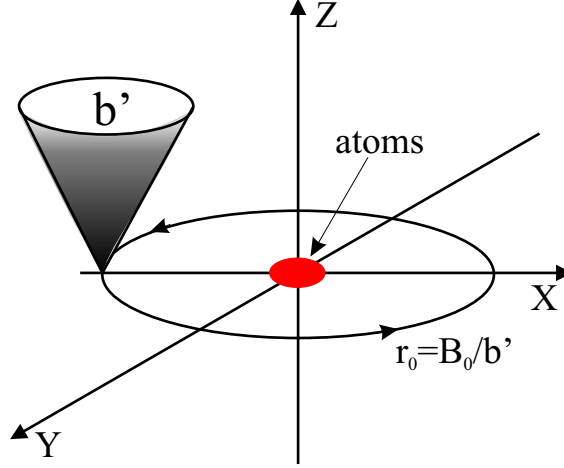


Figure 2.3: Instantaneous diagram of the TOP trap magnetic fields. The circle of radius $r_0 = B_0/b'$ is the locus of $\vec{B} = 0$, hence the atoms are centered in a region with magnetic field amplitude B_0 .

The quadrupole field, near the center of symmetry of the two anti-Helmholtz coils that generate it, has a gradient b' on the horizontal plane, which becomes twice as big along the symmetry axis. It is a perfectly good potential for confining atoms itself, apart from one feature: near the zero of the magnetic field at the centre of the trap Majorana spin flips can transfer the atoms into high field seeking (thus anti-trapped) states (i.e. the field is too weak to maintain the polarization of the atoms). To prevent this, a uniform field of magnitude B_0 is added, which rotates on the horizontal plane, thus moving the zero of the magnetic field dynamically on a circle of radius $r_0 \equiv B_0/b'$.

If the rotating field has components $B_0 \cos \omega_T t$ along x and $B_0 \sin \omega_T t$ along y , the total instantaneous field is:

$$\vec{B} = (b'x + B_0 \cos \omega_T t, b'y + B_0 \sin \omega_T t, -2b'z). \quad (2.6)$$

If we want the atoms to feel an average force pushing them towards the centre of the trap where the magnetic field strength is B_0 , this bias field must rotate at a frequency higher than the frequency ω at which the atoms oscillate in the magnetic trap; hence:

$$\omega_T \gg \omega. \quad (2.7)$$

On the other hand, if we want the magnetic moment of the atoms to follow adiabatically the rotating field, an upper limit to its frequency is imposed by the

Larmor precession frequency $\omega_L = \mu|\vec{B}|/\hbar$, and therefore:

$$\omega_T \ll \omega_L. \quad (2.8)$$

When this second condition is satisfied, the potential energy can be calculated as $U = \mu|\vec{B}|$, with \vec{B} given by eq. 2.6:

$$U(x, y, z, t) = \mu\sqrt{(b'x + B_0 \cos \omega_T t)^2 + (b'y + B_0 \sin \omega_T t)^2 + 4b'^2 z^2} \quad (2.9)$$

If also eq. 2.7 is satisfied, it makes sense to use an effective potential averaged over a period of the rotation of the bias field, from which we can work out the trap frequencies:

$$\bar{U}(x, y, z) = \frac{1}{T} \int_0^T U(x, y, z, t) dt \quad (2.10)$$

where $T = 2\pi/\omega_T$, whence, at the first non-vanishing order in the coordinates:

$$\bar{U}(x, y, z) = \mu B_0 + \mu \frac{b'^2}{4B_0} (x^2 + y^2 + 8z^2) \quad (2.11)$$

which is a harmonic potential whose oscillation frequencies are related to the magnetic field by the following relationships:

$$\begin{aligned} \omega_r^2 &= \mu \frac{b'^2}{2mB_0} \\ \omega_z^2 &= 8\omega_r^2 = 8\mu \frac{b'^2}{2mB_0} \end{aligned} \quad (2.12)$$

where m is the mass of the atom. From the equation 2.11 we can calculate the depth of the trap as the value of the potential along the circle ($r_0 = B_0/b'$, $z = 0$), where the zero of the quadrupole field rotates, and subtracting from this the offset μB_0 . The resulting depth, $\frac{1}{4}\mu B_0$ represents the maximum energy of the atoms that can be trapped.

2.3.2 Effect of gravity

An effect that should be taken into account is the modification of the TOP trap potential due to gravity, by adding the term mgz to the instantaneous potential. To see how the presence of this new term affects the time-averaged potential and the frequencies of the trap it is useful to define the dimensionless parameter $\eta \equiv \frac{mg}{2\mu b'}$, given by the ratio between gravity (pulling the atoms downwards), and the magnetic force (pushing them upwards). Simple maths shows that the presence of gravity causes the position of the minimum of the potential along z to sag from $z = 0$ to the new position

$$z_{\min} = -\frac{r_0}{2} \frac{\eta}{\sqrt{1-\eta^2}} \quad (2.13)$$

where r_0 was defined above. The new oscillation frequencies for the total potential, which includes gravity, can be expressed as a function of the frequencies 2.12 [45]:

$$\begin{aligned}\omega_r^2 &= \omega_{0r}(1 + \eta^2)^{1/2}(1 - \eta^2)^{1/4} \\ \omega_z^2 &= \omega_{0z}(1 - \eta^2)^{3/4}.\end{aligned}\tag{2.14}$$

The expressions given above are included for completeness, although the effect of the parameter η in this experiment is negligible to the purpose of our measurements, and has been ignored when quoting trap frequencies as it modifies the axial frequency (for the conditions from which the condensates are released) by about 0.5% and the radial frequency even less. The gravitational sag is only about 0.4 mm in the weak trap where the atoms are initially loaded, which is small compared to the size of the probe beam.

2.4 Dilute Bose gas in a harmonic trap

This section recalls the main features of the theory of a dilute Bose gas in a harmonic trap that are of interest for this thesis. I will present first the case of an ideal gas with no interactions, and subsequently we shall see how those results are modified in the presence of weak interactions between the atoms.

2.4.1 The ideal Bose gas

An ideal gas of N identical bosons confined in a volume V is described by the Bose-Einstein statistical distribution, which requires, for the level with energy $u = p^2/2m$, a mean occupation number $n(u)$ given by [43]:

$$n(u) = \frac{g(u)}{e^{(u-\mu)/k_B T} - 1}\tag{2.15}$$

where $g(u)$ indicates the density of states, and μ is the chemical potential, which for a Bose gas must be ≤ 0 . It is usual to define a parameter $z = e^{\mu/k_B T}$ called fugacity. This is useful because, in terms of this parameter, we can express the population of the ground state as:

$$N_0 \equiv n(0) = \frac{z}{1 - z}\tag{2.16}$$

which must be added to the number that is obtained from the statistical distribution for $u > 0$. The total number of particles is then [43]:

$$N = N_0 + \frac{V}{\lambda_{dB}^3} g_{3/2}(z)\tag{2.17}$$

where we have $g_n(z) \equiv \sum_{l=1}^{\infty} \frac{z^l}{l^n}$ and λ_{dB} is the de Broglie wavelength defined as $\lambda_{\text{dB}} \equiv \sqrt{\frac{2\pi\hbar^2}{mk_{\text{B}}T}}$. When the chemical potential approaches zero, and hence the fugacity approaches 1, we obtain a relationship between density and temperature that defines a critical temperature below which the population of the ground state becomes macroscopic. This phenomenon is called Bose-Einstein condensation. The critical temperature can be worked out to be:

$$T_c = \left(\frac{n}{g_{3/2}(1)} \right)^{2/3} \frac{2\pi\hbar^2}{mk_{\text{B}}}. \quad (2.18)$$

This expresses a condition on the phase-space density $\rho = n\lambda_{\text{dB}}^3$ that, at the critical temperature, becomes $\rho(T_c) = g_{3/2}(1) \approx 2.612$. Below this temperature the fraction of atoms condensed in the ground state and the fraction of thermal atoms in the excited levels are functions of the temperature only:

$$\frac{N_e}{N} = \left(\frac{T}{T_c} \right)^{3/2} \quad (2.19)$$

$$\frac{N_0}{N} = 1 - \left(\frac{T}{T_c} \right)^{3/2}. \quad (2.20)$$

If the Bose gas is confined in a harmonic potential, the energy levels are those of a 3D harmonic oscillator: $E(n) = \hbar\bar{\omega}(n + \frac{3}{2})$, where $\bar{\omega} = (\omega_x\omega_y\omega_z)^{1/3}$ is the average of the frequencies in the three spatial directions, and $n = n_x + n_y + n_z$ is the 3D harmonic oscillator quantum number. For a gas of N particles, the many body Hamiltonian with no interactions can be treated as the 3D harmonic oscillator of single particles whose ground state wavefunction is given by the product of the single particle ground state wavefunction $\psi_0(\vec{r})$, which is a Gaussian. The density distribution is: $n(\vec{r}) = N|\psi_0(\vec{r})|^2$, and the widths of the harmonic oscillator $a_{\text{ho}} = \sqrt{\frac{\hbar}{m\bar{\omega}}}$ determines the size of the cloud. The fugacity in the case of the trapped gas is modified to: $z(\vec{r}) = e^{(\mu - U(\vec{r}))/k_{\text{B}}T}$, while the density of the thermal fraction is formally still expressed by the relation $n_{\text{th}}(\vec{r}) = \frac{V}{\lambda_{\text{dB}}^3} g_{3/2}(z(\vec{r}))$. This changes the critical temperature, which now depends on the frequency of the trap according to

$$k_{\text{B}}T_c = \hbar\bar{\omega} \left(\frac{N}{g_3(1)} \right)^{1/3} \quad (2.21)$$

where the $g_3(1) \approx 1.2$ comes from having increased the degrees of freedom to six, due to the introduction of a potential that depends on the coordinates. Also eq. 2.19 and 2.20 are accordingly modified, and the dependence of the condensed fraction from the temperature becomes:

$$\frac{N_0}{N} = 1 - \left(\frac{T}{T_c} \right)^3. \quad (2.22)$$

2.4.2 Theory of a weakly interacting Bose gas

BEC arises as a consequence of quantum statistics, but the interaction energy of the atoms within the condensate is not negligible even for a dilute alkali gas at very low pressure, like the one considered here. In this type of experiments the gas is dilute and cold, and in such conditions the interactions can be described mostly by binary collisions at low energy, which are characterized by one parameter only: the s-wave scattering length a , which for ^{87}Rb is of the order of 10^2 Bohr radii. The effective interacting potential can be expressed by a delta function of the position of the two atoms, times a coupling constant g , which is linked to a through the relationship [3]:

$$g = \frac{4\pi\hbar^2 a}{m}. \quad (2.23)$$

Including this mean-field interaction with the harmonic potential energy in the time-dependent Schrödinger equation, one obtains the so-called Gross-Pitaevskii (GP) equation [46]:

$$i\hbar \frac{\partial}{\partial t} \Phi(\vec{r}, t) = \left(-\frac{\hbar^2 \nabla^2}{2m} + U(\vec{r}) + g|\Phi(\vec{r}, t)|^2 \right) \Phi(\vec{r}, t) \quad (2.24)$$

which holds for atom numbers much larger than 1, and when $\bar{n}|a|^3 \ll 1$, which expresses a condition for a gas to be dilute or weakly interacting [3]. For the ground state we can write the wavefunction as the product $\Phi(\vec{r}, t) = \phi(\vec{r}) \exp(-i\mu t/\hbar)$, where the spatial wavefunction is normalized to the total number of atoms in the condensate. Entering this ground state wavefunction into eq. 2.24 one obtains a time independent GP equation:

$$\left(-\frac{\hbar^2 \nabla^2}{2m} + U(\vec{r}) + g|\phi(\vec{r})|^2 \right) \phi(\vec{r}) = \mu \phi(\vec{r}). \quad (2.25)$$

In the absence of interactions, represented by the nonlinear mean-field term containing g , i.e. for $g = 0$, eq. 2.25 becomes the normal Schrödinger equation for a single particle in the potential $U(\vec{r})$.

Although we are describing the dilute gas as *weakly interacting*, this should not lead us to think that the effects of these interactions are small. If, for example, we take the ratio of the interaction energy and the kinetic energy we get $E_{\text{int}}/E_{\text{kin}} \propto Na/a_{\text{ho}}$, which, for $a > 0$ is easily much bigger than 1 in normal experiments. For our condensates $N \simeq 2 \cdot 10^5$, $a \simeq 5.6$ nm, and $a_{\text{ho}} \simeq 1.2$ μm , hence $E_{\text{kin}}/E_{\text{int}} \sim 10^{-3}$, and therefore the kinetic energy term can be neglected in the equation 2.25. This approximation leads to a density profile that is zero except where the chemical potential exceeds the energy of the external potential, where it is $n(\vec{r}) = [\mu - U(\vec{r})]/g$. For a harmonic potential, this has the shape of an inverted parabola. Such a situation is usually indicated as the Thomas-Fermi (TF) limit [3]. The

condition $\mu = U(R)$ determines the radius of the condensate in the TF limit, and it yields:

$$R = a_{\text{ho}} \left(\frac{15Na}{a_{\text{ho}}} \right)^{1/5} \quad (2.26)$$

which becomes bigger for increasing N . The balance between the interaction energy and that of the harmonic oscillator (h.o.) increases the size of the radius of the cloud from the length of the harmonic oscillator a_{ho} to the value $\sigma_{\text{cond}} = \zeta a_{\text{ho}}$, where the factor $\zeta \equiv (8\pi Na/a_{\text{ho}})^{1/5}$ is dimensionless and characteristic of the system [47]. For our condensates of about $2 \cdot 10^5$ atoms, in a trap of frequency $\bar{\omega} \simeq 2\pi \times 84$ Hz, $\sigma_{\text{cond}} \approx 8 \mu\text{m}$.

So far in this section we have considered, for simplicity, a spherical harmonic trap of frequency $\bar{\omega}$. For an axially symmetric trap, like our TOP potential, the ratio between the radial and the axial width is fixed by the conditions $\mu = m\omega_{\perp}^2 R_{\perp}^2/2 = m\omega_z^2 R_z^2/2$ [3], and their value can be easily derived as:

$$R_{\perp} = a_{\text{h.o.}\perp} \left(\frac{15Na}{a_{\text{h.o.}\perp}} \frac{a_{\text{h.o.}\perp}^2}{a_{\text{h.o.}z}^2} \right)^{1/5} \quad (2.27)$$

$$R_z = a_{\text{h.o.}z} \left(\frac{15Na}{a_{\text{h.o.}z}} \frac{a_{\text{h.o.}z}^4}{a_{\text{h.o.}\perp}^4} \right)^{1/5}. \quad (2.28)$$

where $a_{\text{h.o.}\perp}$ and $a_{\text{h.o.}z}$ are the harmonic oscillator lengths calculated using respectively the frequencies ω_{\perp} and ω_z .

2.5 Evaporative cooling

Evaporation in the magnetic trap is the final stage of our cooling process, which brings the atoms from the temperature of the optical molasses down to and beyond the threshold of condensation. The technique is now a well established one, and a comprehensive review of its application to trapped atoms can be found in [48]. Here I will recall the main concepts, with the intent of introducing all the terminology and equations necessary to follow smoothly the evaporation protocol used in this thesis and described in chapter 4.

The principle behind the idea of evaporative cooling of atoms is intuitively simple: one has to select the hottest atoms of the sample (i.e. those with temperature well above average), remove them from the trap, and then wait for the system to re-thermalize at a lower average temperature before iterating the procedure.

It is immediately clear that the most important requirement is that the lifetime of the trap is long compared to the time required for thermalization. Since the trap lifetime is mainly determined by the rate of inelastic collisions with the background atoms, while the time necessary to thermalize the sample depends on the rate of elastic collisions, the important parameter is the ratio between the elastic and inelastic collisions (“good” to “bad” collisions). An obvious drawback of the

method is the fact that the size of the sample gets drastically reduced during the evaporation. Typical scaling factor for BEC experiments in magnetic traps is a reduction of the atoms by one order of magnitude for every two orders of magnitude increase in phase space density.

Among the experimental techniques discussed in [48], the two that have been employed to evaporate the atoms in these thesis are described here.

2.5.1 Radio frequency evaporation

An experiment exploiting RF-spectroscopy of magnetically trapped atoms was first performed in 1989 by D. Pritchard and collaborators [49]. This technique exploits the spatial dependence of the Zeeman splitting of the atomic levels produced by an inhomogeneous magnetic field to selectively transfer atoms between the magnetic sub-levels.

In our experiment the inhomogeneous magnetic field is provided by the TOP trap, whose magnetic field is minimum at the centre and increases as we move towards the border. The spatial distribution of the atoms in the parabolic potential is Gaussian, and the higher the energy of an atom is, the further that atom is from the centre of the trap, and therefore it experiences a higher magnetic field amplitude and, hence, a bigger Zeeman splitting of the magnetic levels. When an electromagnetic field of frequency such that $h\nu = g_F m_F \mu_B B(\vec{r})$ is applied to the atoms, these are spin-flipped towards levels with negative $g_F m_F$, and therefore removed from the trap. This results in cooling, provided that the frequency is slowly ramped down in such a way that it always fulfills the resonance condition for the atoms at the border of the cloud, which have higher than average energy. For ^{87}Rb atoms in the $F = 1$, the Zeeman splitting of the levels at low fields is about 0.7 MHz/G, hence, for the typical magnetic fields in a TOP trap, the required frequencies are tens of MHz.

If the energy of the evaporated atoms is $\eta k_B T$, where the dimensionless parameter η , called the *truncation parameter*, depends on the Zeeman splitting, and we want it to be higher than the average energy of an atom in the trap, which for an harmonic trap is $3k_B T$, we need $\eta > 3$. This requires, in practical terms, to start the cut from a distance bigger than 2σ from the centre of the Gaussian distribution (where σ indicates its width). In addition to the request of reducing the temperature of the gas, evaporative cooling must also increase the phase space density if one wants to reach the quantum degeneracy. Following the approach taken in [48], it can be shown that for $\eta > 5$ a so called *runaway regime* can be reached, for which the rate of elastic collisions increases as the temperature gets lower. It can also be shown that the most favourable condition to reach this regime, in terms of the ratio between elastic and inelastic collisions (for atoms in a parabolic potential) is attained for a truncation parameter $\eta \simeq 6$, when the ratio required becomes of the order of 300.

2.5.2 Evaporation in a TOP trap

In our experiment we employ also a second evaporation technique that is intrinsically provided by the TOP trap. We have seen how the request of introducing a rotating bias field came from the necessity of displacing the zero of the magnetic field from the position where the atoms were centred. In the TOP trap the locus of points with $B = 0$ is commonly known by the name of *circle of death*. This circle, whose radius is $r = B_0/b'$, represents the locus of points where Majorana transition can bring trapped atoms into untrapped states. This fact provides an intrinsic evaporation surface because of the fact that the most energetic atoms, which generate the tails of the energy distribution, are the one capable of reaching the border of the trap (due to the inhomogeneity of the TOP potential) and hence the circle of death where they are expelled from the trap. The technique is schematically represented in fig. 2.4. This evaporation method is therefore based on the reduction of the radius of the circle of death. As usual, the critical parameter for an effective evaporation is the speed at which the radius is reduced, and it is experimentally optimized as a function of the trap lifetime and the re-thermalization rate.

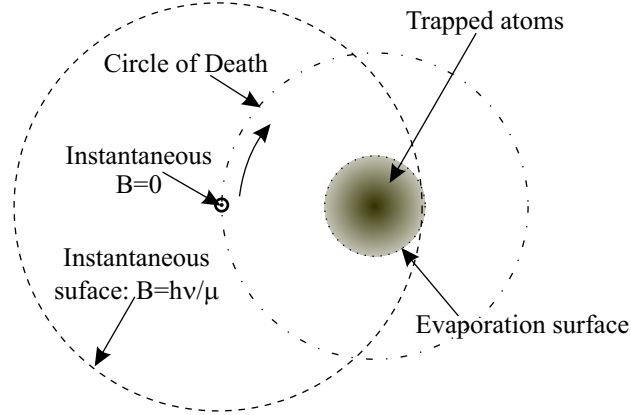


Figure 2.4: Sketch of the evaporation in a TOP trap at an instant of time: the circle of death and the RF evaporation condition, provide an evaporation surface that has the shape of a nearly cylindrical barrel.

In practical terms, although this method proves to be very effective in reducing the temperature whilst increasing the phase space density, trying to employ it as the only evaporation technique, from the initial magnetic trap down to beyond the condensation threshold, leads to big losses. This happens because we reduce the radius just by decreasing the value of B_0 whilst keeping a high gradient (to ensure a higher collision rate). During this process the oscillation frequency of the atoms in the trap increases, so the approximation $\omega \ll \omega_T$ becomes less and less valid. Experimentally we have looked at the increase in phase space density *versus* the loss in number of atoms, and stopped this method when it started to become less efficient. From that point on we continue the evaporation with the radio frequency.

2.6 Optical trapping

In this experiment we make use of optical traps to store our condensate after having produced it in a magnetic trap. The necessity of doing this has already been pointed out in the introductory chapter. Therefore this section is devoted to introducing the optical dipole force and the two types of trap that we use following the approach adopted in [50], where more details and derivations can be found.

The optical dipole force arises from the interaction felt by an atom when an oscillating atomic electric dipole moment is induced on it by the oscillating electric field of the laser light. Two quantities of main interest for optical trapping are the dipole force potential U_{dip} and the rate of scattered photons Γ_{sc} (which is the ratio $P_{\text{abs}}/\hbar\omega$ between the power absorbed and the energy of the absorbed photon). These two quantities depend both on the dipole moment, and ultimately on the real and imaginary part, respectively, of the atomic polarizability. Their expressions are derived in [50] for the simple harmonic oscillator case (i.e. the Lorentz model atom), with large detunings (but still small compared with the transition frequencies) so that the rotating-wave approximation can be applied, and they can be expressed as:

$$U_{\text{dip}}(\vec{r}) = \frac{3\pi c^2 \Gamma}{2\omega_0^3 \delta} I(\vec{r}) \quad (2.29)$$

$$\Gamma_{\text{sc}}(\vec{r}) = \frac{3\pi c^2}{2\hbar\omega_0^3} \left(\frac{\Gamma}{\delta}\right)^2 I(\vec{r}) \quad (2.30)$$

where δ is the frequency detuning of the laser from the frequency of the optical transition ω_0 , and $I(\vec{r})$ is the intensity of the dipole trap laser beam. For a multilevel atom like an alkali atom, the potential of eq. 2.29 turns out to be the ac Stark shift of the ground-state $|g_i\rangle$:

$$\Delta E_i = \frac{3\pi c^2 \Gamma}{2\omega_0^3} I \times \sum_j \frac{c_{ij}^2}{\delta_{ij}} \quad (2.31)$$

where the contribution of the different levels $|e_j\rangle$ is taken into account via the transition coefficients $c_{ij} = \frac{\langle e_j | \mu | g_i \rangle}{\|\mu\|}$ of the dipole moment matrix μ_{ij} .

For the case of alkali atoms in particular, the energy levels involved in the D lines are such that the fine structure (FS) splitting is much larger than the hyperfine structure (HFS) of the ground state, which in turn has splittings much larger than those of the excited state. With the assumption of unresolved HFS of the excited state, valid when the radiation employed is far detuned from resonance (compared to the HFS of the excited state) as in our case, Grimm et al. in [50] have derived an expression for the potential of the ground state with angular momentum F and magnetic quantum number m_F , valid for both circular and linear polarization of the light:

$$U_{\text{dip}}(\vec{r}) = \frac{3\pi c^2 \Gamma}{2\omega_0^3} \left(\frac{1 - P g_F m_F}{3\delta_{D1}} + \frac{2 + P g_F m_F}{3\delta_{D2}} \right) I(\vec{r}) \quad (2.32)$$

where $P = 0$ for linearly polarized light and ± 1 for circularly σ^\pm polarized light. The detunings δ_{D1} and δ_{D2} are calculated for the particular F level of the ground state and are relative to the centre of the hyperfine splitting of the two excited states ${}^2P_{3/2}$ and ${}^2P_{1/2}$. An analogous expression can be derived for the scattering rate of photons, which takes into account the individual contribution of the two D lines.

The simplest example of optical dipole force trap is provided by a single beam, detuned far below the atomic resonance (red detuned) and strongly focussed such as to create a centre of maximum intensity where the atoms are trapped. For a Gaussian beam of total power P , the intensity is a function of the position along the axis of propagation z and of the distance r from it

$$I_{\text{FB}}(r, z) = \frac{2P}{\pi w^2(z)} \exp\left(-2\frac{r^2}{w^2(z)}\right) \quad (2.33)$$

where $w(z)$ indicates the $1/e^2$ radius of the beam, whose dependence on z is given by the equation

$$w(z) = w_0 \sqrt{1 + \left(\frac{z}{z_{\text{R}}}\right)^2} \quad (2.34)$$

where w_0 is called the beam waist and indicates the minimum radius assumed by the focussed beam; the confocal parameter or Rayleigh length $z_{\text{R}} = \pi w_0^2/\lambda$ is the distance from the focus over which the radius increases to $\sqrt{2} \cdot w_0$; z_{R} is larger than the waist by a factor $\pi w_0/\lambda$ thus producing a much lower gradient in the axial direction than the one in the radial direction.

The depth of the trap equals the optical potential $U_0 \equiv |U(r=0, z=0)|$ at the position of maximum intensity. When the thermal energy $k_{\text{B}}T$ of the atomic cloud is much smaller than U_0 , the atoms will be confined in the central region of the beam so that the ratios r/w_0 and z/z_{R} are always smaller than 1. In such a situation, the intensity profile can be expanded to the first order in these quantities, yielding a cylindrical harmonic potential

$$U_{\text{FB}}(r, z) \simeq -U_0 \left[1 - 2\left(\frac{r}{w_0}\right)^2 - \left(\frac{z}{z_{\text{R}}}\right)^2 \right] \quad (2.35)$$

where the minus sign comes from the red detuning, which we are assuming here, and from having defined the potential depth U_0 as a positive quantity. When the assumptions made for the approximations performed above hold, the trap frequencies can be derived from the harmonic potential 2.35 as

$$\omega_r = \left(\frac{4U_0}{mw_0^2}\right)^{1/2} \quad (2.36)$$

$$\omega_z = \left(\frac{2U_0}{mz_{\text{R}}^2}\right)^{1/2}. \quad (2.37)$$

2.6.1 1D Optical Lattice

The first of the two optical trap configurations that we used is a one-dimensional standing wave. Experimentally such a configuration can be achieved either by retro-reflecting a single laser beam, which was our choice, or by superimposing two identical, counter-propagating, laser beams. The analytical expression for the resulting potential, under the same approximations made before of $U_0 \gg k_B T$, is given by:

$$U_{\text{SW}}(r, z) = -U_0 \cos^2(kz) \left[1 - 2 \left(\frac{r}{w_0} \right)^2 - \left(\frac{z}{z_R} \right)^2 \right] \quad (2.38)$$

where U_0 is 4 times bigger than for a travelling wave of same power and waist size, because of constructive interference of the electric fields of the two counter-propagating beams. The period of the trap intensity modulation is $\pi/k = \lambda/2$, leading (for red frequency detuning) to very tight confinement along the axial direction at the antinodes of the potential. As a result, the atoms are trapped in pancake-shaped harmonic traps, stacked along the direction of propagation of the light. Expanding the cosine square of eq. 2.38, and again keeping only the second order terms in r and z (neglecting terms of the order of z^2/z_R^2 and z^2/w_0^2 which are much smaller than $k^2 z^2$), gives the trapping frequencies of the standing-wave potential as

$$\omega_r = \left(\frac{4U_0}{mw_0^2} \right)^{1/2} \quad (2.39)$$

$$\omega_z = k \left(\frac{2U_0}{m} \right)^{1/2}. \quad (2.40)$$

The radial frequency has the same form as eq. 2.36, but the potential is this time 4 times deeper. The axial frequency is much higher than the one in eq. 2.37 by a factor $2(\pi w_0/\lambda)^2$ and it reaches its maximum value given by eq. 2.40 for $z = 0$, and decreases towards the border of the trap due to the reduced intensity.

The trap frequencies in eq. 2.39 and 2.40 will be used, in appendix C, to deduce the density of the atoms in each lattice site. In doing so, we find that the clouds should be treated as a 2D gas. The density in the lattice will be used to obtain an estimate of the three body collision rate around the Feshbach resonance, and in chapter 8 to compare with the theory the loss curves obtained by sweeping across the resonance.

Whilst a technical discussion of the alignment procedure and of the sensitivity of such a configuration to misalignment will be given in chapter 5, here is given a brief review of the physics of a BEC trapped in a 1D optical lattice. This discussion follows the approach used in [51], and its objective is to examine the relationship between the lattice parameters and the momentum distribution of the atoms when they are diffracted by a pulse of the standing wave.

In a simplified form, the standing-wave potential can be written as

$$U(x, t) = \frac{U_0}{2}[1 + \cos(2kx)] \quad (2.41)$$

where k represents the wavenumber of the laser light of wavelength $\lambda = 2\pi/k$. The period of the potential is half a wavelength (in our case $\approx 0.4 \mu\text{m}$), while the Thomas-Fermi radius along z is about $6 \mu\text{m}$, therefore the condensate occupies about 30 lattice sites. We shall approximate this with an infinite periodic potential and apply the band structure theory to our system.

Let $E_{n,q}$ indicate the eigenenergies and $|n, q\rangle$ the eigenstates (Bloch states) of the system, where n is the band index and q is the quasi-momentum. The periodicity in the reciprocal lattice is $2\hbar k$, so that the Bloch states can be expressed as a linear combination of plane waves of momenta $p = q + 2m\hbar k$:

$$|n, q\rangle = \sum_{m=-\infty}^{\infty} a_{n,q}(m) |\phi_{q+2m\hbar k}\rangle. \quad (2.42)$$

To obtain the energy levels of the atoms in the lattice, we must solve the Schrödinger equation of a particle in the periodical potential of eq. 2.41. The wavefunction obeys the Bloch theorem, and therefore it has period $\lambda/2$

$$\psi_{n,q}(x + \frac{\lambda}{2}) = e^{i\frac{q\lambda}{2\hbar}} \psi_{n,q}(x). \quad (2.43)$$

The eigenenergies $E_{n,q}$ are usually plotted for each band n in the quasi-momentum range $q \in [-\hbar k, \hbar k]$, which is called the *first Brillouin zone*.

When the atoms loaded into such a potential come from a BEC, their momentum spread is $\Delta p \simeq \hbar/\Delta r$. If we assume that Δr is about the Thomas-Fermi radius, then, for our conditions, $\Delta p \approx 0.01\hbar k$. Therefore the atoms from a BEC are loaded into a lattice state with a well defined quasi-momentum. If we load a stationary condensate into the lattice, it will have a uniform phase across the lattice and, from Bloch theorem, $q = 0$.

A BEC that is suddenly loaded into a lattice has a very small momentum spread, so the condensate can be considered a plane wave ($|\Psi(t=0)\rangle = |\phi_q\rangle$), described as a superposition of Bloch states. At $t = 0$ it is

$$|\Psi(t=0)\rangle = \sum_{n=0}^{\infty} |n, q\rangle \langle n, q | \phi_q \rangle. \quad (2.44)$$

Taking into account eq. 2.42, and using as evolution operator $e^{-i\frac{E_{n(q)}t}{\hbar}}$, the BEC wavefunction, whilst in the lattice, evolves as

$$|\Psi(t)\rangle = \sum_{n=0}^{\infty} a_{n,q}^*(0) e^{-i\frac{E_{n(q)}t}{\hbar}} |n, q\rangle. \quad (2.45)$$

If the evolution lasts for a time τ , after which the potential is suddenly switched off, we can obtain the coefficients $b_q(m)$ of the plane wave components in the lattice frame:

$$b_q(m) = \sum_{n=0}^{\infty} a_{n,q}^*(0) a_{n,q}(m) e^{-i \frac{E_n(q)\tau}{\hbar}}. \quad (2.46)$$

The population of the plane wave components oscillates as a function of τ , as shown in fig. 2.5, where $|b_q(m)|^2$ is plotted against the time τ spent in the lattice. In chapter 5 there will be a similar plot obtained experimentally by observing the oscillation of the population of the diffracted orders when we apply a lattice pulse of variable duration τ to the condensate. These plots are used to determine the lattice depth.

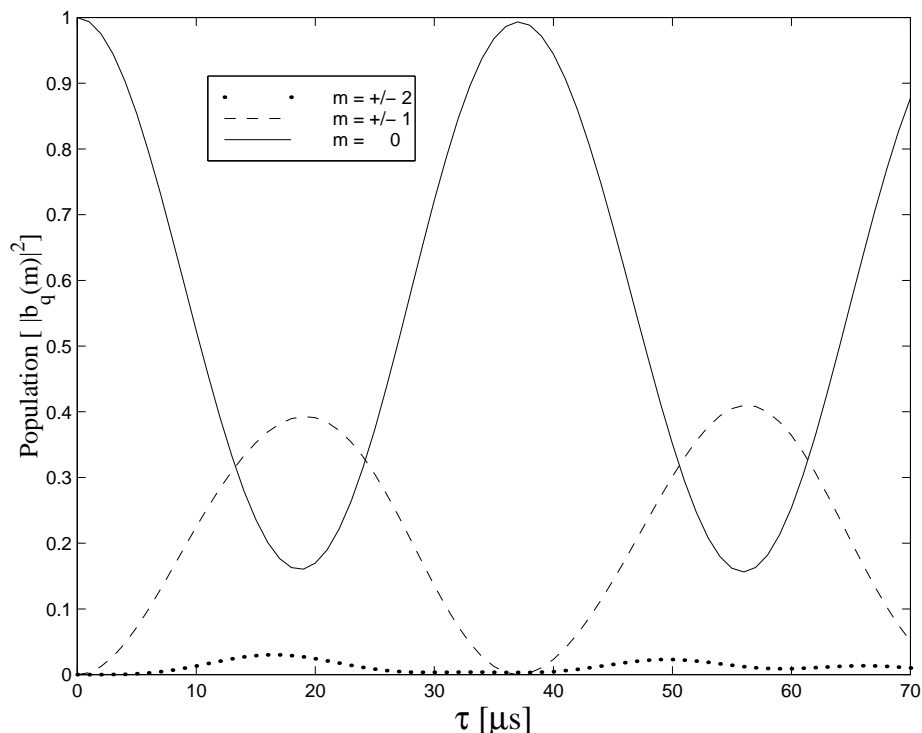


Figure 2.5: Plot of the modulus square of $b_q(m)$ of eq. 2.46 (for $q = 0$) as a function of τ for a lattice depth $U_0 = 11.4 E_{recoil}$.

2.6.2 Crossed-beam dipole trap

The atomic clouds confined in a standing wave are very asymmetric, as they are very tightly squeezed in one direction compared to the others. In contrast, a single focussed beam, discussed above, creates a potential well elongated in the axial direction due to the size of the Rayleigh length. An obvious way to overcome the

weakness in the axial direction is to use two laser beams orthogonal to each other, to form what is known as a crossed-beam dipole trap. The beams have different frequencies so that the resulting potential is the sum of the potentials of the two beams, and these achieve strong confinement in all directions.

In our experiment the two laser beams have different waist and power. The resultant dipole potential is obtained by adding two potentials of the form given in eq. 2.35, where beam 1 has its axis along z and beam 2 propagates along y . The potential obtained, up to quadratic terms, can be written as

$$U_{\text{CB}}(r, z) \simeq -(U_{01} + U_{02}) + \left(\frac{2U_{01}}{w_1^2} + \frac{2U_{02}}{w_2^2} \right) x^2 + \frac{2U_{01}}{w_1^2} y^2 + \frac{2U_{02}}{w_2^2} z^2 \quad (2.47)$$

hence the oscillation frequencies are given by:

$$\omega_x = \sqrt{\left(\frac{4U_{01}}{mw_1^2} + \frac{4U_{02}}{mw_2^2} \right)} \quad (2.48)$$

$$\omega_y = \sqrt{\frac{4U_{01}}{mw_1^2}} \quad (2.49)$$

$$\omega_z = \sqrt{\frac{4U_{02}}{mw_2^2}} \quad (2.50)$$

These expressions show the dependence on the waist sizes w_1 and w_2 of the two beams and also on the depths of the potentials.

A last comment on the crossed-beam dipole trap depth: although the magnitude of the potential at the centre is $U_{\text{CB}}(0, 0) \simeq -(U_{01} + U_{02})$ from eq. 2.47, the effective potential depth is actually the $\min(U_{01}, U_{02})$ because any atom more energetic than that can always escape from the trap along the axis of the other beam.

Gravity has a significant effect as it modifies the shape of the potential along z and imposes a minimum intensity on the beams to hold the atoms against their weight. Therefore, optical traps are usually formed with tight confinement along the vertical direction. A quantitative analysis of the effect of gravity on the crossed-beam dipole trap will be performed in chapter 6.

2.7 Feshbach resonances

The description of the production of molecules given in the introductory chapter shows that the range of the collisions plays a central role. Atoms in a BEC occupy the lowest translational state available to them. Under these conditions, the range of the collision can be described using a single parameter: the s-wave scattering length a . The energy of a condensed atom due to the presence of the others is $U = gn$ where n is the number density of particles and g is the mean field

parameter introduced in eq. 2.23. This shows that the energy has the same sign as a and that a positive a leads to effectively repulsive interactions while a negative a leads to attractive interactions.

The scattering length of two colliding atoms can vary in the presence of an external magnetic, optical, or RF field. In this thesis we make use of an external magnetic field. These modifications are significant only for certain values B_0 of the magnetic field, when the scattering length has a singularity: the so-called *Feshbach resonances*. Away from a resonance the background value of the scattering length a_{bg} is approximately constant; ^{87}Rb atoms in the ground state ($|F = 1, m_F = 1\rangle$) have $a_{bg} = 100.4(1) a_0$ [52], where $a_0 = 0.053$ nm is the Bohr radius. Near a resonance it varies according to the relation [53]:

$$a(B) = a_{bg} \left[1 - \frac{\Delta B}{B - B_0} \right] \quad (2.51)$$

where ΔB is the width of the resonance as indicated in fig. 2.6.

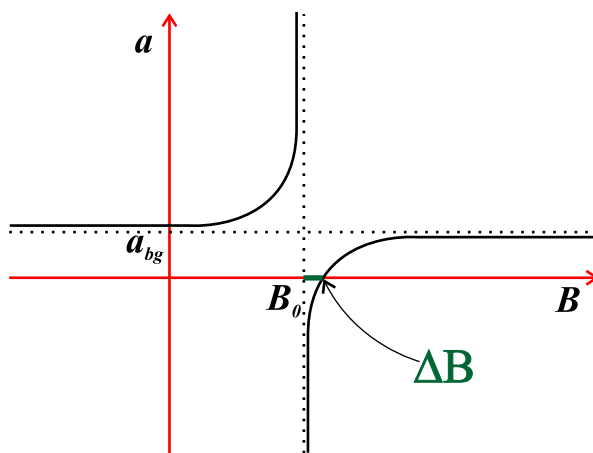


Figure 2.6: Dependence of the scattering length on the external magnetic field near a Feshbach resonance.

Over the years calculations have been reported for Feshbach resonances in the lowest hyperfine states of all the alkali atoms that have been condensed. These resonances have in turn been measured in cold gases of Na [54], ^{85}Rb [55, 56], Cs [57], ^{40}K [58], and ^7Li [59, 60].

As far as ^{87}Rb is concerned, a search was carried out experimentally in 1995 [61] for atoms in the $|F = 1, m_F = -1\rangle$ state, and no resonances were observed. In 1997 Vogels et al. [33] predicted four of them in the state $|F = 1, m_F = 1\rangle$.

The dispersive behaviour of the scattering length around the resonance (eq. 2.51) suggests that tuning the magnetic field across the resonances gives an experimental handle on the scattering length. This degree of control has allowed observation of a controlled implosion of a Bose gas, the so-called *Bosenova* [62], and the creation

of a bright soliton in a BEC [59, 60]. In the future it may be possible to explore number squeezing experiments by tuning the parameter U/J (the ratio between the trap depth and the tunnelling rate), key to the transition to the Mott-insulator phase, by acting on the scattering length to increase U rather than on the intensity of the laser.

In the work described in this thesis the object was to exploit this tunability of the interactions to produce molecules, by sweeping across a Feshbach resonance from negative to positive values of the scattering length. The atomic and molecular energy levels have different Landé g -factors, and so at specific values of the magnetic field the energy of a pair of free colliding atoms can be resonant with the energy of a bound molecular state. The experiment was first successfully accomplished by Dürr et. al. [63].

2.7.1 Feshbach Resonances in ^{87}Rb

Although the state where the presence of s -wave Feshbach resonances was predicted for ^{87}Rb , $|F = 1, m_F = 1\rangle$, cannot be trapped in a magnetic trap for the reason explained in section 2.3, it can be trapped in an optical potential (see fig. 2.7), and indeed we need to trap the atoms in the state where they undergo the resonance for a reason that will be clear very soon.

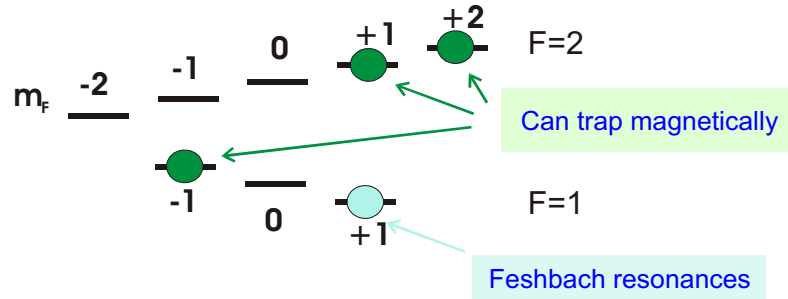


Figure 2.7: Hyperfine structure of the ground state in ^{87}Rb in the presence of a magnetic field. Zeeman sub-levels are indicated where atoms can be trapped magnetically and where Feshbach resonances have been predicted.

In 2002 Marte et al. [34] observed 43 resonances in ^{87}Rb atoms within a magnetic field range comprised between 0.5 and 1260 G. Only 18 of them come from atoms prepared in the entrance channel $|F = 1, m_F = 1\rangle \otimes |F = 1, m_F = 1\rangle$. These are all rather narrow resonances that, in most cases, have widths much smaller than 1 mG. Two were found to be significantly wider than 1 mG, the widest being centred at 1007.4 G with a measured width of 0.20(3) G [64].

In our experiment we can produce BEC of ^{87}Rb atoms in the $|F = 1, m_F = -1\rangle$ state by means of evaporation in a magnetic trap. To observe the resonance, we then transfer the BEC into an optical trap, use an RF sweep to change the

internal state of the BEC to $|F = 1, m_F = 1\rangle$, ramp up a magnetic field, and look for atom loss as we sweep across the resonance. The losses are due to inelastic collisions between the trapped atoms. In the specific case of resonances like the one at 1007 G, which involves only atoms in the absolute ground state of ^{87}Rb , the $|F = 1, m_F = 1\rangle$ state, inelastic two-body collisions cannot occur, hence the losses must come mainly from 3-body collisions.

To accurately find the resonance, in experiments we transfer the atoms into the $|F = 1, m_F = 1\rangle$ state, then we quickly ramp up the field (at a rate of 20-50 G/ms) to a certain value B_{hold} , sit there for 100 ms and then ramp down very quickly again and take an image of the atoms left in the trap. To ramp up and down the field for the resonance at 1007 G, we need at least about 50 ms. This long ramping time is the reason why the atoms cannot be in free fall and need to be trapped.

Fast ramps of the magnetic fields are required to prevent losses from intermediate resonances. When this experiment is repeated for many values of B_{hold} around the resonance we obtain, as we shall see in chapter 7, a curve describing a dip that shows the atom loss as a function of the magnetic field, and whose centre gives the position of the resonance. As far as the width is concerned, there is no obvious relationship between the width of the dip (as fitted with a Lorentzian, for example) and the theoretical width ΔB mentioned above, which indicates only the magnetic field range in which the scattering length has negative sign. This can be obtained by a direct measurement of the scattering length, as described in [64].

As we have said, these losses are mainly due to 3-body collisions, whose rate equation

$$\frac{dN}{dt} = -K_3 \langle n^2 \rangle N \quad (2.52)$$

is characterized by the rate coefficient K_3 . In the case of a condensate the value obtained for K_3 is expected to be 6 times smaller than for a thermal cloud. This factor of 6 arises from correlations, and is discussed in more detail in chapter 7; therefore we can define, for a condensed cloud: $K_3^c = K_3/3!$ [65]. Experimental measurements of K_3 for ^{87}Rb are reported in [65, 34].

2.8 Formation of ultracold molecules exploiting a Feshbach resonance

This section summarizes the theory of the formation of molecules in an adiabatic passage across a Feshbach resonance (following the approach of Góral *et al* [66]). Góral *et al* describe a two-channel theory for the association of ultracold molecules with a linear ramp of the magnetic field across the Feshbach resonance.

The resonance at 1007 G in ^{87}Rb is an s-wave resonance, with the two colliding atoms both in the $|F = 1, m_F = 1\rangle$ electronic ground state. The scattering channel of the two asymptotically free atoms will be regarded as the open channel and its

potential indicated as the background scattering potential $V_{bg}(r)$. This is, for $r \rightarrow \infty$, a van der Waals potential, so its dependence on the separation of the two atoms is $-C_6/r^6$. The presence of a homogeneous magnetic field removes the degeneracy on m_F , and for certain values of B the weak coupling of the open channel with other channels becomes much stronger. For the values of B for which the open channel is strongly coupled to a closed channel ($V_{cl}(r)$) we have a Feshbach resonance.

The formation of molecules at a Feshbach resonance is only possible when sweeping across it from negative to positive scattering lengths. For ^{87}Rb , this means that the ramp will start at a strength of the magnetic field higher than the resonance position and sweep down across it. The connection between bound states of the closed channel and Feshbach resonances can be seen in a very simple way: the singularities of the scattering length are located exactly at the magnetic field positions for which the molecular bound states cross the energy of the dissociation threshold into two free atoms. This is clearly shown in Fig. 2.8 for the binding energies of two ^{87}Rb atoms in the s-wave molecular states of the open channel below the dissociation threshold.

In the theoretical description a two-body Hamiltonian is used, that depends only on 5 parameters. This approach leads to an exact solution, to which many-body physics considerations are applied, to give prediction for the rate of association of molecules.

The value of the magnetic field for which the dissociation threshold of the open channel becomes degenerate with the energy of the resonance state in the closed channel is slightly different from the position of the resonance (B_0 in eq. 2.51). This other value of the magnetic field is denoted by B_{res} and is linked to B_0 through the following relationship (see [66]):

$$B_0 = B_{\text{res}} - \frac{\langle \phi_{\text{res}} | W G_{bg}(0) W | \phi_{\text{res}} \rangle}{\left[\frac{dE_{\text{res}}}{dB} (B_{\text{res}}) \right]} \quad (2.53)$$

where $E_{\text{res}}(B)$ is the energy of the deeply bound state in the closed-channel (the resonance state) that becomes resonant with the free-atoms threshold of the open channel, and $\langle \phi_{\text{res}} | W G_{bg}(0) W | \phi_{\text{res}} \rangle$ is the matrix element of the Green function G_{bg} of the two-body Hamiltonian for the open channel between the state $W | \phi_{\text{res}} \rangle$. This state represents the inter-channel coupling, where W is the strength of the coupling between the two channels, and ϕ_{res} indicates the resonance state. The five parameters (and their values) used to describe the resonance enhanced scattering are: the van der Waals dispersion coefficient $C_6 = 4660$ au, the background value of the scattering length $a_{bg} = 100.4 a_0$, the width of the resonance $\Delta B = 200$ mG, the shift $B_0 - B_{\text{res}} = -63.71$ mG, and the slope of the resonance state energy $\frac{1}{h} \frac{dE_{\text{res}}}{dB} (B_{\text{res}}) = 3.8$ MHz G^{-1} (see [66] and references therein). Fig. 2.9 shows the dependence of the binding energy as a function of the magnetic field strength for

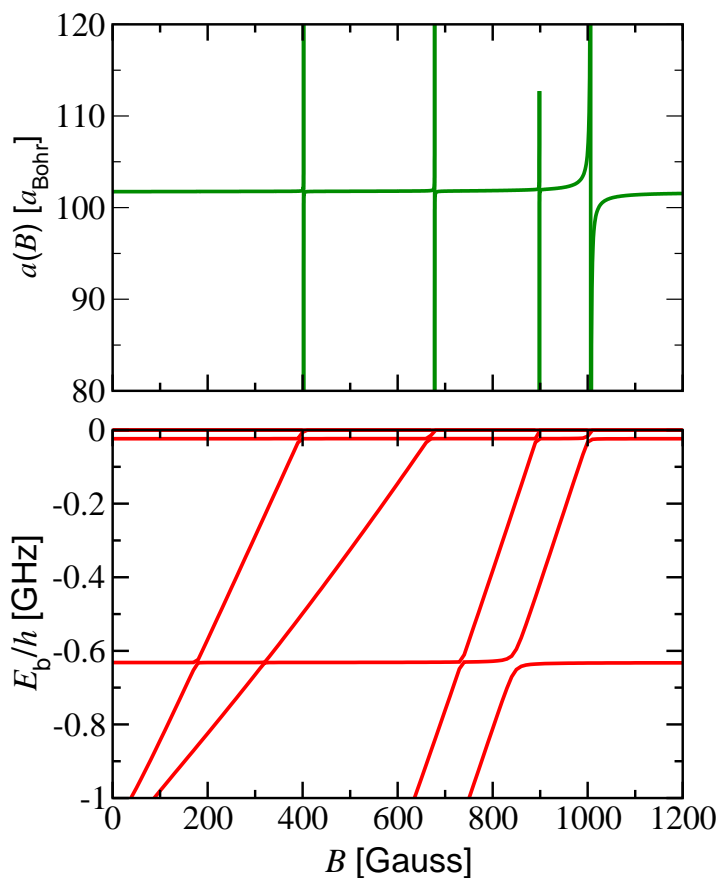


Figure 2.8: The magnetic field dependence of (above) the s-wave scattering length and (below) the energies of the highest excited s-wave vibrational molecular bound states of two ^{87}Rb atoms. [Courtesy of K. Góral and T. Köhler.]

the coupled two-channel system. The avoided crossing between the first bound state E_{-1} of the entrance channel and the resonance state arises from the Landau-Zener *noncrossing rule* for molecular states of same symmetry [67].

2.8.1 Landau-Zener approach

To describe the adiabatic association of molecules in a dilute BEC, Mies *et al* [68] have used a time dependent two-body Schrödinger equation adding, to the background potential $V_{bg}(r)$, a spherically symmetric harmonic potential of frequency ω_{ho} , provided by an optical trap. The vibrational trap states $\phi_v(r)$ are labelled by the quantum number $v = -1, -2, -3, \dots$ so that the dissociation threshold in the open channel is given by E_0 (see fig. 2.10). It is realistic to assume that

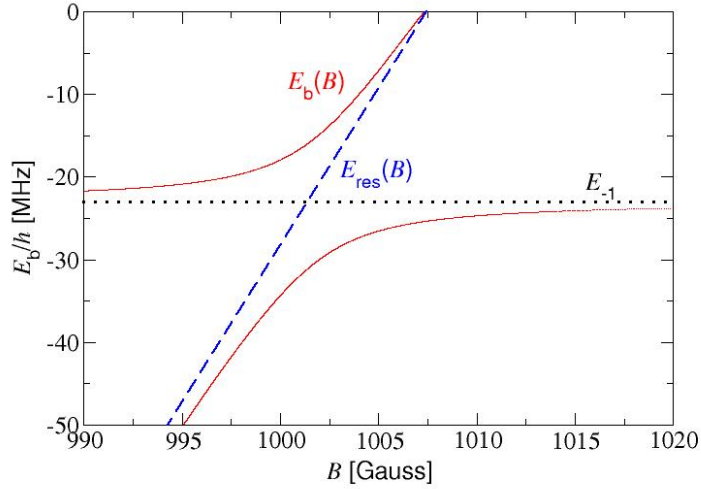


Figure 2.9: Dependence of the binding energy of the vibrational bound states of the two channel Hamiltonian on the magnetic field. [Courtesy of K. Góral and T. Köhler.]

$|E_{-1}| \gg \hbar\omega_{\text{ho}}$ so that the harmonic trapping potential does not modify the vibrational bound states. The last assumption is that in the closed channel the atoms are restricted to the resonance state $\phi_{\text{res}}(r)$. With these assumptions it is possible to work out two sets of equations that determine the exact dynamics of the adiabatic association of two atoms in the harmonic potential [66].

The equations deduced by Goral *et al* are not repeated here, but it is interesting to see how they extend the two-body interaction description to include effects from the many-body theory of Köhler and Burnett [69]. Firstly, the presence of mean-field interactions increase the size of the atomic cloud which, therefore, occupies a much larger volume than that occupied by a single atom in the harmonic trap. This size is given by the Thomas-Fermi radius. Mies *et al*, however, suggested that it is reasonable, in the region within the Thomas-Fermi radius, to replace the states of the harmonic potential with those of a spherical box with a zero-point energy of E_{kin}/N . This is due to the assumption that in that region the mean field cancels the trap potential, leaving an effective flat potential to be felt by the individual atoms. The size of this box is related to the TF radius of eq. 2.26 by the equation:

$$R_{\text{box}} = R_{\text{TF}} \left(\frac{2}{5}\right)^{1/2} \frac{\pi}{\sqrt{\ln\left(\frac{R_{\text{TF}}}{1.2683a_{\text{ho}}}\right)}} \quad (2.54)$$

where a_{ho} is the size of the harmonic oscillator. Another many-body effect included in the theory is that, for a BEC, there is a macroscopic occupation of the lowest energy state. Therefore if we consider a ramp of the magnetic field across the

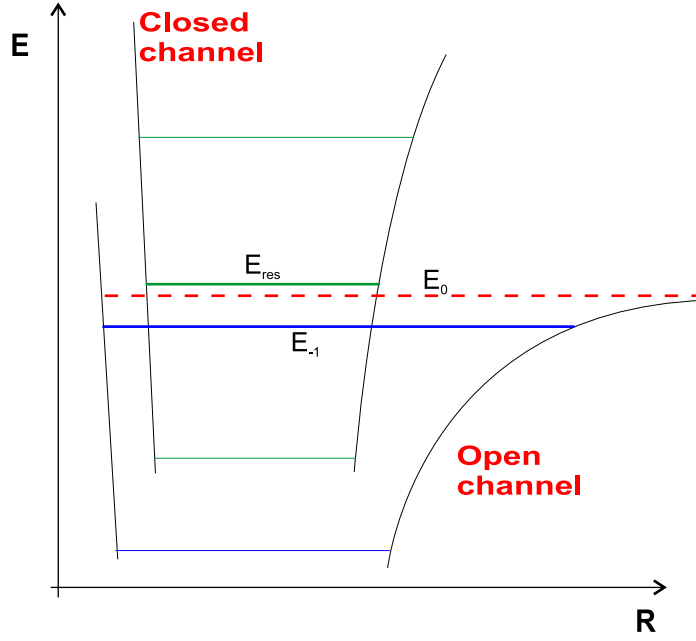


Figure 2.10: Schematic of potential curves of the two channels shown in the introduction (expanded energy scale). The states involved in the molecule formation, this time have been labelled according to the convention made in the text.

resonance, the prevailing transition involves only the condensate mode and the resonance state; each atom interacts with the other $N - 1$ atoms, and this enhances this prevailing transition by a factor $\sqrt{N - 1}$.

Combining these considerations with the exact results of the two-body theory cited above, gives two equations that exhibit a two-level Rabi flopping style passage from the condensate mode to the resonance state:

$$\begin{aligned} i\hbar\dot{C}_0(t) &= E_0C_0(t) + \frac{1}{2}\hbar\Omega^*C_{\text{res}}(t) \\ i\hbar\dot{C}_{\text{res}}(t) &= E_{\text{res}}(B(t))C_{\text{res}}(t) + \frac{1}{2}\hbar\Omega C_0(t) \end{aligned} \quad (2.55)$$

which are the rate equations for the probability amplitude of the two states. The term $\frac{1}{2}\hbar\Omega$ is given by

$$\frac{1}{2}\hbar\Omega = \sqrt{N - 1} \sqrt{\frac{(2\pi\hbar)^3}{\frac{4\pi}{3}R_{\text{box}}^3}} \langle \phi_{\text{res}} | W | \phi_0^{(+)} \rangle. \quad (2.56)$$

Here $\langle \phi_{\text{res}} | W | \phi_0^{(+)} \rangle$ is the matrix element of the coupling strength W between the zero-energy background scattering state and the resonance state, times the two factors accounting for the many-body physics effects discussed above.

For a linear ramp of the magnetic field across the resonance, and assuming that, at $t = 0$, all the particles are in the condensate state so that $|C_0(0)|^2 = 1$

and $|C_{\text{res}}(0)|^2 = 0$, the final populations (for $t_{\text{ramp}} \rightarrow \infty$) are determined by the Landau-Zener formulae:

$$\begin{aligned} |C_0(t_{\text{ramp}})|^2 &= e^{-2\pi\delta_{\text{LZ}}} \\ |C_{\text{res}}(t_{\text{ramp}})|^2 &= 1 - e^{-2\pi\delta_{\text{LZ}}}. \end{aligned} \quad (2.57)$$

The final fraction of atoms converted into molecules is determined by the Landau-Zener exponent δ_{LZ} , which depends only on three parameters: the background scattering length a_{bg} , the width ΔB of the resonance, and the ramp speed $|\frac{dB}{dt}|$, according to the relation:

$$\delta_{\text{LZ}} = (N - 1) \frac{4\pi\hbar|a_{bg}||\Delta B|}{\frac{4\pi}{3}R_{\text{box}}^3 m|\frac{dB}{dt}|}. \quad (2.58)$$

For $N = 2$ this is the exact result of the multi-level two body theory [66]. The remnant BEC population is given by $N|C_0(t_{\text{ramp}})|^2$, while the number of diatomic molecules formed is $N|C_{\text{res}}(t_{\text{ramp}})|^2/2$. Note, however, that this treatment does not account for the depletion of the condensate state while molecules are associated; to take this into account the total number N should be replaced by the actual number $N|C_0(t)|^2$ in eq. 2.55.

These equations are used to predict the fraction of atoms converted into molecules as a function of the inverse ramp speed for comparison with the experimental data (see chapter 8). This model does not take into account losses from three-body collisions, and the loss of molecules de-excited to more deeply bound states.

The theory introduced so far implies that an infinitely slow linear ramp (if losses are neglected) leads to the complete conversion of atoms into molecules. Experimentally, however, loss mechanisms are important. Especially for our specific case, where the biggest coupling with the resonance state occurs at a field for which the size of the molecules is small, so that de-excitation to lower bound states is likely to take place. The lack of a complete theory that accounts also for these effects makes it necessary to optimize empirically the experimental protocol. Xu *et al* [70], for their experiment on the formation of Na₂ molecules at MIT, reported that, in order to reduce the amount of losses, they used a ramp that was one order of magnitude faster than the optimum by LZ theory. A similar feature was also observed for ⁸⁷Rb at MPI [71], where in recent experiments the magnetic field was stepped just below the resonance rather than being slowly ramped back.

Experimental apparatus

This chapter describes the design and construction of our experimental apparatus which was a major part in the work presented here. Standard techniques of laser cooling and magnetic trapping have been employed to achieve BEC in ^{87}Rb . The characteristics of the vacuum system required for the experiments presented here, along with a general description of the laser sources and the optics present on the optical bench, is given in the sections from 3.1 to 3.3.

Section 3.4 describes the magnetic coils and gives details of the techniques used to make the field sufficiently stable to see the Feshbach resonance. A double MOT system, which provides the source of cold atoms for this experiment, is described in sections 3.5 and 3.6.

The last two sections describe the imaging system and the computer control of the experiment respectively. The equipment used to generate the standing wave and the crossed dipole trap are standard, and will be described directly in chapters 5 and 6.

3.1 Vacuum system

Evaporative cooling (and also laser cooling) of a gas can only be carried out in a good vacuum because the evaporation process takes a finite amount of time, and therefore the lifetime of the cloud (which is limited by the collisions with the background gas) must be at least as long. For evaporative cooling it is necessary that the lifetime of the magnetic trap is long compared to the thermalization time (determined by the rate of elastic collisions between cold atoms). This requires typical lifetimes of the order of 10^2 s at pressures of about 10^{-11} Torr. To achieve such pressures in the vacuum chamber we use ion pumps as well as a non-evaporable getter (NEG) pump.

The region of very low pressure must be separated from the higher pressure region, necessary for a MOT to be loaded from the background vapour of ^{87}Rb . This was achieved by building a double MOT system, as first proposed in [72]; in this scheme a pressure differential is maintained between two separate vacuum chambers, so the higher pressure in the first chamber allows a faster loading into the *collection* MOT, and consequently a larger flux of cold atoms into the second chamber, where the magnetic trap is loaded from the so-called *science* MOT. As a collection MOT we used a pyramid MOT (see section 3.5).

The pyramid is placed in a stainless steel cylinder with a large (10 cm diameter) glass window on the side where the trapping laser beam enters, and a stainless steel pipe that connects this chamber with the science cell vacuum system on the other side. A schematic of the vacuum system is shown in fig. 3.1.

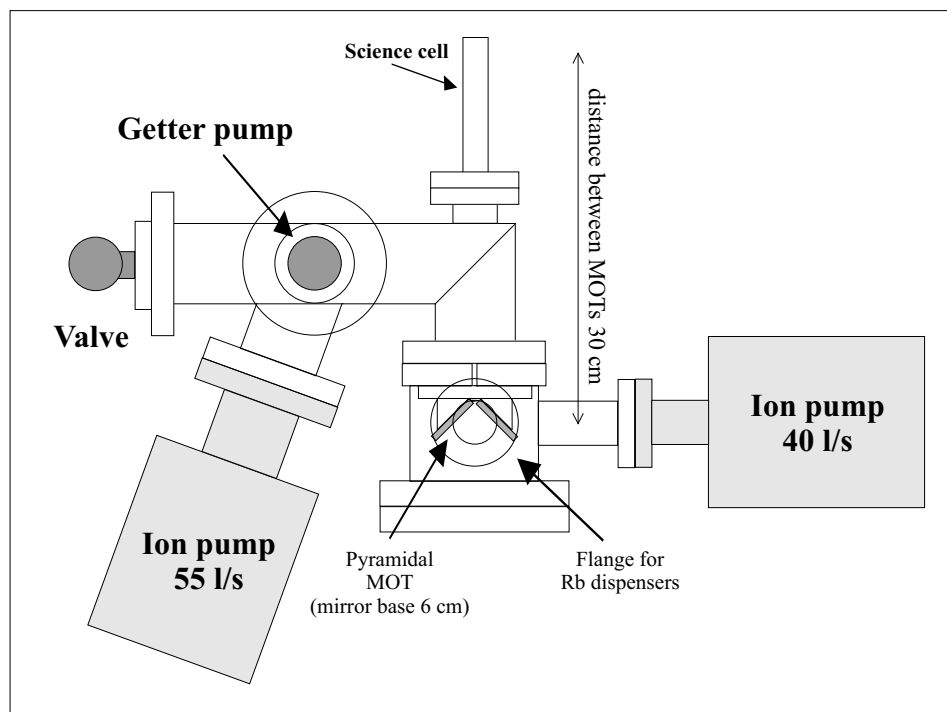


Figure 3.1: Vacuum system. The feedthrough to the getter source (not shown) is connected to a flange on top of the custom-made piece for the pyramidal MOT

The chamber containing the pyramid is attached to a 40 ls^{-1} ion-pump (VacIon Plus 40 by Varian), which maintains a pressure of 10^{-9} Torr. The science chamber has a 55 ls^{-1} ion-pump and the getter pump to maintain a lower pressure. The differential pumping tube has diameter $D = 5$ mm and length $L = 17$ mm. The conductance between the two chambers, at low pressure, is determined by two parameters: the number of atoms entering the tube ($\propto D^2$), and the average number of collisions with the walls as the atom goes down the tube ($\propto L/D$

assuming free molecular flow, i.e. mean-free path $\ll D$). At very low pressures this leads to the formula for molecular flow F down a thin tube [73]:

$$F = \frac{65}{\sqrt{M}} \times \frac{D^3}{L} \text{ ls}^{-1} \quad (3.1)$$

with D and L expressed in cm. M indicates the relative molecular weight of the gas. For ^{87}Rb it gives $F = 7 \times \frac{D^3}{L} \text{ ls}^{-1} \simeq 0.5 \text{ ls}^{-1}$. The ratio between this flux entering the second chamber and the 55 ls^{-1} pump speed of the ion-pump leads to the two orders of magnitude difference in the vacuum attained in the two systems.

The first BEC experiment in Oxford was built in 1998 [74], and it is still operating. From that experience some key changes were implemented in the new one:

- The pyramid mirrors are as large as can be conveniently fitted in the vacuum chamber in order to have a bigger atom collection region and, hence, to achieve a high atomic beam flux. The present pyramid has a base of 6 cm (compared to the 3.8 cm of the original).
- The distance between the two MOTs is about 30 cm, while in the old design it was 65 cm. This shorter distance means that a bigger fraction of the atoms reaches the second MOT.
- A non-evaporable getter (NEG) pump is used to help reach and preserve a very low pressure, instead of a titanium sublimation pump.

The new experiment has bigger ion pumps: 40 and 55 ls^{-1} compared to 25 and 40 ls^{-1} of the old experiment. Also the differential pumping tube has a lower conductance, 0.5 ls^{-1} compared to the 1.6 ls^{-1} in the old experiment. The NEG pump (SAES CapaciTorr-CF35, Cartridge C-400-DSK-St172) works through a chemical reaction, adsorbing active molecules impinging on the getter. It needed to be activated during the bakeout of the vacuum system by heating the getter to $400 \text{ }^\circ\text{C}$ for about an hour. One more novel feature of this experiment is that the whole vacuum system is mounted on its own breadboard and can be wheeled on a track attached to the optical table. This allows the system to be moved to the edge of the table (to be connected to the turbo molecular pump or to be baked out) by just sliding it from amidst the magnetic trap, without the need to remove the coils and the optics around the cell. We have appreciated the usefulness of this feature that allowed a quick bakeout still leaving the laser beams well aligned when the cell was wheeled back to its original position.

3.1.1 Rubidium dispensers

The rubidium source for the experiment is a dispenser (SAES Getters Rb/NF/7/25 FT10+10) located just above the pyramid mirrors. The chemical reaction that

releases rubidium is activated by heating when a current of 2.6 A flows through the dispenser. The current reaches the getter inside the vacuum through a high current feedthrough attached to the top flange of the chamber. Two of these dispensers are mounted in our setup, so that when one of them runs out of rubidium we can switch to the other without having to open the vacuum chamber. We switched to the second dispenser last year, during the course of the work described here.

The dispensers are designed for rapid deposition of large amounts of Rb, at an operating current of 6 A. The datasheet does not give a lifetime for operation at lower current, but the experience of other groups using similar getters, and ours, suggests that it is about 2 years of operation 10hrs/day at about 3 A. Initially we operated the dispenser at 2.8 A and, by the time we had to switch to another set, we had to operate it at 3.5 A in order to obtain a constant release rate of Rb. The current is provided through a precision DC power supply (*Thurlby Thandar TSX3510* 35 V-10 A) set in current mode.

3.2 Laser sources

The use of semiconductor laser diodes for laser cooling is now widespread as they are very compact and are readily available in the spectral region required for the cooling of Rb and Cs atoms. Laser diodes were first used for the cooling of caesium atomic beams [75], and later also for 3D trapping of caesium atoms [76].

To perform laser cooling with diode lasers though, one needs to narrow the linewidth of the radiation and lock its frequency to a particular optical transition. Performing these operations on a commercially available laser diode using standard techniques leaves us with insufficient power to cool the atoms of a double MOT system. Therefore to obtain the necessary laser power we adopt a master-slave configuration, in which the frequency stabilization is performed on one laser (the master) and transferred, by means of the optical injection, onto a second laser (the slave); the full power of the slave laser is available for experiments. Details of this configuration can be found in many of the previous thesis from the laser cooling group.

3.2.1 Master lasers

The master laser is a grating-stabilized laser diode whose linewidth has been reduced by means of an external cavity obtained with a diffraction grating mounted in the Littrow [77] configuration to auto-inject the diode exploiting optical feedback. This also helps to eliminate mode jumps in the region around the hyperfine transition that we use for laser cooling.

This transition, for ^{87}Rb (as for most alkali atoms), is the D2 line. The hyperfine structure of ^{87}Rb is described in appendix A. The $5\ ^2S_{1/2}\ F=2 \rightarrow 5\ ^2P_{3/2}\ F'=3$ transition is a closed one, that only allows decay back to the initial level. In reality

it is not fully closed, because there is also off-resonant excitation to the $F' = 2$ state. We use light red frequency detuned from the $F = 2 \rightarrow F' = 3$ transition by 18 MHz. This leads to a ratio in excitation rates of about 200. Therefore, once in every 200 fluorescence cycles, the atoms are excited to the $F' = 2$ state, from whence they may decay to the lower hyperfine ground state, $F = 1$, and so be lost from the cooling process. Since many more than 200 photons are scattered, these atoms must be *repumped* back into the cooling cycle by driving a transition out of the level $F = 1$ and back into the $F = 2$. This *repumping* light is provided by a laser tuned on the $F = 1 \rightarrow F' = 2$ transition. The power necessary for this task is small compared to the power needed for the cooling. For both MOTs we found that an intensity about 20 times less than that of the cooling light was adequate. The frequency difference between the laser light needed for repumping and that used for cooling is approximately equal to the hyperfine splitting of the ground state (that is about 6.8 GHz).

To produce light at the frequency of the cooling transition we use a commercial (grating-stabilized) external-cavity diode laser (ECDL) by TUI-Optics, locked to the cross-over between the $F = 2 \rightarrow F' = 1$ transition and the $F = 2 \rightarrow F' = 3$ transition (as explained in the next subsection). For the repumping light we used a home-made ECDL. Both lasers have a similar construction (L. Ricci et al. [78], see also [74]). Some of the features relevant to this specific experiment are listed in what follows. The diodes are Sanyo DL 7140-201 specified for $\lambda = 785$ nm, $P = 70$ mW. For the external cavity we use a blazed grating for 750 nm and 1200 lines/mm. The light on the first diffracted order is used as the feedback to the diode laser. A piezoelectric crystal is placed behind the grating to allow modulation of the length and angle of the external cavity. To observe the fluorescence in a rubidium glass cell, and get the lock-in signal, the current is set close to the operational value specified by the manufacturer, and the temperature of the diode, regulated by a Peltier effect heat pump, is stabilized within a tenth of a degree Celsius and set a bit colder than room temperature using a commercial temperature controller (Newport, model 350). When fluorescence is found (by adjusting the orientation of the diffraction grating), the temperature is regulated so that the same wavelength is provided by operating the laser with a current close to the maximum operational value. The laser from TUI-Optics comes with its own controller (model no. DC 100), which has both a current driver (model no. DCC 100/500 mA), and a temperature controller (model no. DTC 100/30W).

3.2.2 Frequency stabilization

To provide a reference frequency for locking the lasers we use Doppler-free saturation spectroscopy. The frequency stabilization is performed by a fast feedback loop on the diode current, and a slow feedback loop on the voltage applied to the piezoelectric crystal (PZT). The voltage applied to the PZT is scanned to produce

a spectrum like that shown in fig. 3.2. These signals are used to lock the laser frequency to the centre of a chosen Lamb dip. The cooling transition, as mentioned earlier, is locked to the crossover between the $F = 2 \rightarrow F' = 1$ transition and the $F = 2 \rightarrow F' = 3$ transition.

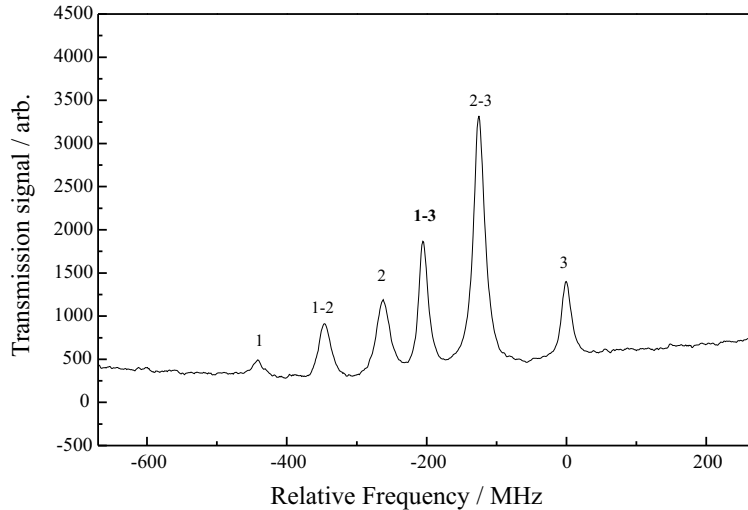


Figure 3.2: Saturated-absorption spectrum of the $|F = 2\rangle \rightarrow |F'\rangle$ transitions (of the $5^2S_{1/2} - 5^2P_{3/2}$) in ^{87}Rb . What is actually displayed is the transmission of the probe beam of the saturated-absorption scheme, from which the Doppler profile has been subtracted.

The numbers indicate F' and cross-overs are labelled by both excited states.

We have the possibility to dither the current driving the diode with a small amplitude, at 100 kHz, to produce a small frequency modulation. When the frequency of the laser is resonant with one of the absorption peaks, the frequency modulation produces an amplitude modulation on the photodiode. The lock-in electronics is used to generate a dispersion signal from this modulation which is integrated and used as feedback for the diode current and the amplifier for the PZT. This system allows us to keep the laser locked for several hours in absence of external mechanical noise on the optical table. The staff of the Electronics Workshop of the Physics Department designed and built both the lock-in electronics (EW 1225) and the piezo driver (EW 1145).

3.2.3 Slave lasers

Once the light has been prepared, i.e. the frequency has been selected and stabilized, it is used to optically inject the slave lasers. These are a pair of diodes (Sanyo DL7140-201) mounted on a home made support which holds the diode itself and its objective (used to collimate the output beam). They are temperature stabilized with a Peltier effect heat pump and a thermistor, in the same fashion as

the extended-cavity laser. Their temperature controllers were made by our electronics workshop. To optically inject the slaves we have to carefully align about 1 mW of master light going into the slave laser in such a way that the radiation of the two diodes is superimposed. This operation transfers the frequency stability of the master onto the slave; it can be verified that the frequency of the slave laser follows that of the master by sending the light from the slave through a cell containing rubidium vapour, and then onto a photodiode, to observe that the absorption spectrum reproduces the one obtained with the master light.

3.3 Optical bench layout

Fig. 3.3 shows a schematic of the optical table. Let us start its description by following the path of the radiation output by the diode lasers. To improve the laser beam's coupling into the optical elements which follow, the elliptical profile of the output beam is made circular by a pair of anamorphic prisms. It then passes through an optical isolator that prevents feedback of light onto the diode laser from any reflections, and prevents the light coming from the slaves from upsetting the master. After the optical isolator the power is typically 25 mW. A polarizing beam-splitter cube divides the beam into two parts. A tiny fraction (13 μ W) goes to the Rb cell for saturation spectroscopy. The rest of the power is sent to optically inject the slave lasers, and to the optical pumping and imaging fibre. At each stage the fraction of light used for a specific purpose can be adjusted by changing the orientation of a half-wave plate in front of the cube.

At the first stage 2.5 mW of light, necessary to inject the pyramid slave, are selected and sent through an acousto-optic modulator (AOM1) used in a cat-eye configuration. A crystal inside the AOM vibrates at a frequency Ω_{AOM} , controlled by a Voltage Controlled Oscillator (VCO), which is set so that light to the pyramid slave will be at a frequency δ_{PYR} away from the $|F = 2\rangle \rightarrow |F' = 3\rangle$ cooling transition resonance frequency. Fig. 3.4 shows details of the frequencies at each stage. The AOM provides an experimental adjustment to finely tune the frequency of the cooling light. The VCO sends an RF signal to the AOM at $f_{\text{RF}} - \delta_{\text{PYR}}/2$ (where $f_{\text{RF}} = 107$ MHz). By aligning the beam onto the AOM at the proper Bragg angle 75% of the power goes into the -1st diffraction order (the 0th and the +1st orders are blocked). This diffracted beam is retro-reflected back through the AOM so that it undergoes another shift of frequency $f_{\text{RF}} - \delta_{\text{PYR}}/2$, and then it optically injects the pyramid slave laser. In the double pass through the AOM and extra optics about 40% of the power is lost. So the actual injecting power is about 1.5 mW. The slave laser beam goes through a pair of anamorphic prisms, an optical isolator, and then on towards the pyramid.

The portion of the light from the master laser transmitted by the pyramid selector cube goes on to the next stage. Another polarizing beam-splitter cube sends the light to AOM2 (also in the cat-eye configuration) to select the frequency

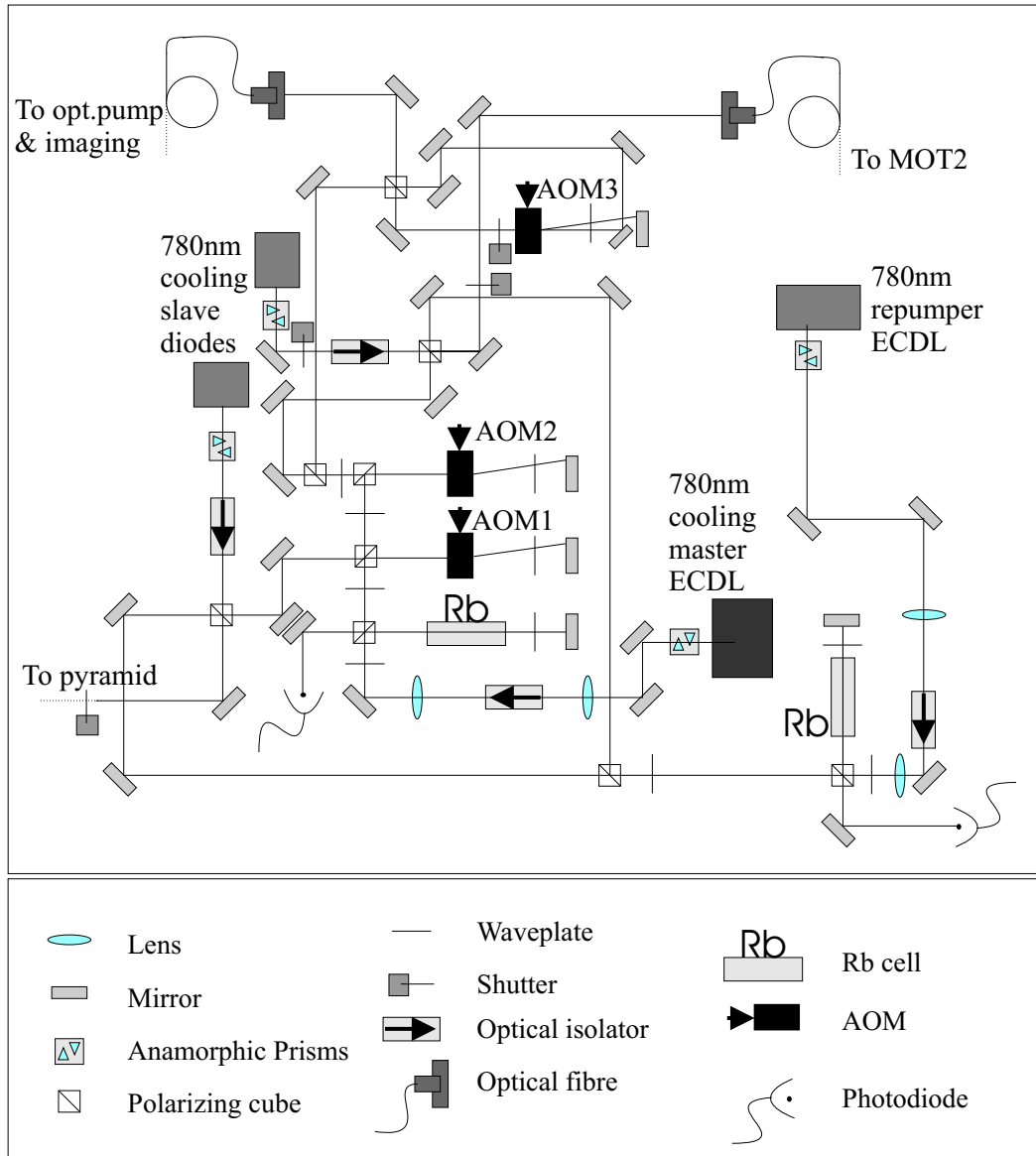


Figure 3.3: Schematic of the optical table.

in the same fashion as the previous one. The beam that injects the slave laser for MOT2 has a power of 0.35 mW. The light from this second slave laser is coupled into a polarization-maintaining optical fibre that transports it to the optics around the cell of the second MOT. The fibre serves two other important purposes: it cleans the spatial mode of the laser beam (at the expense of about 40 – 50% of the power), and guarantees that any change made on the laser setup does not require the MOT2 beams to be re-aligned (only the fibre injection needs to be optimized).

The repumper light follows a similar path to the cooling light up to the saturated absorption setup. Then it splits into two paths at a polarizing cube: a

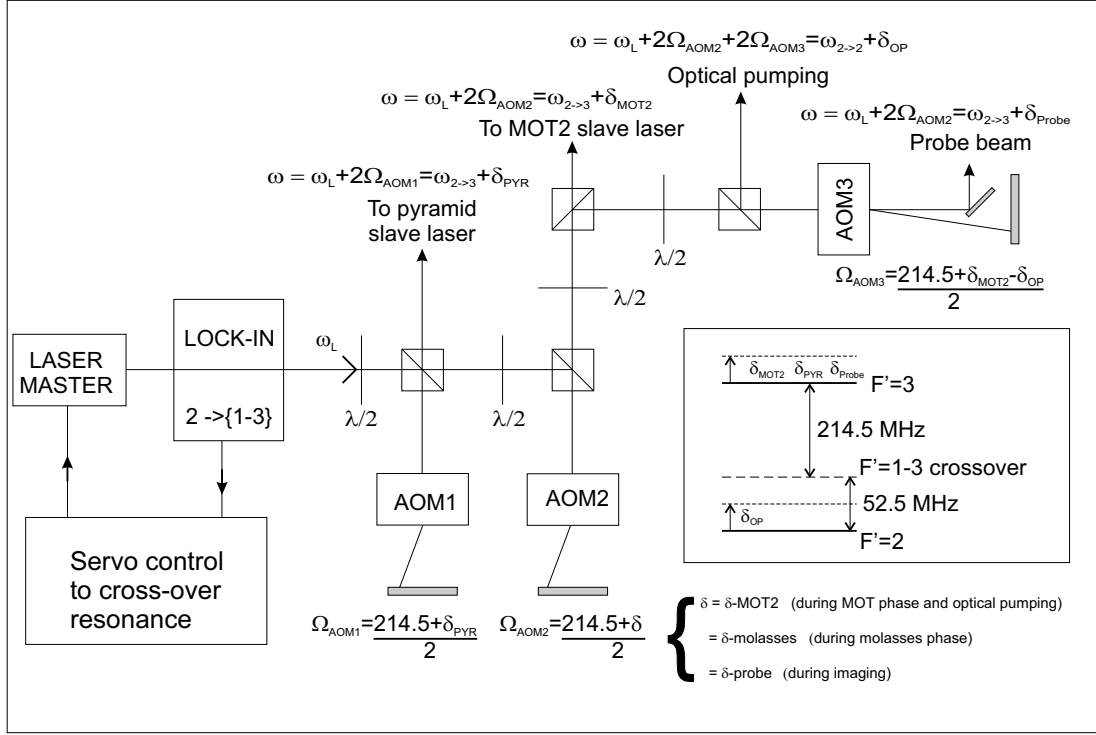


Figure 3.4: Diagram of the laser frequencies manipulation using AOMs.

fraction (3.5 mW) is superimposed with the pyramid cooling light and the rest (5.5 mW) is combined with the cooling light for the second MOT and coupled into the fibre. The superposition of the repumper light with the main cooling light is made with a pair of mirrors and a cube. Mechanical shutters along the various paths serve to make sure that no light from the lasers reaches the cell during the evaporation in the magnetic trap (the scattering rate for photons should be much less than 0.01 s).

The light from the master laser is also used for the optical pumping and the imaging. This light is taken after the double pass through AOM2 and, after 0.35 mW of power have been selected to inject the MOT2 slave, the rest of it (8.5 mW) is sent to a third AOM. We need two different frequencies at different times. To probe we need light resonant with the $|F = 2\rangle \rightarrow |F' = 3\rangle$ transition, which is very close to the frequency coming from AOM2. Therefore for the imaging we use the 0th order of AOM3 and set AOM2 to make the light resonant with the $|F = 2\rangle \rightarrow |F' = 3\rangle$ transition. To optically pump the atoms into the $|F = 1\rangle$ hyperfine ground state just before loading the magnetic trap, we need light tuned on the $|F = 2\rangle \rightarrow |F' = 2\rangle$ transition, minus an optical pumping frequency detuning δ_{OP} . This is achieved using AOM3 driven by the frequency specified in fig. 3.4. To have only one frequency at a time coupled into the optical fibre that is used for both imaging and optical pumping, we control a mechanical shutter, which acts

as a frequency selector, using the same TTL signal used to enable AOM3. This is set up in such a way that when AOM3 is on, the residual 0th order is blocked, while the -1st makes its double pass through AOM3 and then is injected into the optical fibre. When the AOM3 is off, the frequency selector allows the 0th order to be reflected by a mirror and then sent into the optical fibre.

3.4 Magnetic fields

This section describes how we produce the magnetic fields for the experiment. These are:

- Two quadrupole magnetic fields for the pyramid MOT and the second MOT.
- A rotating bias field that is added to the quadrupole field in the second MOT to create the TOP trap.
- Homogeneous magnetic fields are necessary to cancel any external magnetic field on the atoms in all spatial directions around the centre of both cells. That is particularly important during the optical molasses cooling phase.
- A large homogeneous field, of more than 1000 G, is necessary to observe the Feshbach resonance, because the one we chose to work with occurs at 1007.34 G [34]. This field must be stable to about five or ten parts per million.
- Additional coils are required during the evaporation, to be driven with an RF field to expel the hot atoms from the trap.

3.4.1 Pyramid quadrupole

To make the pyramid MOT we use a quadrupole field with an axial gradient of about 10 G/cm. The large size of the coils needed to fit round the chamber (10 cm diameter) means that a high number of current-turns is needed, and consequently considerable heat is dissipated. To meet these requirements we wound two coils, each with 13 turns of a hollow copper pipe encased in a glass-fiber cladding, around the steel chamber containing the pyramidal mirrors. Refrigerated water flows through the coils. The coils have a mean diameter of about 13 cm, and are separated about 7 cm along their axis. This geometry gives a nearly anti-Helmholtz configuration and, for 30 A current, generates a magnetic field gradient of 10 G/cm at the centre of the trap.

3.4.2 Shim coils

The shim coils, or nulling coils, are used to cancel the effect of external magnetic fields. The main contribution to spurious magnetic fields in the lab comes from the Earth's field of about 1 G. Such field can easily be produced by coils with a large diameter and modest current.

Pyramid shim coils

These coils position the zero of the quadrupole magnetic field in line with the hole in the pyramid. There are three of them on our setup: one along the direction of the pyramid beam, and the other two in the two orthogonal directions. The three coils are identical, and have been wound by the Oxford University Magnet Group. Each coil has six layers of 18 turns for a total of 107 turns per coil. They are circular with a diameter of 17 cm. To drive them we use home made power supplies which can provide each coil with up to 2 A (EW 1145 and EW 1225, both made at the Electronic Workshop of the Department of Physics); these coils provide 4.5 G/A (at the centre of the pyramid).

Science MOT shim coils

To compensate external field around the centre of the second cell we used 3 pairs of Helmholtz coils. They all have different number of turns, and the current (provided by the same two current supplies used for the pyramid shim coils) has been determined by looking at the expansion of the MOT after switching off the quadrupole gradient, to have an idea of the compensation during the molasses phase. We have recorded the value of the temperature of the cloud loaded in the TOP trap as a function of the current through the shim coils, and chosen the current for which the temperature was lowest. The coils that compensate the field in the direction of gravity were wound around the quadrupole coils. Details of the geometry of the coils setup are summarized in table 3.1.

Spatial direction	Turns per coil	Size (cm)	Distance from MOT2
x	35	(side length) 17	± 14 cm
y (atoms flux)	35	(side length) 8	± 9 cm
z (gravity)	30	diameter ≈ 5	wound around quadrupole coils

Table 3.1: Summary of the geometry of the MOT2 shim coils.

Very recently the shim coils for the z (vertical) direction have been switched to anti-Helmholtz configuration to generate a magnetic field gradient (that is used

in a Stern-Gerlach type experiment described in chapter 8). Therefore we had to wind another z shim coil. For space reasons we wound only one square coil of side length 18 cm, and placed it 13.5 cm below the MOT2. For this bigger diameter and distance from the MOT, 115 turns were required to produce the same field for a similar current as in the previous coils.

3.4.3 TOP coils

The rotating field that is added to the quadrupole field to create the TOP trap (as described in chapter 2) is provided by two pairs of coils. These two pairs are placed around the glass cell orthogonal to each other, and with their symmetry axes in the horizontal plane. The TOP trap coils employed in this experiment were built some years ago for a previous experiment with caesium atoms, and details of their construction can be found in [79].

These coils produce a relatively large field (~ 44 G) in the horizontal plane. This is achieved by using a compact geometry to ensure a small number of turns and small power. Moreover they occupy very little space around the cell, so that the quadrupole coils can also be close. The TOP coils are made of two pairs of rectangular coils of 6 turns each. One pair just fits inside the other one (see fig. 3.5). Attached to each coil there is a thin wire, which makes a single turn around it and acts as a pick-up coil to monitor the magnetic field produced by the TOP coils.

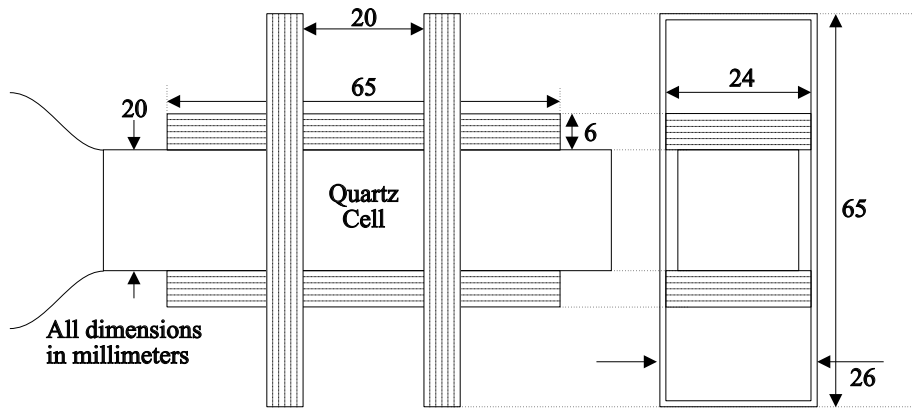


Figure 3.5: A diagram illustrating the geometry of the TOP coils.

They are operated with a signal that is a sine on one pair and a cosine on the other. The frequency of these signals is 7 kHz and the resulting field rotates in the horizontal plane at this frequency. The electronics used to generate the sinusoidal signal is described in details in [80], and only brief details are given here. It consists of three parts: a phase shifter, a Schmitt trigger, and a voltage controlled amplifier.

The phase shifter creates a cosine wave from the sine wave coming from a normal function generator. The Schmitt trigger synchronizes the computer that controls

the experiment with the phase of the rotating field; this is crucial in processes such as optical pumping. The voltage controlled amplifiers control the amplitude of the sine and cosine (with a voltage from the computer). These components are all placed in one box to reduce external noise.

The signal thus generated is too weak to produce the field intensity required. Therefore, it is sent through an audio amplifier (H&H MX1200) that can generate 600 W of output power in a load $R = 4 \Omega$. At 7 kHz the impedance of our TOP coils is dominated by their inductance, i.e. for an inductance $L = 9 \mu\text{H}$ it is $X = 0.4 \Omega$. To match the impedance, and reduce the loss of power, the amplifier is connected to the coils through a transformer. To calculate the transformer ratio we assumed the ideal case in which there is no power loss inside the transformer: $P_1 = P_2 \rightarrow I_1^2 R = I_2^2 X$ leading to the winding ratio:

$$r = \frac{N_1}{N_2} = \frac{V_1}{V_2} = \frac{I_1 R}{I_2 X} = \sqrt{\frac{R}{X}} = 3.2. \quad (3.2)$$

Transformers with this ratio of turns were wound, which, at maximum power, lead to a current into the TOP coils of $I \simeq 40 \text{ A}$.

3.4.4 RF coils

The coils used to induce radio-frequency evaporation during the last stage of the evaporation process are made of 5 turns, wound between the quadrupole coils and the TOP coils. They are circular and have a radius of 1.8 cm. A frequency generator (SRS DS-345), to which they are attached in series with a 50Ω resistor (that helps to match the impedance at low frequencies, and prevents large changes in amplitude with frequency), is used to drive them with an RF signal.

3.4.5 Quadrupole and Feshbach bias field coils

This section describes a piece of apparatus which plays a central role in the experiment as it provides the magnetic field gradient during the evaporation, as well as the uniform magnetic field needed to produce the Feshbach resonance that we want to use to make molecules.

These coils were originally designed as quadrupole coils for a TOP trap, but, when we decided to engage in the search for the Feshbach resonance, we sought the possibility of producing the high magnetic fields required by reversing the current in one of the coils and, in this way, switch from anti-Helmholtz to Helmholtz configuration. Given the geometry of the coils these configurations are only approximately achieved.

The coils had to be used for both purposes because the compactness of our setup made it impossible to find enough space near the cell to wind a new set of Helmholtz coils.

The geometry of the coils and the water-cooled block around which they are wound is sketched in fig. 3.6 (see also [79]). Water cooling is provided by the same refrigerated water source as used for the pyramid quadrupole coils. The water flows inside the metallic block to carry away the heat. Each coil has 441 turns of 20 SWG wire, wound in three grooves of the cooling block. The minimum separation of the two blocks is determined by the size of the cell plus the thickness of the TOP and RF coils. They generate a field with an axial gradient of about 390 G/cm when operated at $\simeq 12$ A. A hole with a diameter of 15 mm in the middle of each block allows the vertical beam of the MOT to reach the cell.

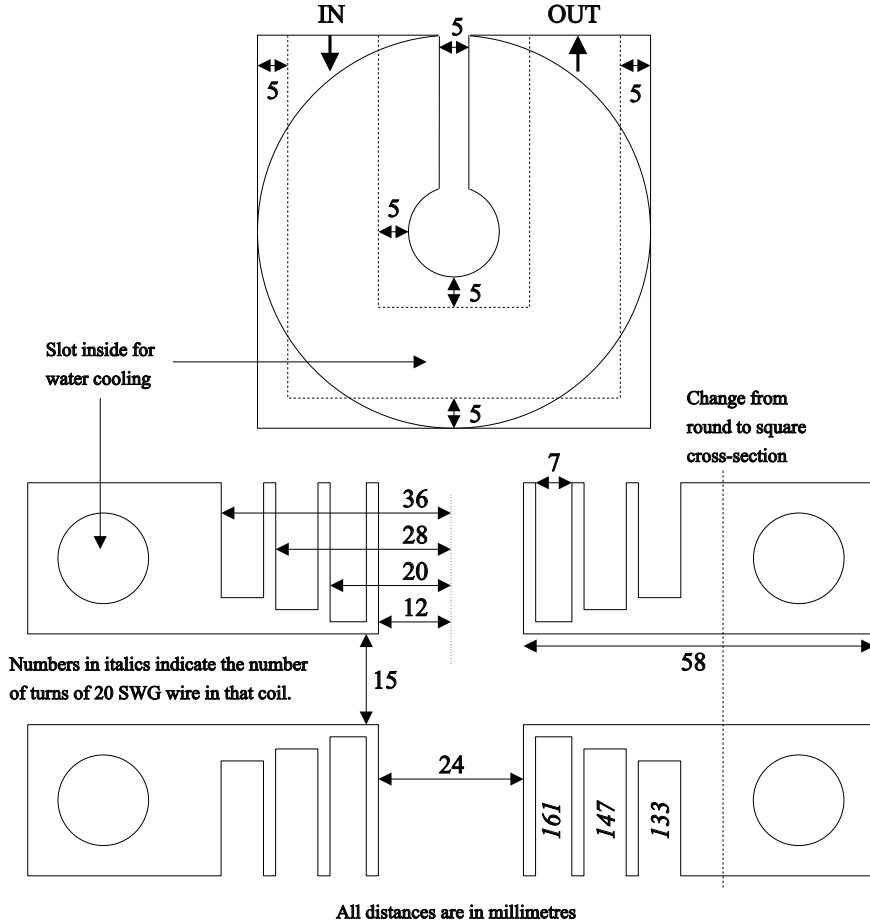


Figure 3.6: A diagram illustrating the geometry of the quadrupole coils.

During the evaporation we need to run them at 12 A for about a minute. This heats the wire considerably, increasing the initial total resistance of both coils in series (3.3Ω) to a value requiring more than the maximum value (36 V) achievable with our first power supply (Kepco ATE 36-30M). So at a later stage we decided to operate it from the start at 10.85 A, which yields a field gradient of 350 G/cm. This gradient was adequate to achieve BEC.

When we started exploring the Feshbach resonance at 1007 G, as we needed nearly 17 A to be passed through the coils to produce such a field, a pair of power supplies (Farnell H60/50) connected in series was used instead. The coils are not designed to operate at such a high current, but we only needed it for less than half a second. This was just achievable by waiting about 3 minutes between each run, to allow the coils to cool down to about 30 °C. This severely reduced the rate at which data were acquired, as the loading of the MOT had reached its stationary state after about half that time.

Reversal of the current

To switch from a Helmholtz to an anti-Helmholtz configuration, we needed to invert the current in one of the two coils. This was done using four solid state relays (Crydom D1D20), which are essentially diodes that can bear up to 20 A. A schematic of the configuration of such a *switch box* is in fig. 3.7.

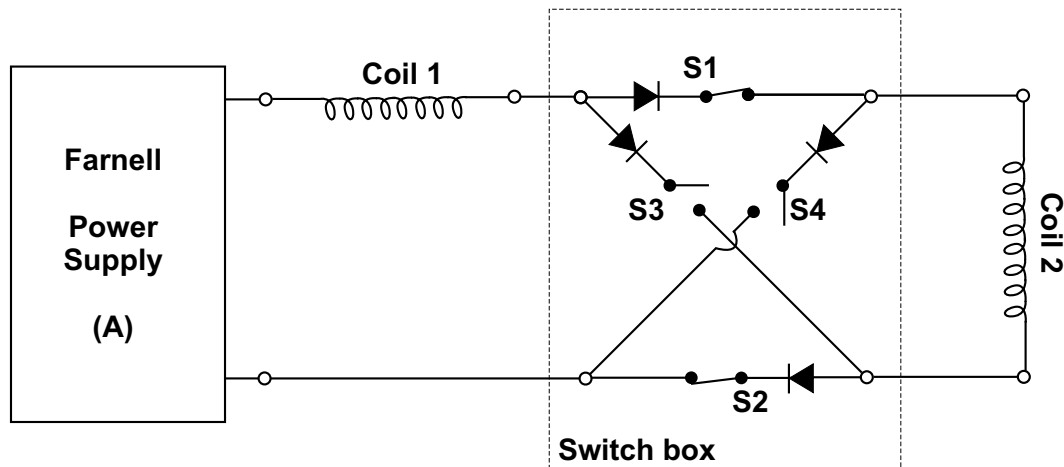


Figure 3.7: Schematic of the switch box. S1 and S2 closed, and S3 and S4 open: anti-Helmholtz, while S3 and S4 closed, and S1 and S2 open: Helmholtz.

When the switches S1 and S2 are closed, and S3 and S4 are open, the coils are in anti-Helmholtz configuration, while when S3 and S4 are closed, and S1 and S2 are open, the coils are in Helmholtz configuration. They are controlled by a TTL signal coming from the computer. Because S1 and S2 conduct high currents during nearly one minute of evaporation, when the coils are in the anti-Helmholtz configuration they become fairly hot, even though mounted on heat-sinks.

Calibration of the magnetic field

It was important to calibrate the field from the coils when in the Helmholtz configuration in order to know the precise field of the Feshbach resonance around 1007 G.

This was achieved with RF spectroscopy of the Zeeman sub-levels. RF radiation induced spin flips to the other m_F states within the $F = 1$ level, and these transitions were detected by applying a magnetic field gradient that spatially separated the different Zeeman components, and by measuring the fraction of atoms in each component. Precise localization was achieved by moving the position of the ramp to maximize the transfer, whilst making the range of the sweep as narrow as possible. The result of such measurements are shown in fig. 3.8. The offset has to be interpreted as a residual magnetic field at zero current of -0.1 ± 0.03 G.

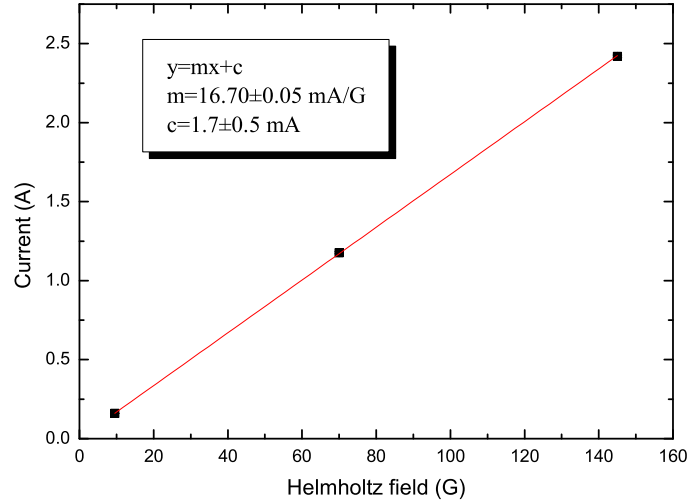


Figure 3.8: Calibration of the Helmholtz field. The value on the x axis is the field in Gauss as obtained through the Breit-Rabi formula from the frequency of the RF transfer.

To associate the frequency applied with a specific field value we used the Breit-Rabi formula to calculate the splitting of the hyperfine levels as a function of the field:

$$E_{M_J, M_I} = -\frac{h\nu_{HFS}}{2(2I+1)} - g_I \mu_N B M_q \pm \frac{h\nu_{HFS}}{2} \left\{ 1 + \frac{4M_q x}{2I+1} + x^2 \right\}^{1/2} \quad (3.3)$$

where $h\nu_{HFS} = A_J(I + \frac{1}{2})$ is the separation of the hyperfine level at zero field, $M_q = M_I \pm M_J$, and x is a dimensionless parameter defined as:

$$x = \frac{(g_J + g_I \frac{m}{M}) \mu_B B}{h\nu_{HFS}} \quad (3.4)$$

where m and M are the electron mass and the nucleus mass respectively, and g_J and g_I are the Landé g-factors for J (total angular momentum) and I (nuclear spin) respectively.

To make these measurements we loaded the BEC into the standing wave, and then reversed the current of one quadrupole coil to have a Helmholtz configuration. Subsequently we ramped the current to obtain the starting field for the ramp (before the calibration was done these field values were calculated from the geometry of the coils), and applied a constant frequency using a 10 turns coil placed in front of the atoms and with its axis on the horizontal plane (from signal generator Agilent Technologies, E8247C PSG CW Signal Generator). While this signal was being applied, the current through the coils was ramped up to the final value. Then the frequency signal was turned off, as well as the optical trap, and a gradient of 14 G/cm was applied for 4 ms to separate spatially the atoms with different m_F . We then allowed a further 4 ms time of flight, and then imaged the clouds on the CCD camera. This procedure was repeated for each of the 3 different frequency values; and for each of them, to obtain a narrow current range, we reduced the range over which the field was being swept, and the amplitude of the RF signal. Error bars in fig. 3.8 are smaller than the size of the point symbol.

We were not able to take calibration points at higher fields, and we believe that the reason for this was that at higher frequencies the antenna we were using was not properly impedance-matched so did not provide enough power to drive the transition. From the fit we can see that to obtain 1000 G we have to pass 16.7 A through the coils. The error of 0.3% on the gradient limits the precision with which we can state the central value of the resonance to about 3 G. The stability of the current at that value, however, is 100 times higher. We did not change the antenna because we did not have any specific reason to require an accuracy higher than 3 G to identify the resonance.

Control and stabilization of the magnetic field

In the case of ^{87}Rb the resonances are all relatively narrow, and the widest (at 1007 G) is only 170 mG wide. This is 4 orders of magnitude smaller than the value of the field and, if we want to be able to resolve it, we need to be able to produce a field of 1000 G and keep it stable better than 10^{-4} . Since the field is proportional to the current through the coils, we have to keep the current stable up to a few parts in 10^5 .

The power supply in current-regulation mode only had a stability of 10^{-3} (from the power supply specifications), and so would be totally insufficient for our purpose. Therefore, we decided to add an electronic feedback circuit to stabilize the current to the level that we needed. A schematic representation of the stabilization circuit is shown in fig. 3.9 (the stabilization circuit is used to control the amount of current that flows through the coils).

In the new scheme the power supply is set in voltage mode, therefore it provides a fixed output voltage, that is controlled by the computer. The actual amount of current through the coils is regulated using a MOSFET as a variable resistor whose

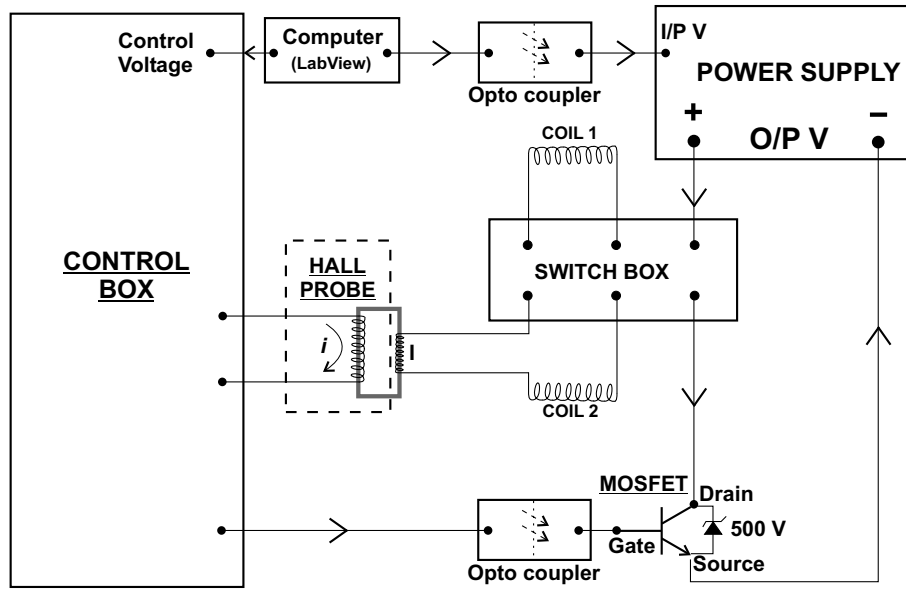


Figure 3.9: Schematic representation of the magnetic field stabilization circuit.

value is set by a feedback loop. The stabilization circuit has three key elements:

- A Hall probe, which senses the current flowing through the coils. Its output is a current proportional to the current through the coils.
- The control box, which converts the output of the Hall probe into a voltage, and compares it to the control voltage that corresponds to the current that we want to pass through the coils. The difference between these voltages is used to determine the voltage to be sent to the gate of a MOSFET
- A MOSFET, which regulates the amount of current that flows through the coils.

Some operational details about the Hall probe and the MOSFET are presented here, while the main electronic features of the control box are described in appendix D.

To check the field stability achieved with this setup, we added a 0.05Ω shunt resistor, which can carry up to 30 A, in series with the MOSFET-coils circuit, and we measured the AC component of the current across the shunt using a multimeter HP-34401A. The amplitude of the AC component measured across the shunt was 5×10^{-5} times the DC component.

The Hall probe

The first element of the feedback loop that stabilizes the current is a Hall-effect current sensor, whose scheme of operation is shown in fig. 3.10. The current that we

want to stabilize flows in the direction of the thick arrow (I_{primary}). This generates a magnetic field that is trapped in a ferromagnetic core making a loop around the current. This magnetic field crosses the semiconductor piece (shaded). A small current generator within the sensor generates a current I_c , that flows across the semiconductor piece in a direction orthogonal to the magnetic field. In such circumstances an electric field arises in the direction orthogonal to both current I_c and magnetic field: this is called the Hall effect. The electric field leads to a potential difference that can be used to control a feedback circuit A to apply a current $I_{\text{secondary}}$ on a secondary coil (N turns wound around the ferromagnetic core). For an appropriate value of $I_{\text{secondary}}$, the magnetic field generated by this secondary coil cancels the field generated by the primary current. Now, when the magnetic field is cancelled inside the ferromagnetic core, the current in the primary coil is N times bigger than the current in the secondary coil (the output of the current sensor), whose value can be obtained by passing it through a known resistor R_{sense} . The voltage V_{sense} across this resistor is strictly related to the current that we want to measure, and can be used as the input of the feedback circuit that stabilizes the primary current to the desired value.

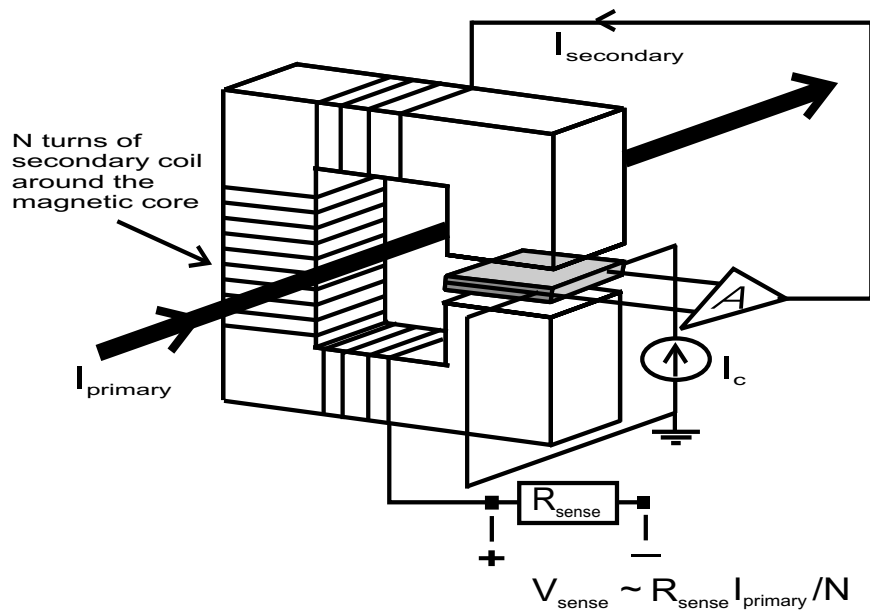


Figure 3.10: Scheme of a Hall-effect current sensor.

Our sensor is made by Honeywell (model CSNJ481). This can take up to 600 A as an input current, and its secondary coil has 2000 turns, so that the output current is limited to 300 mA. We pass about 16.2 A through the coils to produce 1000 G, so we wound the wire 20 times around the hole of the sensor to exploit more of the dynamic range of the Hall sensor and to have a better signal at low current.

The MOSFET

The MOSFET (Farnell, N TO-264) is used as a variable resistor, whose value is regulated by the gate voltage. It can take up to 38 A as a drain current, and dissipates 520 W at room temperature. In practice, the output voltage of the main power supply is set to be higher than it needs to be to ensure there is always enough voltage available to push the required current through the circuit. During the evaporation, when high currents are passed through the coils for up to a minute, the heating in the coils causes their resistance to rise and so the supplied voltage must continually increase even if the current is to remain constant; obviously, for too high an output voltage, the excess power dissipated in the MOSFET overheats it. To protect it against overheating it is mounted on a water cooled brass block.

As a further protection feature for the MOSFET, a Zener diode (500 V breakdown voltage) is inserted between source and drain, so that when the current in the coils is rapidly switched off, any induced e.m.f. between source and drain that exceeds the MOSFET's breakdown value of 600 V will not push current back through the MOSFET itself, but through the Zener diode.

Unfortunately, accidental overheating of the coils on one occasion caused the insulating coating of the coils to melt (thankfully only on a single point), connecting the coils to the optical table that is connected to ground. Instead of winding a new set of coils with all the replacement work that this would have required, we decided to make the melted point the only ground connection in the circuit, and apply a floating voltage to the MOSFET. This was done using an opto-coupling circuit (built using the CHIP *IL-300* by Vishay) to duplicate the gate voltage coming from the stabilization box (that had the same ground connection as the computer signal) into another identical voltage actually applied to the gate of the MOSFET, but without the same ground reference.

3.5 Pyramid MOT

The pyramid MOT is used as a source of pre-cooled atoms with which to feed the science MOT. This preliminary stage is needed because to produce the BEC we use a magnetic trap, which has to be placed in a chamber where the level of vacuum is such that a MOT cannot be loaded by the vapour at room temperature. The choice of a pyramid MOT comes from wanting a cheap, simple, and reliable tool. The original design of its configuration is due to K.I. Lee et al. [81], but it was in Oxford that it was first modified to make it a continuous source of slow atoms with both caesium [82] and rubidium, adding a small hole at the vertex of the pyramid. Details of the function of such a tool can be found in the two references above.

It consists of a set of four mirrors in the shape of an inverted pyramid. There are two square mirrors placed at 90° next to each other, plus two prisms to complete the pyramid. The final result mounted in the vacuum chamber is shown in fig. 3.11.

A hole of $1 \times 2 \text{ mm}^2$ was left at the vertex to allow the cooled atoms to travel to the science cell. The side of the base of the pyramid is 6 cm long. The BK7 glass substrate for the mirrors was coated in our physics department. The coating is a broad-band dielectric coating that has similar characteristics for both s- and p-polarized light, and hence does not affect the polarization of the light.

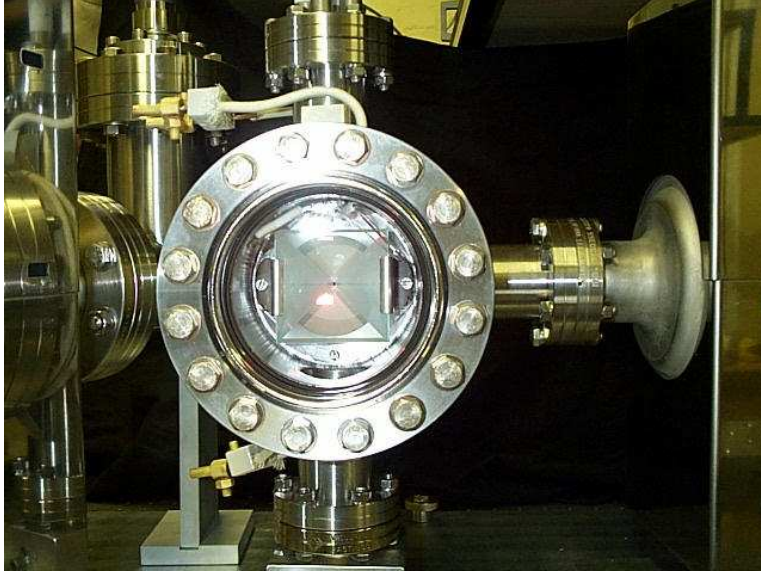


Figure 3.11: The pyramid in which about $2 \cdot 10^8$ atoms are captured in a MOT. The side of the base of the pyramid is 6 cm long.

The pyramid MOT is operated by a single beam travelling along the axis of the pyramid towards its base. This beam contains light for both cooling (59 mW) and repumping (3.5 mW) the atoms. The beam is magnified using a telescope to increase its transverse diameter from 2.8 mm to 43 mm, so that it covers a large portion of the base area of the pyramid ensuring a bigger capture region for the MOT.

As mentioned at the beginning of this section, this is a very simple and effective way to load the science MOT, and the various stages of optimization are now well established procedures in our group. What is important is that they have all been optimized once also the other MOT was operative, to maximize the second MOT's loading rate and its steady state value. The magnetic field gradient is 10 G/cm at the centre of the trapping region. The cooling light is detuned 15 MHz on the red of the $|F = 2\rangle \rightarrow |F' = 3\rangle$ transition. The polarization of the beam is circular, and the reflections on the mirrors of the pyramid make it so that in all points of the trapping region the photons counter propagating in each direction have opposite polarization (σ^+/σ^-).

The flux of atoms to the second chamber is strongly dependent on how well the zero of the magnetic field is aligned with the vertex of the pyramid, and on the

direction of the laser beam that, at the centre, acts as a push beam. The former feature is ensured firstly by centring the quadrupole field and the laser beam on the axis of the pyramid, and then finely positioning it using the shim coils to slightly move the zero of the magnetic field. The latter is controlled by a pair of mirrors which steer the direction of the laser beam, and a CCD camera that monitors the fluorescence of the pyramid MOT: when this is well aligned, the pyramid MOT is not visible on the CCD camera. The pyramid MOT reaches its full loading in about 4 s.

3.6 Science MOT

The beam of slow ^{87}Rb atoms produced with the pyramid travels for about 30 cm, and then is collected and trapped in a second MOT. This second MOT, or science MOT, (denoted MOT2 throughout this thesis) is a standard six-beam MOT.

The three pairs of counter-propagating beams are formed from the light coming out of the optical fibre. About 30 mW of power, including about 1.5 mW of the repumping radiation, comes out of the fibre and is split into six beams. Two of these beams counter propagate along the vertical direction through the centre of the glass cell. The other four form two counter-propagating orthogonal pairs in the horizontal plane.

The quartz cell is attached to the vacuum chamber through a quartz-metal adaptor. The long side of the cell (7 cm) is the one in the direction of the incoming atomic beam from the pyramid, and its section is $2 \times 2 \text{ cm}^2$.

The laser beams have a diameter of about 20 mm, and a nearly perfect Gaussian profile thanks to the mode filtering provided by the fibre. A half-wave plate is placed just before each polarizing beam-splitter cube, to allow regulation of the power-splitting ratio at each step. Each pair must be balanced in power, and the three pairs have similar total power. Finally a quarter-wave plate for each of the six beams makes their polarization circular just before they enter the cell. The helicity of the polarization is chosen according to the schemes presented in chapter 2, and it is such that each counter-propagating pair has one beam polarized σ^+ , and the other polarized σ^- .

A first rough alignment of the MOT beams is done by looking at the superposition of the counter-propagating beams on white paper with an infrared viewer. Once this alignment is good enough for a tiny MOT to be observed, the alignment of the beams, as well as the orientation of the quarter-wave plates, is improved maximizing the fluorescence of the MOT collected by a photodiode.

The main objective is to collect the largest number of atoms in the second MOT, therefore maximizing this parameter (N) was the criterion used to choose the values of the magnetic field gradient and the detuning of the laser beams. The current flowing through the dispenser was also determined by looking at the number of atoms in the second MOT. After an initial linear growth it would reach a

steady state value, and the turning point ($I = 3$ A) was chosen as initial dispenser current. It had to be increased little by little during the following months to ensure constant quantity of rubidium in the pyramid chamber. Figure 3.12 shows the measurements taken during the optimization process, and which lead to the choice of $\delta = -2\pi \times 14$ MHz and $\nabla B = 14$ G/cm as best operational parameters.

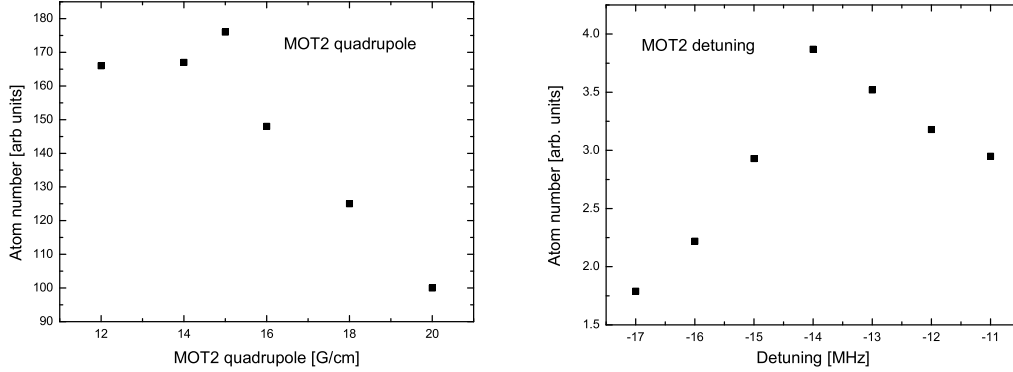


Figure 3.12: Optimization of the *science* MOT parameters. The scan of the field gradient has been done keeping the detuning of the light at $\delta = -2\pi \times 14$ MHz, and the scan of the detuning was performed keeping the axial field gradient at $\nabla B = 14$ G/cm.

The choice of the current flowing through the shim coils was made by looking at the temperature of the molasses. After this optimization process, we can load up to 2×10^8 atoms in the second MOT in about 120 s. The lifetime of the atoms was measured by recording the decay of the fluorescence signal at different times after blocking the pyramid beam. An exponential fit of the data yields a $1/e$ lifetime $\tau = 102 \pm 7$ s, as reported in fig. 3.13. The initial quick decrease in the fluorescence is probably due to light assisted inelastic collisions between two atoms in the MOT, one in the ground level and one in the excited level, that dominate the losses at large numbers being proportional to N^2 . The time constant of the remaining decay is mainly determined by collisions between the trapped atoms and the background vapour, which is proportional to the number N of trapped atoms. For these reasons the first data-point is not included in the fit.

3.7 Imaging system

This section describes how we take quantitative images of the atomic clouds. A description of the analysis performed on the images to extract physical information about the clouds is given in appendix B.

We used the well-established absorption imaging technique to observe our con-

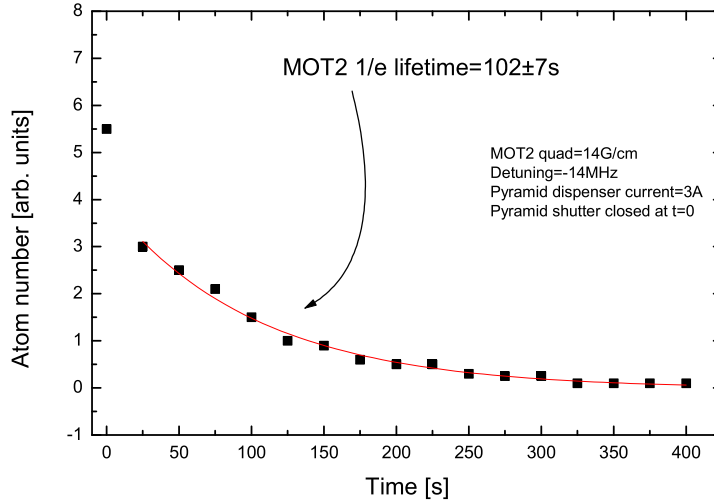


Figure 3.13: Lifetime of the science MOT.

densates. A circularly polarized¹ laser beam resonant with a closed atomic transition is directed onto the atomic cloud (see fig. 3.14). Radiation gets absorbed by the atoms so that a *shadow* of the cloud is cast on the CCD. The absorption profile depends on the density and the shape of the atomic cloud. The absorption of the radiation, as it crosses the atoms in the y direction (under conditions specified below) is described by Lambert's law [83]:

$$I=I_0 \cdot e^{-ky} \quad (3.5)$$

where $k = n\sigma$ is the absorption coefficient, given by the density of the cloud times the absorption cross section, that can be written, in a regime of low saturation, as:

$$\sigma(\delta)=\frac{\sigma_0}{1 + (\frac{2\delta}{\Gamma})^2} \quad (3.6)$$

where $\sigma_0 = 3\lambda^2/2\pi$, that in our case is $\sim 3 \cdot 10^{-8} \text{ cm}^2$, is the cross section for resonant absorption, and Γ is the natural line width of the transition involved. A table of numbers relevant to the optical properties of ^{87}Rb is reported in appendix A. The conditions under which equation 3.5 applies are:

1. The light must be monochromatic, that is to say the linewidth of the laser (during the probe pulse) must be much smaller than Γ .

¹This is to maximize the absorption, when probing in the presence of a polarizing magnetic field.

2. The amplitude of the electric field should vary very slowly on distances of the order of a wavelength.
3. The radiation can be approximated with a plane wave.

The first condition is guaranteed by the locking of our lasers. The second one requires the size of the cloud that we image, and over which the intensity decays, to be large compared to the probing wavelength. This is satisfied because a condensate has a diameter of the order of a few microns. The last condition arises from the consideration of whether the cloud acts as a lens to focus the light: in a regime of low saturation, the Kramers-Kronig relations between refractive index and absorption give a phase shift $\Delta\phi \simeq (\delta/2\Gamma) \ln(I_0/I_t)$, where I_0 and I_t are the incident and transmitted light respectively. For a red frequency detuning of the radiation, the medium becomes equivalent to a lens of focal length $f = 2\pi l^2/(\Delta\phi \lambda)$, where l is the size of the cloud along the direction of propagation of the light beam [84]. Therefore, for the last condition to be satisfied, it is required that $\delta \simeq 0$ (resonant probe beam).

Our probe beam (of measured waist $w_0 = 3$ mm) is resonant with the $F = 2 \rightarrow F' = 3$ transition, and its intensity (0.9 mW/cm²) is about 30% of the saturation intensity. The probe pulse lasts for about 0.2 ms, to prevent saturation when imaging a condensate. During the probe pulse the cloud falls about 30 microns; this effect limits the accuracy of our measurements of the size of the clouds. We have calculated that this effect increases the size of the condensate measured after 15 ms of time of flight to be 20% bigger than if it were not falling. This affects the determination of the size, but not the number of atoms calculated from the picture, and since we do not use the size of the cloud to deduce any relevant physical result, we decided that it is not important to correct for this.

The blurring could be reduced by a faster probing pulse, but that would require more laser power on the camera to have the same signal. This extra power is needed on the camera to use most of the dynamic range of its chip, but would lead to more saturation of the transition. The solution to this could be either to get a new camera with a higher sensitivity, so that a shorter pulse of the same intensity could make use of the whole dynamic range of the CCD, or reduce the magnification so that the the intensity hitting the camera is higher. Currently the magnification enlarges the image of the cloud, and hence the whole probe beam by a factor 2.59, reducing the intensity hitting the CCD by a factor 6.7. This magnification, however, gives images of the condensates that spread over a reasonable number of pixels, even when imaged in trap without time-of-flight expansion. The side length of one pixel is 9 μm , hence the resolution of the imaging system is $9/2.59=3.47$ μm .

3.7.1 Absorption pictures

The absorption imaging technique is a destructive one, i.e. the pulse of resonant light destroys the condensate. To remove the background light from the image of the cloud we must take three pictures. The first records all the light that has not been absorbed by the atoms (I_A). A second (bright) picture is taken in exactly the same conditions as the first one, but without atoms, therefore it records the whole intensity of the light (I_B). A third (dark) picture is taken without firing the probe, to record the background light (I_D). A computer program subtracts the last picture from the first two, and then takes the ratio of the two resulting frames. This ratio, $T(x, z) = \frac{I_A - I_D}{I_B - I_D}$, represents the *transparency* of the medium. Its reciprocal is the *opacity*, and the logarithm of the opacity is, by definition, the *optical density* of the medium. Therefore, the optical density $D(x, z)$ is obtained from the transparency $T(x, z)$, using the relationship [2]:

$$D(x, z) = -\ln(T(x, z)). \quad (3.7)$$

The data are recorded as an array containing the optical density for each pixel. These data are used to extract physical information on the cloud such as density, number, and size (as discussed in appendix B).

3.7.2 CCD camera

To acquire the images we use a Spectra Source CCD camera (*Teleris 2*) with a Kodak CCD array of 768×512 square pixels each with a side length of $9 \mu\text{m}$. The overall size of the chip is $6.91 \times 4.6 \text{ mm}$. It has a saturation capacity of 8.5×10^4 electrons/pixel, and a specified quantum efficiency of about 40 % at 780 nm. The very simple software that controls the acquisition of the frames through the computer (and clears the CCD array before acquiring each frame) allows acquisitions every 2 s. This means that the shortest time between each picture is about 2 s, thus the probe beam intensity must be very stable for about 5 s. The quality of the background cancelation in our images shows that this is not a problem with our apparatus.

The following simple calculation supports the choice of the intensity. Each pixel must deliver less than $8.5 \times 10^4 e^-$, otherwise it will be saturated. If we aim for half of this value ($4 \times 10^4 e^-$), with a quantum efficiency of 40 %, we require about 10^5 photons. The surface of each pixel is $8.1 \times 10^{-7} \text{ cm}^2$, therefore the energy needed on the chip per cm^2 is $u = \frac{hc}{\lambda} \frac{N_{\text{photons}}}{S_{1\text{pxl}}} \approx 3 \times 10^{-9} \text{ J/cm}^2$. With a pulse that lasts 0.2 ms, the intensity needed to shine this energy on the CCD is $I = 1.5 \text{ mW/cm}^2$, and taking into account the magnification of the beam after it passes the cell, the intensity on the atoms must be $I = 10 \text{ mW/cm}^2$. Therefore, with the intensity $I = 0.9 \text{ mW/cm}^2$ specified earlier, we use about one tenth of the dynamic range of the CCD, and we are already almost saturating the transition. This is not the ideal situation, but it did not significantly affect the quality of the data.

3.7.3 Magnification and calibration

A schematic of the imaging system designed to produce a magnification of 2.5 is shown in fig. 3.14. The telescope consists of a pair of achromatic doublets of focal lengths 40 mm and 100 mm respectively, spaced by a distance equal to the sum of the two focal lengths. The probe beam, collimated by the first lens after the fibre, is again collimated after the telescope, and the rays are normally incident onto the chip of the CCD. In order to reduce the aberrations, the distance between the atomic cloud and the telescope, and between the telescope and the surface of the CCD is as shown in fig. 3.14. The polarization is made circular by a polarizing beam splitter cube followed by a quarter-wave plate before the cell. The polarization is made circular by a polarizing beam splitter cube followed by a quarter-wave plate before the cell.

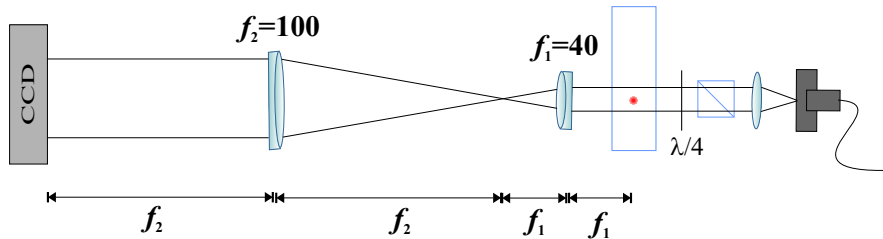


Figure 3.14: Schematic representation of the imaging system.

Focussing was achieved by finely adjusting the position of the first lens. The pixel size was calibrated by taking pictures of condensates for different time-of-flight, and fitting the free fall with a parabola (see fig. 3.15). The measured magnification factor was 2.59 ± 0.01 .

3.8 Computer control

The LabView program (by National Instruments) has been used to achieve precise control over several analogue devices and accurate time synchronization of digital and analogue devices on the experiment. The control program regulates the voltages sent to the VCOs which in turn control the frequency of the AOMs, the state of the mechanical shutters, and provide the control voltage to the power supply of the magnetic field and of the stabilization box. Once the science MOT is fully loaded, we use this program to start a sequence that triggers and regulates all the analogue and digital devices that are needed to load the magnetic trap, perform the evaporation to obtain the BEC, load the BEC into the optical traps, control the magnetic field required to produce the Feshbach resonance and during the ramps to create the molecules. Finally it also sets the imaging parameters and triggers the probe pulses for the acquisition of the images.

The computer reaches all the electronic devices controlled by the program via two 12 bit PCI cards (National Instruments: PCI-6713, and PCI-MIO-16E-4).

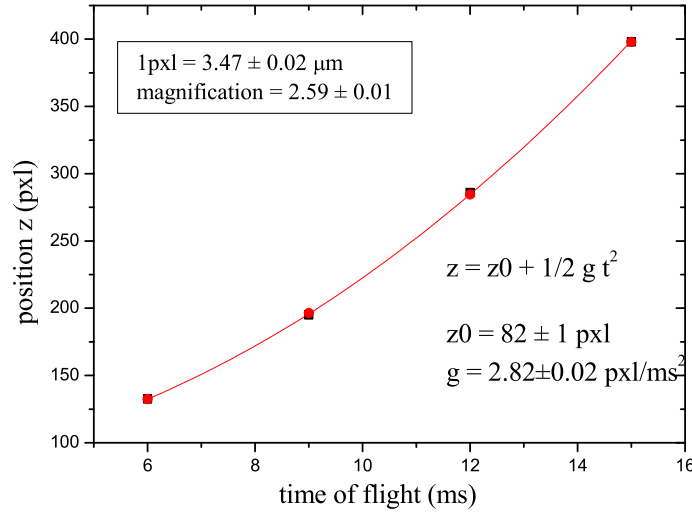


Figure 3.15: Calibration of the imaging system magnification with time of flight images.

The first has 8 analogue outputs, and 8 digital outputs, while the second has 2 analogue outputs and 16 analogue inputs, 5 digital outputs and 3 digital inputs. They both have 2 gated counters which are used for triggering the optical pumping pulses, and flashes of lattice light with TTL signals. This did not provide sufficient digital outputs, so an analogue to digital converter was designed, by the Central Electronics workshop of our physics department, to generate 8 digital outputs from one analogue output of the PCI-6713.

Obtaining BEC

This chapter describes the experimental protocol that we used to produce a BEC of ^{87}Rb atoms in the $|F = 1, m_F = -1\rangle$ state. Since it is a very standard procedure, I shall limit the content of this chapter to what is essential background for this thesis, and to the issues relevant to our experiments.

The first section deals with the loading of the magnetic trap, in particular mode matching, i.e. the preparation of the cloud in a way that it maintains the phase-space density upon loading into the magnetic trap. The second section describes the evaporation protocol and its optimization in order to maximize the number of atoms in the final condensate. Initial measurements performed with the condensates are briefly described in section 4.3.

4.1 Loading the TOP trap

As we have already discussed in the previous chapters, the densities and temperatures that can be achieved in a magneto-optical trap are not sufficient to reach the quantum degeneracy. To attain this, we need to employ evaporative cooling in a trap with no intrinsic cooling limits. This can be achieved by using a far-detuned optical trap or a magnetic one. We make use of a TOP trap, which is the magnetic trap described in chapter 2.

The maximum energy of the atoms that can be trapped in the magnetic trap is limited by the potential depth $\frac{\mu B_0}{4}$ derived in section 2.3.1. As we want to trap the biggest possible number of atoms in the initial trap, we will start with the maximum value of B_0 achievable with our setup, which is 44 G. This fixes the trap depth to about 370 μK (atoms in the $|F = 1, m_F = -1\rangle$ state have a magnetic moment that gives $\mu/h = 0.7 \text{ MHz/G}$). This depth is well above the temperature that can be achieved by the molasses cooling phase, thus the pre-cooled atoms do not escape if they are in the correct magnetic state.

4.1.1 Mode matching

The initial trap, besides requiring a depth higher than the energy of the atoms, must have a profile that matches that of the cloud. For a harmonic trap potential $V = \alpha r^2$, which has to host a cloud of mean energy $\langle E \rangle = \frac{3}{2}k_B T$, we need the size of the cloud in the i -direction to be $\sigma_i \sim \sqrt{k_B T / 2\alpha}$. Given the size and temperature of the molasses, this relationship fixes the curvature of the harmonic potential. For our experiment, we measured the temperature of the molasses to be about $30 \mu\text{K}$, and its radius 0.9 mm ; hence $\alpha \approx 2.5 \times 10^{-22} \text{ J/m}^2$. For the case of ^{87}Rb in a harmonic trap, this leads to a frequency in the radial direction of about 60 rad/s . Equation 2.12 in chapter 2 provides the relationship between the trap frequency and the magnetic fields generating the TOP potential. We have already stated the necessity of using the highest rotating bias field possible: $B_0 = 44 \text{ G}$; hence to obtain $\omega_r = 60 \text{ rad/s}$, requires a magnetic field gradient $b' \simeq 100 \text{ G/cm}$ (from eq. 2.12).

If the trap parameters are not those that give good matching, the kinetic energy and the potential energy are not balanced after loading, thus inducing a breathing mode (shape oscillations) to the cloud. Also oscillations of the center of mass of the cloud (*sloshing*), due to an offset between the position of the molasses and that of the center of the quadrupole field, cause initial losses if the cloud reaches the locus of $B = 0$. These oscillations were observed experimentally and we found that the breathing mode was negligible. The frequency of the sloshing oscillations of the cloud has been used to obtain a calibration of the effective trap frequency as a function of the magnetic fields (their amplitude was limited to about $270 \mu\text{m}$, which is one order of magnitude smaller than the initial radius of the circle of death).

To appreciate how much a mismatching affects the phase space density, we can look at the diagram in fig. 4.1, which shows the phase space density (in units of its initial value just before loading the trap) versus the trap frequency (in units of the value for an *ideal* matching). The function plotted is [85]:

$$\frac{\rho}{\rho_0} = \frac{8(\omega/\omega_0)^{3/2}}{(1 + \omega/\omega_0)^3}, \quad (4.1)$$

The diagram shows that having a trap of frequency higher than its ideal value is less harmful than under-matching. There is a range of about $\pm 20\%$ of the optimum trap frequency, where the phase space density is not reduced appreciably. We load the atoms into a trap whose frequencies are within this range.

To maximize the phase space density of the cloud that is transferred into the TOP trap, we used a three stage transfer protocol (implemented in the LabView program), to control the quantities relevant to the mode matching described above. In the first stage molasses cooling reduces the temperature of the atoms to about $30 \mu\text{K}$. In the the second stage we optically pump the atoms from the $F = 2$ level

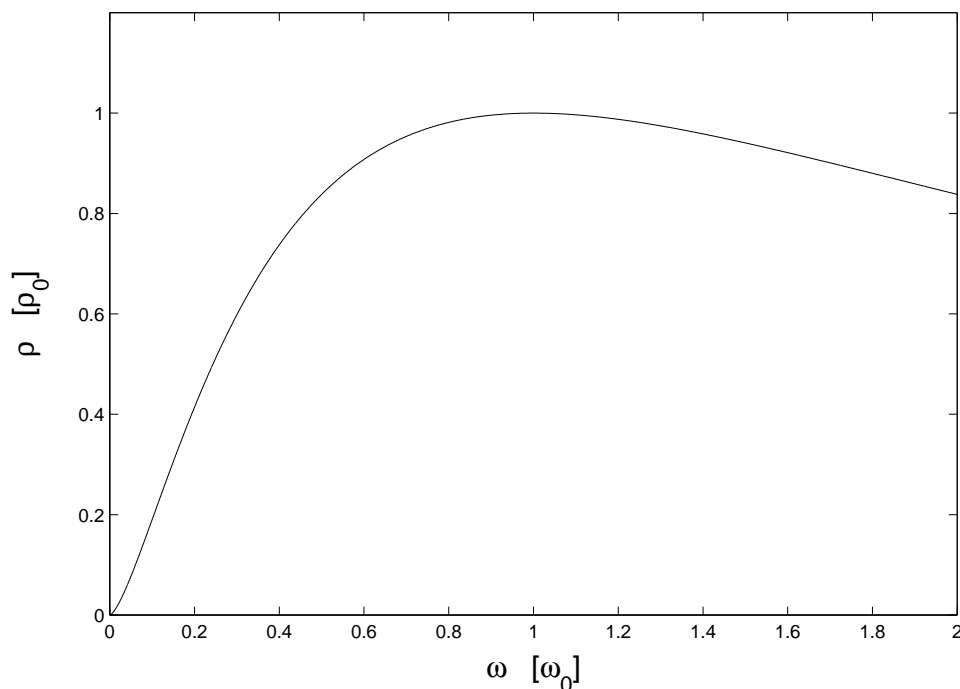


Figure 4.1: Phase space density (in units of its initial value just before loading the trap) versus the trap frequency (in units of the value for an *ideal* matching).

in the MOT, to the $|F = 1, m_F = -1\rangle$ state for magnetic trapping. The third stage is switching on the field to an appropriate initial trap strength.

The phase space density depends on the size of the cloud, as well as its temperature, therefore a compression of the MOT is sometimes performed just before the beginning of the optical molasses. In the compressed MOT, the gradient of the quadrupole field and frequency detuning δ of the laser are both increased. However, we did not perform any compression of the MOT before the molasses cooling, because it was not found to be useful in our experimental measurements. Although the phase space density is reduced by both the expansion of the cloud during the molasses phase and by the heating inferred by the optical pumping pulses, due to the molasses cooling and to the short duration of the optical pumping, it remained close to the top of the curve of fig. 4.1.

4.1.2 Optical molasses

To change from a MOT to optical molasses the magnetic field is ramped down to zero in 2 ms, whilst at the same time increasing the frequency detuning of the light. The cooling is thus provided by the sub-Doppler mechanisms described in section 2.1, giving a final temperature inversely proportional to δ , as given by eq. 2.3. The ramp is followed by further 4 ms of cooling at the final parameters.

In order to choose the final detuning for the molasses phase we plotted the phase space density of the initial TOP trap against different values of this parameter, and this plot is shown in fig. 4.2. We decided to use -35 MHz since greater red frequency detuning did not increase the phase space density significantly within the error bar, but gave fewer atoms. For the point at -50 MHz the number of atoms was about half that for all the previous points.

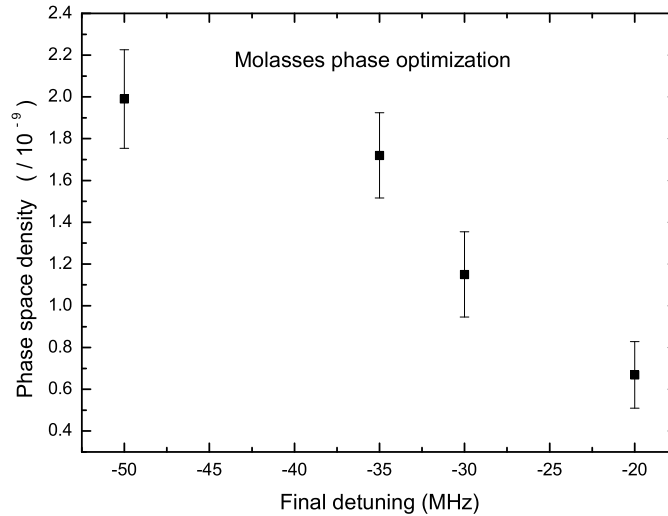


Figure 4.2: Phase space density of the cloud loaded into the TOP trap just after the molasses phase as a function of the final detuning for the molasses.

For these measurements we left atoms in the $F = 2$ level without performing any optical pumping, thus losing the fraction of atoms in magnetic sub-levels with $m_F \leq 0$. The number of atoms here is about 1 order of magnitude lower than the number of atoms actually transferred in the magnetic trap when we optically pump them into the $|F = 1, m_F = -1\rangle$ state. Also the phase space density measured here is one order of magnitude lower than that of the $|F = 1, m_F = -1\rangle$ atoms loaded in the initial trap.

The temperature reached with the molasses cooling was measured to be about $30 \mu\text{K}$ by a time of flight technique, i.e. looking at the size of the cloud as a function of time in free expansion.

4.1.3 Optical pumping

Different optical pumping strategies are possible to transfer the atoms into the state $|F = 1, m_F = -1\rangle$. We could have just switched off the repumping light at the end of the molasses stage, but this only puts $1/3$ of the atoms into the right m_F

state. Optical pumping with σ -polarized light tuned on the $|F = 1\rangle \rightarrow |F' = 1\rangle$ transition would give higher efficiency, but would have required an extra AOM on the optical bench to obtain the appropriate frequency. A simpler option is to use σ -polarized light tuned on the $|F = 2\rangle \rightarrow |F' = 2\rangle$ transition and switch the repumping light off. This does not need an extra AOM, and can also be used to obtain a BEC in the level $F = 2$. To this end we only needed to switch the polarization of the optical pumping beam from σ^- to σ^+ , and have some repumper light *ON* at the same time. We decided to use this second option for our optical pumping. The selectivity of the transfer is obtained thanks to the σ -polarized light and to the presence of a small (3.5 G) magnetic field that provides the atoms with a quantization axis.

To determine how many pulses to use (and which duty cycle) for an optimum transfer, we experimentally scanned one parameter at a time (number of pulses and duration), and recorded the number of atoms transferred in the magnetic trap. This process led to the choice of 15 pulses, each lasting 40 μ s, of light detuned by 5 MHz below (red) the centre of the $|F = 2\rangle \rightarrow |F' = 2\rangle$ transition. The magnetic field is provided by the TOP field, which rotates at 7 kHz, hence the pulses need to be synchronized in such a way that the direction of the magnetic field is parallel to the laser beam at the middle of the 40 μ s pulse. About 0.9 mW of laser light are sent to the atoms using the same optical fibre used for the imaging, therefore also this beam has a $1/e$ diameter of 6.5 mm, and a peak intensity of about 5.4 mW/cm².

The whole optical pumping process lasts about 2.1 ms (since each of the 15 pulses is synchronized with the rotation of the TOP field (7 kHz), which has a time period of 0.143 ms). There is a rise in temperature of the order of a few recoil energies, where ⁸⁷Rb has $T_r=360$ nK (since $\lambda=780$ nm), meaning an overall increase of about 1 μ K. This is negligible compared to the 30 μ K of the molasses.

Our optical pumping scheme transferred 70% of the atoms into the $|F = 1, m_F = -1\rangle$ state. That this transfer efficiency is entirely due to the optical pumping pulses can be seen from the following considerations. As our probe beam uses light resonant with the $|F = 2\rangle \rightarrow |F' = 3\rangle$ transition, we need to transfer the atoms back to $|F = 2\rangle$ before the imaging. This is done by sending repumping light on the atoms for nearly 1 ms just before the probe pulse is fired. The fact that no atoms are observed without this repumping stage before the imaging means that of the (30%) atoms not pumped in the state $|F = 1, m_F = -1\rangle$, none are left in the $|F = 2\rangle$; hence the remaining fraction is entirely pumped into the $|F = 1, m_F = 0, 1\rangle$, and then lost during the magnetic trapping phase. Moreover, if we do not perform optical pumping before loading the magnetic trap, then probing with or without repumping light does not change the number of atoms detected, which means that no atoms were in the $|F = 1\rangle$ state to start with.

4.1.4 Parameters of the initial trap

At the end of the optical pumping the atoms are ready to be trapped in the magnetic potential where their phase space density will be increased by means of evaporative cooling up to and beyond the threshold of condensation.

To load the magnetic trap all the laser light is blocked and the magnetic field is quickly turned on. The atoms are now in a magnetic trap whose strength is determined by the combination of a quadrupole field, of gradient $b' = 95$ G/cm along the radial direction, with a rotating bias field of magnitude $B_0 = 44$ G. These were chosen by looking at the temperature of the cloud loaded into the magnetic trap, and trying to minimize it. The harmonic potential generated by these values of b' and B_0 has a radial frequency $\omega_r \simeq 60$ rad/s that nearly matches the frequency for which the plot of fig. 4.1 has a maximum.

The lifetime of the atoms in the magnetic trap was measured to be about 85 s, and a plot of this measurement is shown in fig. 4.3. The initial ten seconds were left out of the fit because we are only interested in the losses due to collisions with the background atoms, which are determined by the vacuum level and therefore are always present, and not in the initial rapid loss.

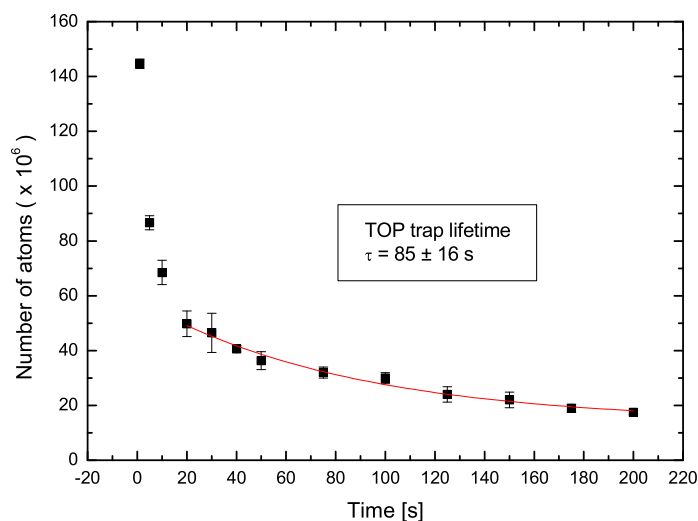


Figure 4.3: Measurement of the lifetime of the atoms in the loading TOP trap.

From the plot in fig. 4.3 we can see that in the initial trap we can load about 10^8 atoms. These have an initial phase space density of about 4×10^{-8} . The eight orders of magnitude needed to reach the threshold of condensation are gained with the evaporative cooling, in the way described in the next section.

4.2 Evaporative path to BEC

We use evaporative cooling to reduce further the temperature of the cloud down to the critical temperature T_c , whose expression was given in section 2.4. Since T_c depends on the number of atoms in the trap, the more atoms are removed from the trap during the evaporation, the lower the temperature needs to go in order to reach the degeneracy, so this process should be performed as efficiently as possible. During the evaporation each atom that leaves the cloud must take away much more energy than the mean energy. The speed of this process is regulated by the rate at which elastic collisions redistribute energy (which depends on the temperature and density of the cloud).

The three parameters: temperature, number density, and phase-space density, are connected between them by the relationship $\rho = CnT^{-3/2}$. The proportionality term C contains only fundamental constants and the mass m the atom, and for ^{87}Rb its value is $C = 6.5 \times 10^{-30} \text{ m}^3\text{K}^{3/2}$. For an effective evaporation we have to act on both n and T in order to increase ρ . Our starting point, for the atoms loaded into the TOP trap, is $n \simeq 6 \times 10^9 \text{ cm}^{-3}$ and $T \simeq 10^{-4}\text{K}$, yielding a phase space density $\rho \simeq 4 \times 10^{-8}$. The other important parameter of evaporative cooling, the elastic collision rate, is given, in terms of the density of the cloud, the cross section and the mean velocity of the atoms, by the relationship [2]

$$\Gamma_c = \sqrt{2} \cdot \bar{n} \bar{v} \sigma \quad (4.2)$$

where $\sqrt{2} \cdot \bar{v}$ is the relative mean velocity between two atoms (with $\bar{v} = \sqrt{\frac{8k_B T}{\pi m}}$), and $\sigma = 8\pi a^2$ is the cross section for elastic scattering (a being the scattering length). For a harmonic trap, moreover, the mean density is related to the trap frequency by the expression [86]:

$$\bar{n} = N \bar{\omega}^3 \cdot \left(\frac{m}{4\pi k_B T} \right)^{3/2}. \quad (4.3)$$

And combining these two equations we get:

$$\Gamma_c \propto \frac{\bar{\omega}^3}{T}. \quad (4.4)$$

The rate of elastic collisions in the initial trap (from eq. 4.2) is $\Gamma_c \simeq 1 \text{ s}^{-1}$. In section 2.5 we have seen that effective evaporation requires a ratio between elastic and inelastic collisions of about 300. This ratio can be estimated by the product of the elastic collision rate times the lifetime of the TOP trap, and in our case it is $\Gamma_c \tau \approx 80$ (for the initial trap). The first step of the evaporation must therefore be to increase this parameter. The lifetime of the trap is limited by the vacuum, hence the quantity on which we can really act during the evaporation is Γ_c .

4.2.1 Increasing the collision rate

To have a larger rate of elastic collisions in the trap we adiabatically compress the cloud (by increasing the magnetic field gradient). By definition this preserves the initial phase space density. This adiabatic compression in a harmonic trap increases the collision rate proportionally to the square of the frequency of the trap; ρ stays constant, so: $\rho \propto nT^{-3/2} \propto r^{-3}T^{-3/2} \propto r^{-6}\omega^{-3}$, where the last step is possible because the temperature in a harmonic trap is given by $T \propto \omega^2 r^2$. Therefore constant ρ implies $r \propto \omega^{-1/2}$, hence $T \propto \omega$, which combined with eq. 4.4 proves that $\Gamma_c \propto \omega^2$ as stated.

The condition for the compression to be adiabatic is: $\frac{d\omega}{dt} \ll \omega^2$ [2]. During the first 4 s of the evaporation we nearly double the collision rate by ramping the field gradient b' from 95 G/cm to 125 G/cm (b' indicates the gradient of B along the radial direction, which is half the value it has along the axial direction). At this early stage we still want to minimize the evaporation, as it would not increase the phase space density; therefore, in order to have the largest possible radius of the circle of death, we keep the TOP field B_0 at its maximum value of 44 G. This first adiabatic compression just increases the elastic collision rate, bringing the product $\Gamma_c \tau$ to about half the value needed for the runaway regime. This target will anyway quickly be reached during the next ramp, when the stiffness of the trap is increased by reducing the amplitude of the rotating bias field and further increasing the gradient.

4.2.2 Evaporation with the rotating potential

The evaporation proper is carried out by ramping down the rotating bias field. Experimentally we determine the speed of the ramp for which the gain in phase space density is highest compared to the loss in number of atoms. As we reduce the value of B_0 , the frequency of the trap goes up according to eq. 2.12; this further compresses the atoms, thus increasing the collision rate and speeding up the thermalization of the cloud, which allows faster ramps.

We found that an optimum slope for the phase space density against the number of atoms was reached when the ramp was split into two steps. During a first step the magnetic field gradient was slowly ramped up to its maximum value $b' = 175$ G/cm in 22 s, whilst at the same time the trap depth was reduced by decreasing the value of B_0 from 44 G to 9 G. The second step keeps the field gradient constant whilst further reducing the value of B_0 , in 8 s, from 9 to 3.5 G. Table 4.1 summarizes the achievements of the evaporation up to this stage. We can see that the collision rate has brought the system in the runaway regime already before the end of the 22 s ramp, and that, so far, the gain in phase space density has been of about 5 orders of magnitude, against a loss of about 2 orders of magnitude in the number of atoms. The trend $\rho \propto N^{-2.5}$ is comparable to what found in many similar experiments.

Time (s)	b' (G/cm)	B_0 (G)	N	Γ_c (s^{-1})	T (μ K)	n (cm^{-3})	ρ
4	125	44	$5 \cdot 10^7$	2	120	10^{10}	$2 \cdot 10^{-8}$
22	175	9	10^7	20	40	$2 \cdot 10^{11}$	$2 \cdot 10^{-5}$
8	175	3.5	$2 \cdot 10^6$	100	8	$2 \cdot 10^{12}$	10^{-3}

Table 4.1: Values of some parameters relevant to the evaporation, at the end of each stage.

The radius of the locus of $B = 0$ is about 0.5 mm at the end of the 22 s ramp, and at the end of the 8 s ramp is only 0.2 mm. A further reduction of B_0 led to large losses. From this point on, therefore, we complete the evaporation with the radio-frequency cutting, keeping the frequency and depth of the trap constant at their final values: $\omega_z/2\pi = 170$ Hz, and $U = 30$ μ K.

4.2.3 Radio-frequency evaporation

The starting point of the RF ramp can be calculated by considering the following: at any point on the circle of death the value of magnetic field varies between 0 and $2B_0$ during one cycle of the rotating field. At the centre of the trap the field is B_0 . The condition for magnetic resonance between two consecutive Zeeman sub-levels is $h\nu = g_F\mu_B|B|$ (where g_F is 1/2 in our case), therefore the variation of the magnetic field between $2B_0$ and B_0 corresponds to a frequency sweep from $\nu = \mu_B B_0/h = 4.9$ MHz ($B_0 = 3.5$ G) to a value $\nu = \mu_B B_0/2h = 2.45$ MHz; where the latter is resonant for atoms in the centre, i.e. at the bottom of the trap.

The RF-evaporation is performed in two steps. The first RF-sweep starts from about 5.2 MHz (just outside the circle of death), which is chosen to prevent ‘accidental’ evaporation before the start of the ramp (caused by any leakage of radio-frequency when the amplitude of the RF-amplifier is set to zero). Then we ramp it down to 3.9 MHz in 9 s, gaining one further order of magnitude in phase space density whilst halving the number of atoms. A plot of the phase space density against the number of atoms during the different phases of the evaporation process is shown in fig. 4.4. The final ramp takes 5 s to sweep down to the threshold of condensation, around 3.1 MHz, or below for a more pure condensate (below 2.9 MHz no thermal component can be discerned).

Fig. 4.5 shows the formation of the condensate during the late stages of the RF-evaporation. The three pictures were all taken after 14 ms of time of flight. The first picture shows a very cold thermal cloud ($N = 8 \times 10^5$, $T \simeq 500$ nK, $\rho=0.5$). In the second picture a condensed peak appears in the middle of the thermal cloud ($N = 5 \times 10^5$, $T \simeq 300$ nK, $\rho=2.8$), and the last one is a pure condensate (about 2×10^5 atoms) with no visible thermal component.

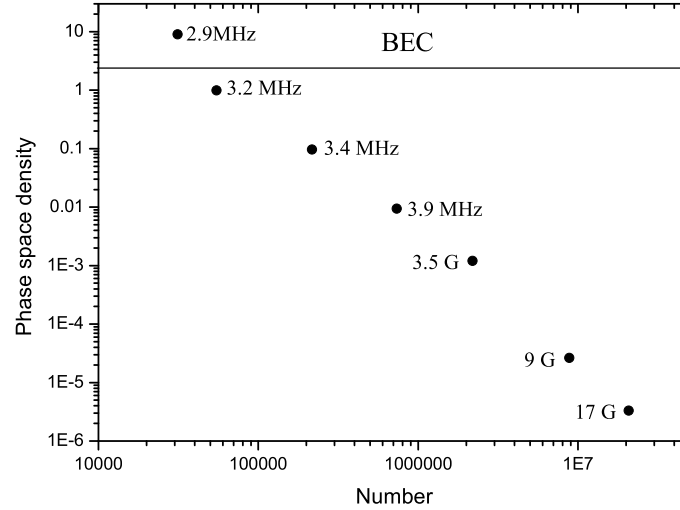


Figure 4.4: Plot of phase space density vs atom number during the evaporation.

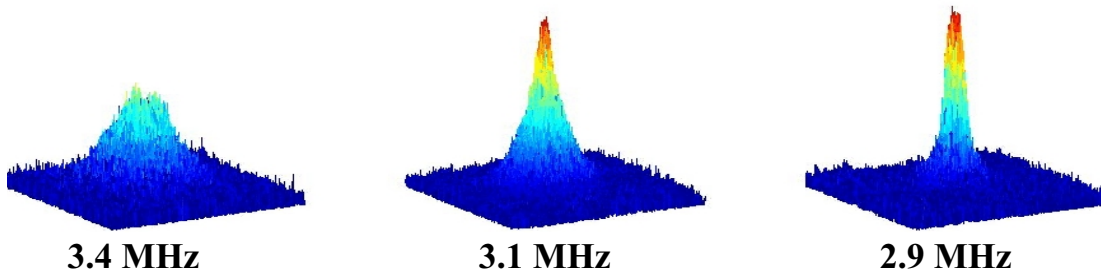


Figure 4.5: 3D plot in false colours of the BEC formation during the late stages of the RF-evaporation. The frequency underneath each picture indicates the final point of the RF-sweep.

4.3 Additional measurements with the BEC

This section records two measurements performed after obtaining BEC that provided us with a more accurate calibration of the TOP field. It is actually a double calibration, using two different methods. The first one is based on probing the cloud (using absorption imaging) in the presence of the rotating TOP field synchronized with the probe pulse; we keep the magnitude of the field constant while varying the detuning δ of the probe. The ‘number of atoms’ detected are plotted as a function of the detuning of the probe beam, see fig. 4.6 (this is the ‘number of atoms’ calculated assuming resonant absorption, which is used as a measure of

the absorption). The absorption has a maximum at the detuning δ_0 for which the Zeeman shift $\mu_B B$ makes the transition resonant. From the value of δ_0 we can work out the magnitude of the magnetic field through the relationship $B = \hbar\delta_0/\mu_B$. To obtain the value of the peak detuning we assume a Lorentzian line shape, and fitting our data with this function shows that the previous value, coming from a theoretical prediction based on the geometry of the coils, was wrong by a factor 1.72. For this measurement we used a very cold thermal cloud (with only partial RF-evaporation).

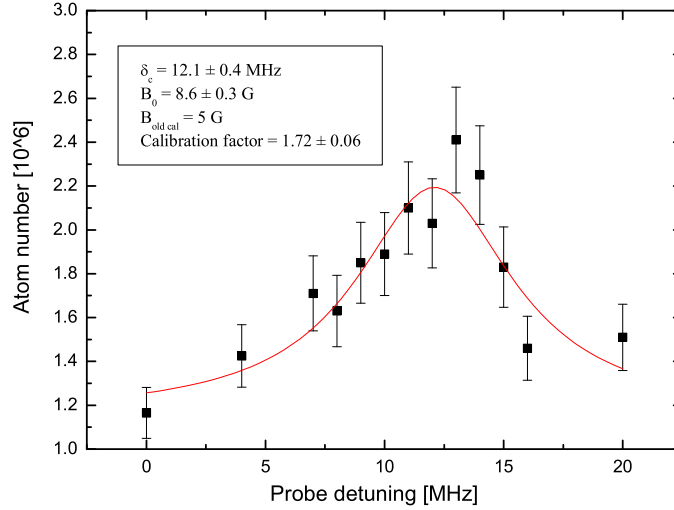


Figure 4.6: Calibration of the TOP field by measuring the Zeeman shift induced on the atomic levels.

The second calibration is based on the RF-cut in the final magnetic trap. As we have discussed above, the value of the radio frequency during the evaporation ranges between two values determined by the top and the bottom of the magnetic trap, and their energy depends on the value of B_0 alone. This provides a method to calibrate the magnetic field by looking at which frequency we start to evaporate. Fig. 4.7 shows a plot of the number of atoms against the final frequency of the RF-cut. As its final frequency starts to drop below the top of the trap the atoms start to be evaporated and a knee is observed in the plot. The horizontal lines indicate the average (with error) of the first 7 points on the right, and the diagonal line comes from a linear fit of the remaining points. The position of the knee is determined as the intersection of the two trends. Also this calibration suggests the same factor 1.72, therefore we decided to adopt it to re-calibrate the magnitude of the rotating field.

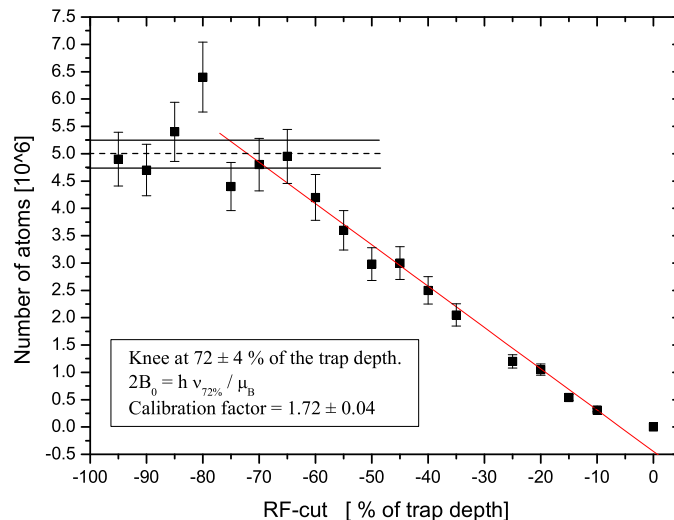


Figure 4.7: Calibration of the TOP field based on the condition for magnetic resonance during the RF-evaporation.

4.4 Summary

In this chapter I have presented the results of the experiments that led to the production of BEC of ^{87}Rb atoms in the $|F = 1, m_F = -1\rangle$ state by means of evaporative cooling in the TOP trap. The criteria adopted to choose the parameters for the transfer of the MOT into the magnetic trap, and subsequently those used to perform evaporative cooling have been discussed. With these parameters we are able to transfer into the magnetic trap up to 2×10^8 atoms in the desired atomic state, and after 48 s of evaporative cooling we can produce pure condensates with about 2×10^5 atoms.

As a preliminary measurement, partially evaporated thermal clouds were used to obtain a more accurate calibration of the rotating field in the TOP trap. This was done by using two independent methods, one relying on the Zeeman shift of the atomic energy levels, and the other based on the condition for magnetic resonance during the RF-evaporation.

1-D Optical lattice

After achieving BEC we set up a standing wave to trap the condensates in a one-dimensional optical lattice with the objective of observing the Feshbach resonances that occur in the $|F = 1, m_F = +1\rangle$ hyperfine state of ^{87}Rb [34]. This state, as we have already said in the previous chapters, cannot be trapped in a magnetic trap.

The interest in atom lattices and in their possible applications to quantum computation, led us to this choice. Later, specific requirements of the molecule production mechanisms, such as the density of atoms, and the aim to preserve coherence throughout the sample, led us to set up also a crossed-beam optical dipole trap, to which the next chapter is dedicated.

In this chapter I shall go through the setup of the standing wave, illustrating its construction and design features. The procedure used to align the standing wave onto the atoms is described in section 5.2. The last three sections are dedicated to the loading and characterization of the atoms in the lattice, such as lifetime, trap depth, and trap frequencies.

5.1 The standing wave

To set up our one-dimensional optical lattice we used a single vertical beam of laser light, focussed to a minimum waist of $60\ \mu\text{m}$, and retro-reflected to form a standing wave. The light source was a pair of semiconductor diode lasers SDL-5422 operating at 850 nm, set up in the standard master-slave configuration. The optics involved is shown in the schematic of fig. 5.1. Being far off-resonance from any atomic transition, we do not need to lock the laser frequency to any particular value. However, to form a standing wave, the laser frequency must be stable, therefore we used an external cavity master laser which operates single mode.

To monitor the laser mode and the injection of the slave we send the light from both lasers into an etalon cavity (Tec Optics, FSR=3GHz), with no need

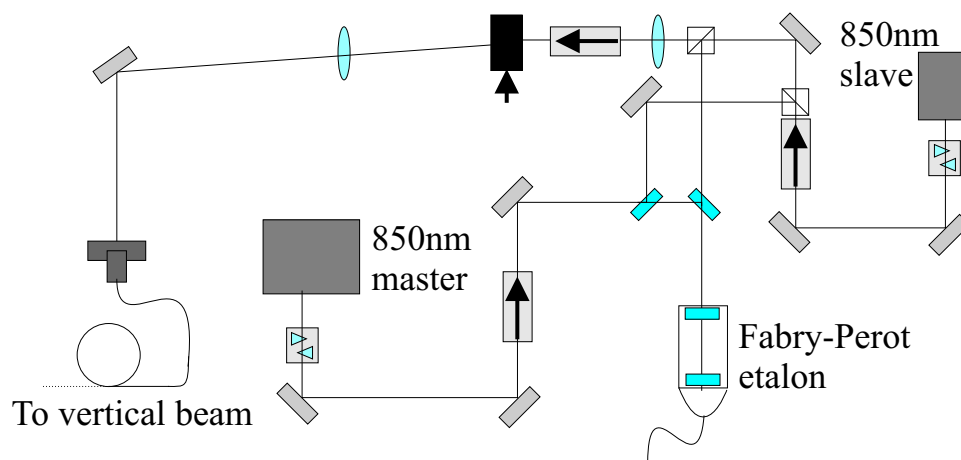


Figure 5.1: Schematic of the laser setup for the standing wave.

for saturated absorption spectroscopy. The slave laser follows the mode coming from the master over a frequency that is typically a few free-spectral ranges of the etalon. Some light from the two laser sources is deflected using beam splitters, so that the status of the light can be monitored in real time on an oscilloscope during the experiment.

In order to reduce further the feedback from the retro-reflected beam, the light from the slave laser is then passed through a second optical isolator. Subsequently, an AOM used in single pass acts as a fast switch for the lattice light. When the AOM is *on*, the first diffracted order is injected into a single-mode polarization-maintaining optical fibre. When it is *off* there is no diffracted order, hence there is no light coupled into the optical fibre. This fibre, like those transporting light to the MOTs, besides acting as a mode cleaner making the beam profile Gaussian, also decouples the alignment of the laser part of the table from the science cell area.

Of the initial power (60 mW) in front of the fibre, about one half is coupled through it and, due to losses in other components and reflections on the cell surfaces, only about 25 mW are available for the standing wave. In order to align the 850 nm light along the same path as the MOT2 beams, we use two dichroic mirrors (**DM**), see fig. 5.2. These have been fabricated here at the department of physics, with a specially designed multi-layer coating that reflects linearly-polarized light at 850 nm, and transmits 780 nm light. In tests these mirrors reflected 98% of the 850 nm light when it was horizontally polarized, and over 99% when it was vertically polarized.

With a total power of 25 mW available for the standing wave, we can calculate from eq. 2.32 that a beam focussed to a waist of $50 \mu\text{m}$, and retro-reflected, will give a lattice depth of $80 E_r$. We decided to aim for such a deep trap so that the apparatus was suitable also for number squeezing experiments [87]. To obtain

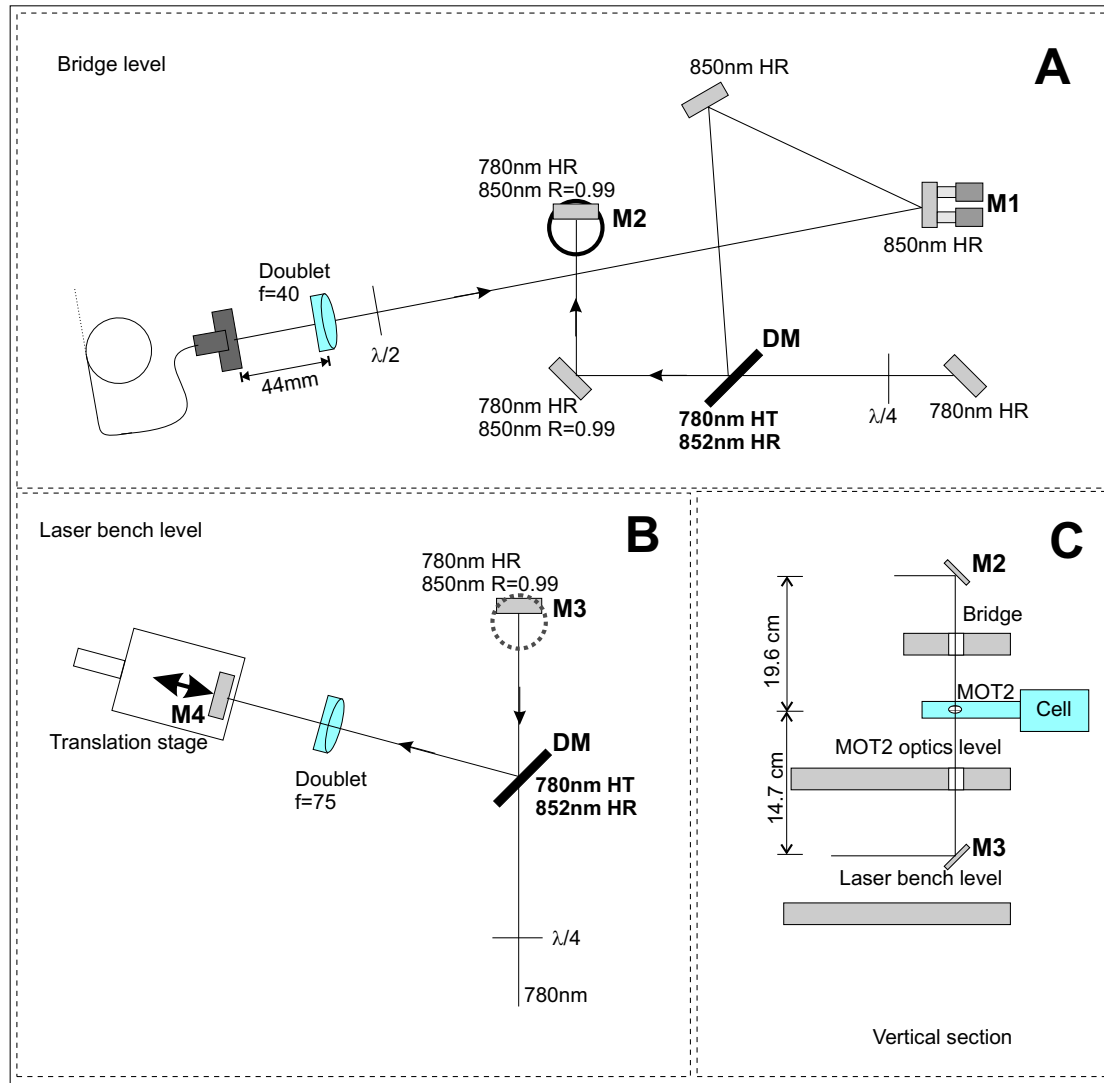


Figure 5.2: Schematic representation of the optics to set up the lattice. (A) The output of the lattice beam fibre is on the upper bridge of the optical table. The position of the doublet lens determines the waist size and its longitudinal position. Mirror M1 is the one used to optimize the alignment onto the atoms. (B) On the lower level of the optical table, mirror M4 is on a translation stage to optimize the spatial overlap of the retro-beam with the down-going beam. (C) Vertical section of the optical table around the cell.

such a beam waist, a doublet lens of focal length $f = 40$ mm was placed 44 mm after the output of the optical fibre. The core of the optical fibre has a radius of $4 \mu\text{m}$ and so the waist of the laser beam exiting the fibre is comparable. Measuring the size of this beam at two different points after the lens, and using the laws for the propagation of Gaussian beams, we deduced that a waist of about $55 \pm 5 \mu\text{m}$

($1/e^2$ half width) would form 78 cm after the lens. This was consistent with the beam having an initial waist given by the core of the optical fibre, and the waist position was consistent with what we could judge by ‘eye’ observing the beam with an infrared sensor card.

The beam’s path length was then designed so that the focus of the beam fell at the trap position within a Rayleigh range $2Z_R$ ($Z_R=10.4$ mm for our measured waist and a wavelength of 850 nm). After crossing the cell, the beam is deflected by the second dichroic mirror, which deflects the 850 nm light out of the path of the 780 nm light. The deflected beam is focussed by a second doublet lens of focal length $f=75$ mm, to a waist of $12 \mu\text{m}$ onto the retro-reflecting mirror **M4**, positioned to form the standing wave (this mirror will be referred to as the *retro mirror* throughout this thesis).

Obtaining a reliable measurement of the effective size of the standing wave at the position of the atoms is not easy, but this is a critical parameter for our experiments, and so it is worthwhile to briefly note some details here. The waist of the standing wave depends on how well we can superimpose the waist of the retro-reflected beam to the waist of the down-going beam. An independent, indirect measurement of the size of the latter comes from the measured values of the oscillation frequencies in the crossed-beam dipole trap, reported in chapter 6. In chapter 2, we have derived the expression for these frequencies in eq. 2.49, and we can see from there that ω_y depends only on w_1 , which is the waist of the down-going beam, and on the trap depth. Working out the waist size from the value measured for the trap frequency $\omega_y/2\pi = 67$ Hz, we obtain $63 \pm 6 \mu\text{m}$. This overlaps, within the experimental error, with the value deduced by Gaussian beam propagation; but the large one suggests a shallower potential. The measured potential depth of the lattice was in the range of 11-15 E_r (see section 5.4), which corresponds to an even bigger beam size ($120 \mu\text{m}$), but this is completely out of the error of these two measurements, suggesting that the lower lattice depth measured is due to other factors such as a larger effective waist of the standing wave caused by the retro-reflected beam having the waist in a slightly different z position, and/or propagating in a slightly tilted direction.

5.2 Alignment procedure

A first rough alignment of the lattice beam onto the MOT was performed by coupling light at 780 nm into the optical fibre used for the standing wave. The procedure was based on loading the second MOT and then, when it was fully loaded, flipping a mirror to send 780 nm light through the optical fibre. The flipping mirror was placed in the path of light going to the pyramid trap; therefore during this stage the second MOT was not being loaded anymore by the atomic beam from the pyramid MOT. However, the nearly 80 s lifetime of the second MOT was long enough to steer the direction of the down-going beam (acting on mirror

M1) until it destroyed the MOT. Attenuating further and further the 780 nm beam, we were able to see it acting as a push beam at the centre of the MOT (being this much bigger than the waist of the lattice beam). The procedure was repeated with a more compressed MOT ($b' = 20$ G/cm) so that, since the 780 nm light forms a waist very close in size and position to that formed by the 850 nm light, we could set the direction of the beam accurately enough to observe some atoms being trapped into the standing wave at 850 nm. Small adjustments on the retro mirror enhanced this preliminary trapping effect. The angle and position of the retro mirror were optimized on the power of the light retro-reflected through the fibre. For the first alignment, iteration of this procedure was sometimes required.

At this point the alignment could be optimized, in the direction that can be seen by the CCD camera, by taking pictures of the BEC in trap, and of the atoms held in the lattice. The lattice beam was moved until the atoms were held by the lattice in the same position where the BEC was formed. In the orthogonal direction (along the probe beam) this could not be done, so we optimized the alignment in that direction by looking at the diffraction peaks of the BEC. This process will be accounted for in a quantitative way in section 5.4, where the measurement of the standing-wave potential depth is described.

5.3 Loading of the atoms into the lattice and lifetime

To reduce heating and losses, we loaded the atoms into the optical lattice adiabatically by slowly turning on the standing wave before switching off the quadrupole magnetic field. The rotating bias field stays on to keep the atoms polarized (in zero field they would spin flip between the different Zeeman sub-levels). As usual, *adiabatic* means that the time taken to ramp the intensity of the lattice beam from zero to 100% must be large compared to $1/\nu_L$, the inverse of the lattice frequency. The radial frequency of the standing wave is about 70 Hz, hence the ramping time must be longer than 14 ms. We raise the intensity of the light linearly in a 50 ms ramp. Subsequently we ramp the gradient of the magnetic field b' from 175 G/cm down to zero in 100 ms ($B_0 = 3.5$ G all the time).

When the alignment of the trap was improved, we observed a number of different features of the periodic potential that helped us to check various aspects of the system. A first experiment, when the lattice depth was about $1.5 E_r$, was to generate a pulsed atom laser like the one observed at Yale in 1998 [16]. The experiment was performed by ramping the lattice power in 3 ms and keeping it *on* for a variable time, counted from the subsequent switching off of the quadrupole field, before taking a picture. As it is shown in fig. 5.3, pulses of atoms are emitted from the BEC with periodicity $\tau = \frac{2\pi}{\omega_B} = 1.1$ ms, where $\omega_B = mg\lambda/2\hbar$ is the Bloch frequency at which the atoms oscillate in the lowest band, and are emitted at the

turning point of each oscillation.

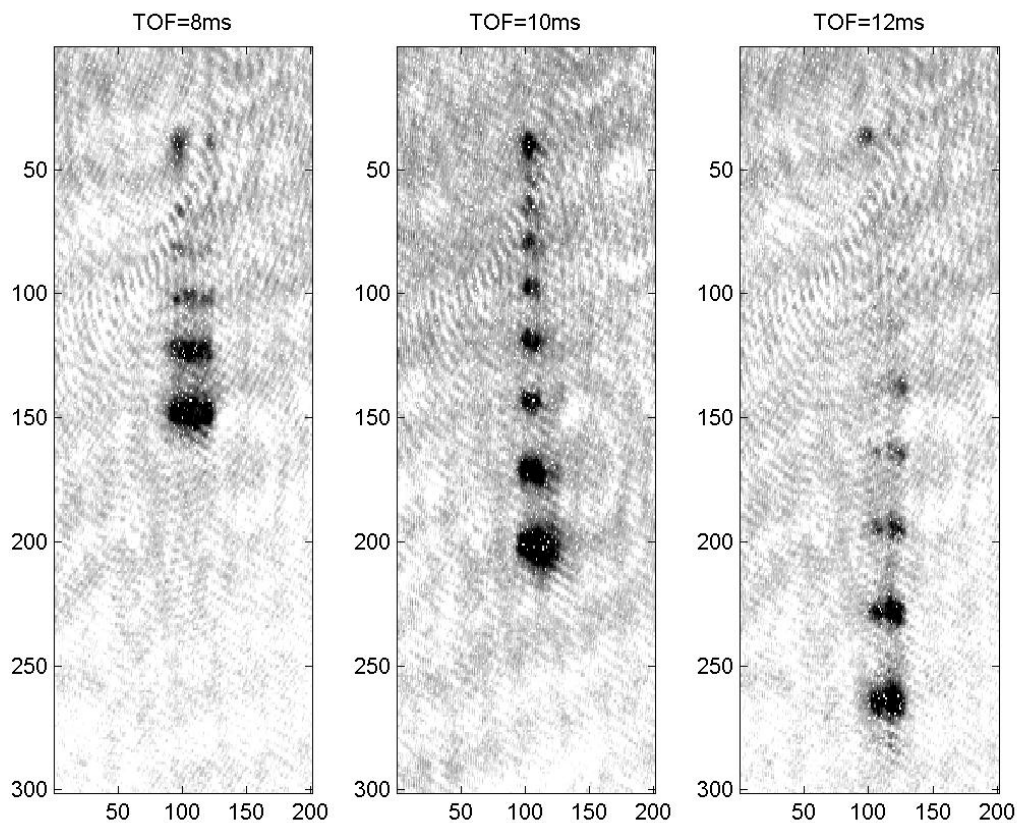


Figure 5.3: Condensed atoms emitted by a lattice $1.5 E_r$ deep, for three different holding times. The axes are labeled in camera pixels, $1 \text{ pixel} \simeq 3.5 \mu\text{m}$

Further improvement of the alignment made the trap depth sufficient to hold the atoms in the standing wave alone, at which point we could measure the lifetime of the lattice. We made this measurement for two different lattice depths. The first time the lattice was about $8.5 E_r$ deep, and the measured time for the number to reduce of one half was $\tau_{1/2} = 1.7 \pm 0.2 \text{ s}$. The second time the depth was $11.7 E_r$ and the measured decay time was $\tau_{1/2} = 0.9 \pm 0.1 \text{ s}$. The data for these measurements are shown in fig. 5.4.

For atoms loaded into the ground state of an optical trap from a BEC, 3-body collisions play a relevant role in the loss mechanism. It has been observed also elsewhere, in agreement with our measurements, that longer lifetimes are achieved as the trap depth is reduced so that the atoms heated via collisions can escape the trap [88]. The dependence of the lifetime on the trap depth is not obvious, but it can qualitatively be understood in terms of density of the trapped

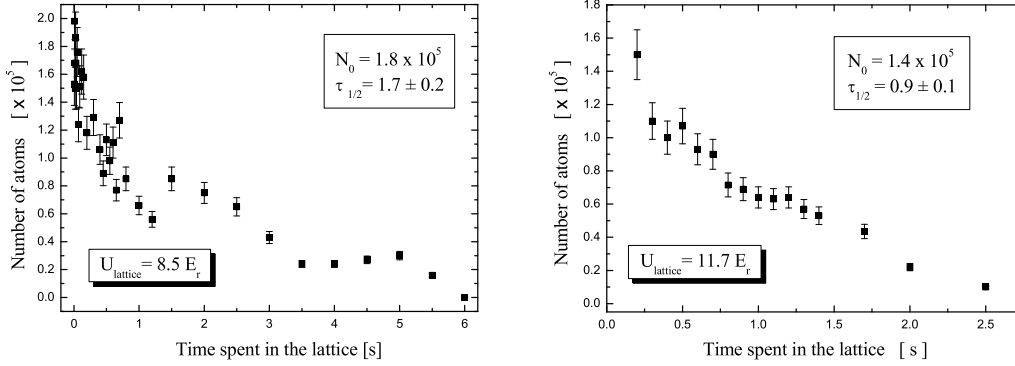


Figure 5.4: Decay of the number of atoms trapped in the lattice for two different trap depths.

atoms. As the trap depth increases, the density (and therefore the rate of 3-body collisions) increases as well. If three body collisions are the main source of loss, then we have $\tau \propto n^{-2}$, where n is the density of atoms in each lattice site, and the proportionality constant is the inverse of the three-body collision rate coefficient. From the discussion in appendix C we can deduce that in each lattice site $n \propto a_{\text{h.o.z}}^{-1} R_{2D}^{-2} \propto U$, thus $\tau \propto U^{-2}$. This is in good agreement with the two measurements given above, i.e. $(1.7/0.9) \times (8.5/11.7)^2 \simeq 1$. Therefore we should expect for the lifetime of the atoms in a trap with depth $U = 14 E_r$, as that used for most of the experiments described in chapters 7 and 8, lifetimes of the order of 0.66 s. This time is still long compared to the duration of any experiment performed with the atoms in the lattice. If we use this value of the lifetime for a $14 E_r$ deep lattice, and the value of the mean square density $\langle n^2 \rangle = 2 \times 10^{-29} \text{ cm}^{-6}$ as obtained from equation C.7 of appendix C, the three-body collision rate comes out to be $0.8 \times 10^{-29} \text{ cm}^6/\text{s}$, in good agreement with the value measured in chapter 7.

5.4 Measurement of the depth of the lattice

In order to compare the atom loss measured during the molecule formation experiments, we need to know the depth of the potential in which the atoms were held. This section explains how we experimentally measured the depth of the optical lattice by looking at the diffraction of the BEC released from a standing-wave potential. The theory involved in this technique has been described in section 2.6.1.

The size of a BEC is small compared to the Rayleigh range of the focussed laser beam forming the trap, therefore we assume equal depth for all the wells populated. Moreover, the axial extent of the BEC is $6 \mu\text{m}$, so we populate about 30 lattice sites, which are half wavelength apart from each other (i.e. 425 nm), and

we can treat the majority of the wells as being in an infinite array. Therefore our system meets the requirements needed to use the theory in chapter 2, where we considered the case of sudden loading of the trap and subsequent evolution of the populated trap levels for a time τ . During this time the amplitude of the plane wave components oscillates as shown in fig. 2.5.

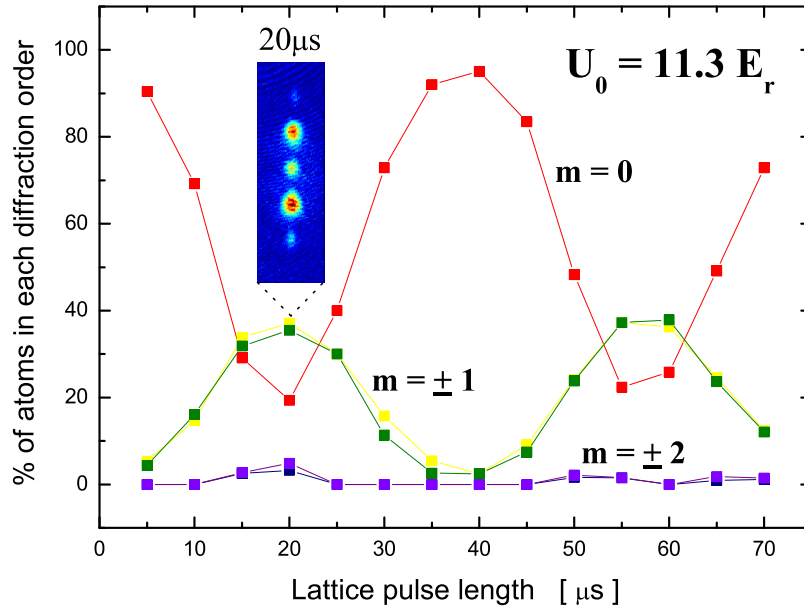


Figure 5.5: Percentage of the population of the different diffraction orders as a function of the time spent in the lattice.

Experimentally, we complete the evaporation in the magnetic trap, turn off suddenly the magnetic potential, and immediately fire a pulse of lattice light of duration τ . The different diffracted orders are allowed to separate thanks to the acquired different momenta $2m\hbar k$, where $m = 0, \pm 1, \pm 2, \dots$ indicates the order of the diffracted cloud. After a time $t = 15$ ms of expansion in free flight, the orders are separated enough to measure the number of atoms in each of them. The zeroth order will have fallen as much as the BEC would have, and the other orders are separated by $\Delta z = \frac{2\hbar}{M\lambda}t \simeq 160 \mu\text{m}$. In fig. 5.5 the percentage of atoms measured in each order is plotted against the duration of the lattice pulse. The position of the minima and maxima of each order and their relative amplitude give the depth of the lattice by comparison with the theoretical plot. To this end, the plot reported in chapter 2 (fig. 2.5) was made for a trap depth $U_0 = 11.3 E_r$, which best reproduce the experimental trend.

5.5 Measurement of the radial trap frequencies

To the purpose of estimating the eccentricity of the profile of the lattice beam, we measured the frequency of radial oscillations of the atoms in the trap. To do so we parametrically excited the trapped atoms by modulating the amplitude of the frequency driving the AOM before the optical fibre. This results in modulation of the beam intensity (in our case 25% of its maximum value). The average trap depth during this measurement was about $8 E_T$, and the experiment was performed on a very cold thermal cloud of about 2×10^5 atoms.

Plotting the size of the cloud in the radial direction against the modulation frequency we found two peaks, indeed showing that the beam profile was elliptical. The plot of the measurement is reported in fig. 5.6, where the two peaks are localized around 92 and 100 Hz, indicating two trap frequencies: $\omega_{r1} = 2\pi \times 46$ Hz, and $\omega_{r2} = 2\pi \times 50$ Hz. The relationship between frequency and trap waist in the lattice is given in equation 2.39, and it shows a dependence $\omega_r \propto 1/w_0^2$, thus also the waist difference between the two axes is only of 4%, making the beam profile elliptical with eccentricity $e = 0.28$. This could be due to a slight misalignment between down-going beam and retro beam.

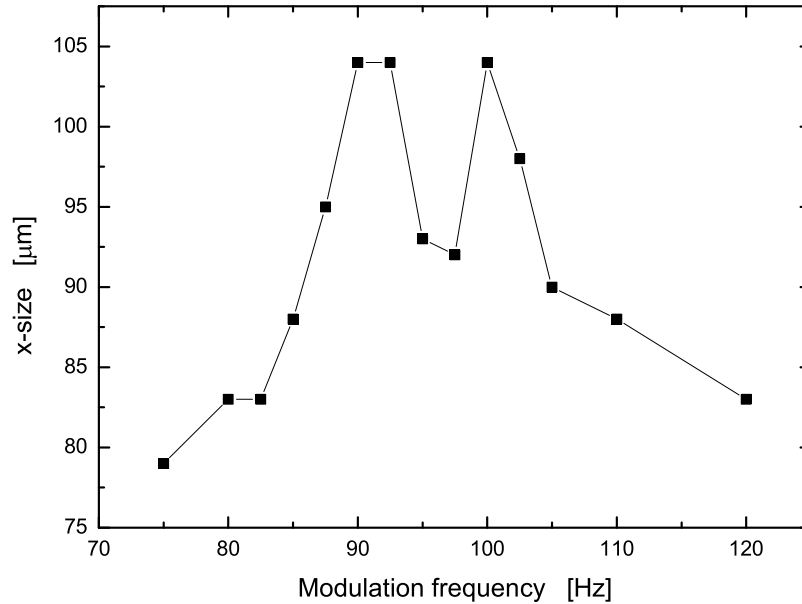


Figure 5.6: Parametric excitation of a cloud of cold atoms trapped in the standing wave. As a measurement of the disturbance generated on the atoms, the radial size of the cloud, along the direction visible by the camera, is plotted against the modulation frequency. The images are taken after 15 ms of time of flight.

This measurement of the radial frequencies can be used to obtain the effective average waist of the standing wave from the eq. 2.39, yielding $w_0 = 71 \mu\text{m}$. This is slightly larger than the waist obtained for the down-going beam alone from the parametric oscillations in the crossed-beam dipole trap, which suggests that the down-going beam and the retro-reflected beam cross at a slight angle.

5.6 Summary

In this chapter I have described how the 1D lattice has been set up and aligned onto the atoms. The choice of the loading parameters has been discussed, and we have seen how the trap depth affects the lifetime of the lattice. The lifetime was measured to be 1 s, and the maximum trap depth 10-15 E_r (depending on the alignment), for a total power of the lattice beam of 25 mW. Finally, the radial trap frequencies were also measured by parametric excitation of the trapped atoms.

Crossed-beam dipole trap

The second type of optical trap set up for this experiment is a *crossed-beam* dipole trap. The reason for doing this has been discussed at the beginning of section 2.6.2, where also the theory relevant to some features of this trap has been introduced. This second trap gave us the chance of trapping the condensates in a single trapping region (unlike the standing wave). This chapter reports on the work done to set up (section 6.1), align (section 6.2), and characterize our crossed-beam dipole trap (sections 6.3 and 6.4).

6.1 The horizontal beam

This section describes the main features of the trap, in which two 850 nm laser beams are focussed to a waist of about $60\ \mu\text{m}$, and cross each other orthogonally near the centre of the magnetic trap. Of these two beams, one propagates along the vertical direction; it is the one used for the lattice, but without retro-reflection. The other beam propagates on the horizontal plane, and its setup is described here.

The main components of the laser system, shown in figure 6.1, are: a free-running laser diode, an AOM (which acts as a switch), and a polarization maintaining optical fibre. When the AOM is on, the first diffracted order goes into the optical fibre, which brings it from the laser area of the table to the science cell area (onto the MOT2 optics level; see fig. 5.2). No frequency stabilization is needed for this beam, because the light is so far detuned that the optical dipole force does not require a linewidth narrower than a free-running laser can provide.

Up to 65 mW of laser power is transmitted through the fibre and focussed to a waist of about $60\ \mu\text{m}$. Due to space constraints around the cell, it was only possible to make this beam cross the cell along the same axis as the imaging system (which is described in section 3.7). We did not want to alter the existing imaging system, and therefore we had to produce that waist using the telescope already

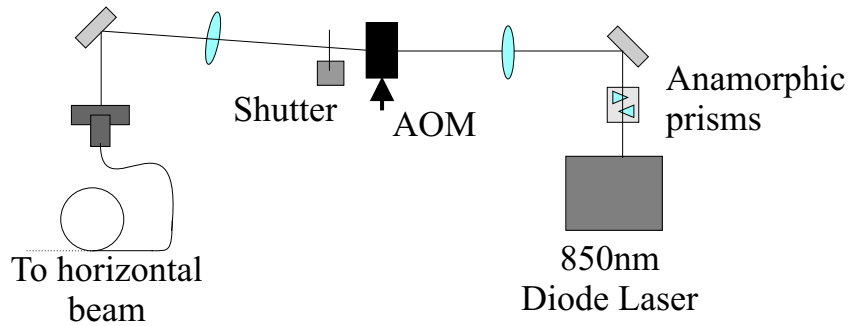


Figure 6.1: Schematic of the laser setup for the horizontal beam.

present on that path, and used to magnify the images of the atoms. This is a 1:2.5 magnifying telescope made of two doublets with focal lengths $f=40$ mm and 100 mm, and placed at a distance that equals the sum of the two focal lengths. In order to have a $50 \mu\text{m}$ waist at the trap position, we need to have a $125 \mu\text{m}$ ($= 50 \times 2.5$) waist at one focal length distance from the $f=100$ mm lens of the imaging magnifying telescope (see fig. 6.2). To achieve this, a doublet lens L1 of focal length $f=30$ mm was placed 30 mm after the fibre to have a collimated beam, and then a telescope (consisting of lenses L2 and L3, separated by 250 mm) was inserted into the path to give the $125 \mu\text{m}$ waist, at the required distance from the imaging telescope.

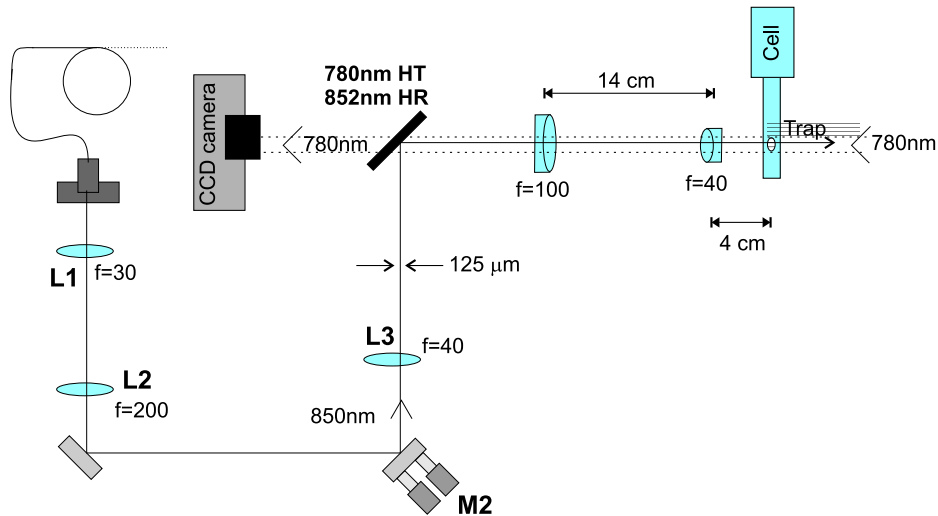


Figure 6.2: Schematic of the set up used to align the horizontal beam onto the atoms.

The beam at 850 nm is deflected along the imaging direction using a dichroic mirror similar to that used to superimpose the standing wave with the MOT light, as described in section 5.1. The waist of the horizontal beam was found to be larger than the $50 \mu\text{m}$ in the original design. It is approximately $60 \mu\text{m}$, as we

shall derive from the measurements reported in section 6.4.

6.2 Alignment procedure

As we can see from fig. 6.2, there are three lenses before the imaging telescope: L1 is a doublet with $f=30$ mm, L2 has $f=200$ mm, and L3 has $f=40$ mm. Mirror M2, just before lens L3, is close to a focus of the beam, and therefore it is used for the fine tuning of the transverse position of the waist on the atoms.

As with the standing wave, the alignment is performed in two main steps, repeated cyclically if needed. First we use weak light at 780 nm to align the horizontal beam in such a way that it hits the centre of a compressed MOT (with $b' = 30$ G/cm), as already described in section 5.2. Then, using 850 nm light, we act on the differential screws mounted behind mirror M2 for the fine tuning, while measuring the shape, size, and temperature of the atoms loaded into the crossed dipole trap. A sufficiently well aligned trap gives round cold clouds after release and time of flight.

To double check that the waist of the beam was, also longitudinally, at the position of the magnetic trap, we let a very weak beam (indeed, just the leakage light from the AOM switched off) through the whole path, and then sent it onto the chip of a CCD camera. The camera had been previously focussed on a very tightly compressed MOT, so that, by moving lens L2, the focus of the horizontal beam was positioned on the magnetic trap within the diameter of a compressed MOT, i.e. a few mm. The pixel resolution of the monitor used for this process suggested a beam size of about $40 \mu\text{m}$. Even if the waist were this small, the beam Rayleigh range would still be about 5 mm, which ensures that if the beam is focussed within a Rayleigh range, the beam size on the atoms would be at most about $60 \mu\text{m}$.

6.3 Loading parameters and lifetime of the trap

For a good mode-matching we want the oscillation frequencies of the optical trap to be similar to those of the final magnetic trap, i.e. : $\omega_r = 2\pi \times 60$ rad/s, and $\omega_z = 2\pi \times 170$ rad/s. Equations 2.48-2.50 express the frequencies of the optical trap as a function of the trap depth and the beams waist; for a beam of waist $60 \mu\text{m}$, the frequency is ~ 100 Hz, when the power is 50 mW. We managed to obtain a diffraction efficiency of about 80% from the AOM, and by careful alignment we managed to couple 70% of the power into the optical fibre. Thus, from 125 mW before the AOM, with the laser running at the maximum recommended current, we get typically 66 mW out of the optical fibre. Reflections on the cell surface cause a further 5% loss of power, to leave just above 60 mW at the atoms (therefore

we must push the laser very close to its maximum current, which can shorten its lifetime).

The adiabatic loading of the atoms into the trap was performed on the same timescale used for the lattice. For trapping frequencies of the order of 100 Hz we need ramping times slower than 10 ms. We find that ramping up the intensity of the light in 100 ms generated good dipole traps. The final powers were between 90% and 100% of the maximum power for the horizontal beam, and between 50% and 100% for the vertical beam. The rotating bias field of the TOP trap was maintained at $B_0 = 3.5$ G whilst the gradient was ramped down to zero in 50 ms.

For the maximum light intensity in both beams we measured the lifetime of the atoms in the trap. The procedure was again to make a BEC, then turn on the optical trap in 100 ms, ramp down the magnetic field, and hold the atoms in the optical potential for a variable time t . Fitting the decay of the number of atoms as a function of the time t spent in the trap, as shown in fig. 6.3, yields a lifetime $\tau = 2.9$ s. A longer lifetime than those reported for the lattice is obtained because, as explained in section 5.3, the crossed-beam potential has a lower depth than the standing wave.

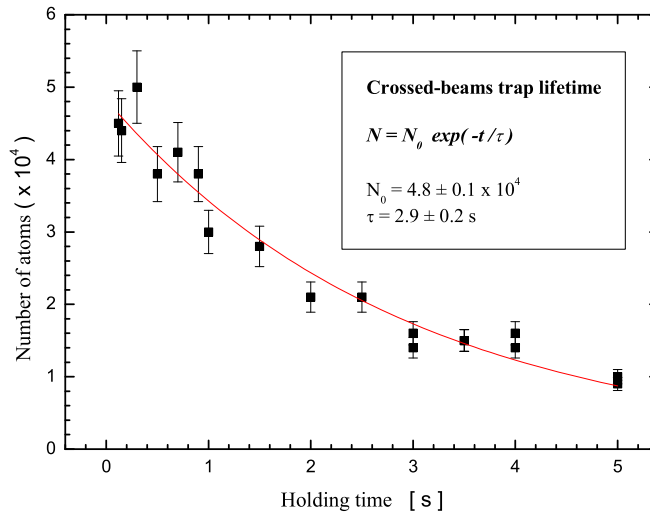


Figure 6.3: Lifetime of the atoms in crossed-beam dipole trap.

6.4 Measurement of the trap frequencies

This section describes the measurement of the trap oscillation frequencies carried out to obtain information on the waists of the two beams. It was also used in

deriving the depth of the trap; in doing this it is important to take into account the effect of gravity on the shape of the optical potential created by the crossed-beam, as described at the end of the section.

The trap oscillations frequencies were measured using parametric excitation of the cloud made by modulating the intensity of the beams (again this is achieved by modulating the AOM frequency, which, as an effect, modulates the injection into the fibre). Plotting the phase space density as a function of the modulation frequency, we observed three values for which the excitation was obviously affecting the phase space density of the cloud. One of these plots is reported in fig. 6.4, which represents the excitation of the frequency along the horizontal beam by modulating the intensity of the vertical beam.

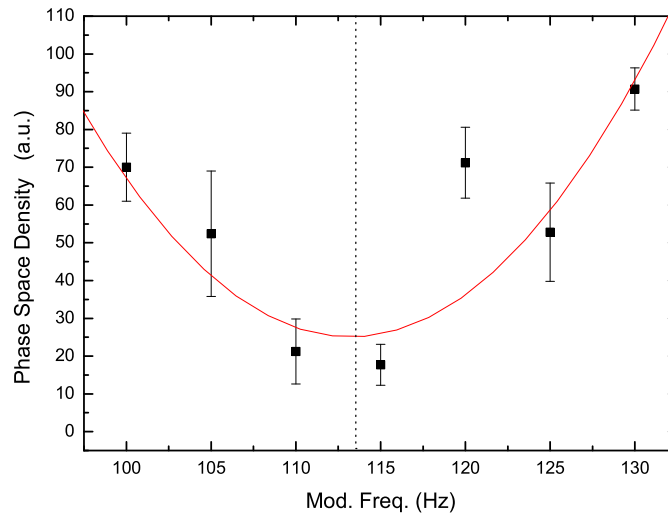


Figure 6.4: Parametric excitation of the oscillation frequencies of the atoms in the crossed-beam dipole trap.

As we are only interested in estimating the position of the centre, we used a parabolic fit, which localizes the position of the minimum around 113.5 Hz, yielding a trap frequency $\omega_y/2\pi = 57 \pm 5$ Hz. Similar measurements were performed in the other directions. Only two thirds of the power available to the vertical beam was used, while the horizontal beam was at 90% of its maximum intensity. The extrapolated frequencies, at full power, for all the three directions are: $(\omega_x, \omega_y, \omega_z) = 2\pi \times (116 \pm 10, 67 \pm 6, 82 \pm 7)$ rad/s. These are not in the exact relationship derived in eq. 2.48, but they fall within the error bar. We also see that these frequencies are not very different from the frequency of the final TOP trap.

Using equations 2.49 and 2.50, with U_{0i} given by eq. 2.47, we can derive the waist of the two beams. Putting these equations together, we obtain a dependence

$\omega \propto 1/w^2$. At full power of the two beams on the atoms ($P_{\text{vertical}} = 25$ mW, and $P_{\text{horizontal}} = 60$ mW), we obtain $w_{\text{vertical}} = 63 \pm 6$ μm , and $w_{\text{horizontal}} = 72 \pm 3$ μm ; this is not accurate for the horizontal beam because the effect of gravity must be taken into account, as shown in section 6.4.1.

At the end of section 2.6.2, we showed that the trap depth can be calculated as the $\min(U_{01}, U_{02})$, where 1 and 2 indicate the vertical and the horizontal beam respectively. The two values, calculated according to eq. 2.35, at full power, and entering the waists given above into the formulae, are $U_{01} = 12.4 E_r$ and $U_{02} = 24 E_r$. It would then seem that the overall trap depth is limited to $12.4 E_r$ by the vertical beam. But this is not what is observed. We are able to trap atoms in the crossed-beam trap when the intensity of the vertical beam is only a fraction of its maximum value ($\geq 50\%$), while the horizontal beam needs at least 90% of its maximum intensity. This implies that the dipole trapping from the horizontal beam is only 10% stronger than it is required to hold the atoms against gravity; therefore, from the same considerations as in the previous chapter for the depth of the atom laser, we can estimate its depth to be $1.6 E_r$. This does not agree with $U_{02} = 24 E_r$ stated above; to understand this discrepancy we have to see how the potential U_{02} is effected by the presence of gravity, so that its expression is no longer the one given in eq. 2.35.

6.4.1 The effect of gravity

To take into account the effect of gravity on the trap depth of the focussed horizontal beam, we can write the overall potential as:

$$U(z) = -U_0 \exp\left(-\frac{2z^2}{w^2}\right) - mgz \quad (6.1)$$

where U_0 is given by eq. 2.35. Taking first derivative of this expression with respect to z , we obtain the turning points a of the potential as the solution of the equation:

$$\frac{4U_0}{w^2} a e^{-2\frac{a^2}{w^2}} = mg. \quad (6.2)$$

Numerical solutions to this equation can be used to plot an harmonic approximation to the bottom of the real potential given by eq. 6.1. For the case of our horizontal beam, this potential and its harmonic approximation are plotted in fig. 6.5.

To obtain the trap parameters we require that the trap depth, given by the potential difference between the minimum and the maximum of the solid line, is $1.6 E_r$. Then we also require that the frequency of the harmonic approximation, given by the dashed parabola, is within the measured range: $\omega_z = 2\pi \times (82 \pm 7)$ rad/s. The laser power is also fixed to 63 mW. For all these parameters fixed, the plot of fig. 6.5 is obtained for a waist $w \simeq 58$ μm . The frequency of the trap

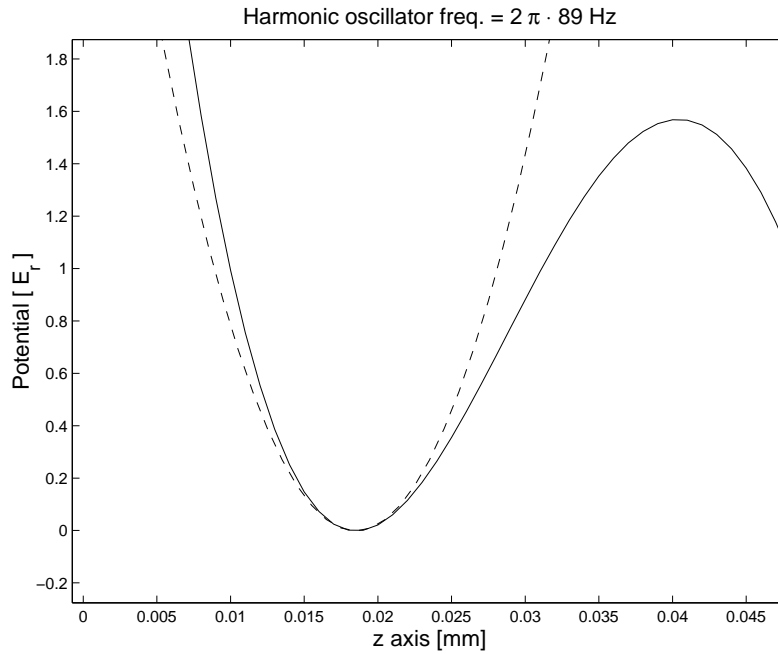


Figure 6.5: Plot of the potential of the horizontal beam as a function of z . The dashed line represents the harmonic approximation to the bottom of the potential.

is determined by the curvature of the dashed parabola: $\omega_z = 2\pi \times 89$ rad/s, which is just within the measured range. Besides, the centre of the trap is shifted down along z , indicating a gravitational sag of about $20 \mu\text{m}$. It is worth noticing that 89 Hz is the value of ω_z which fulfills the relationship of eq. 2.48, when ω_x and ω_y have the measured values given earlier.

In fig. 6.6 the potential of eq. 6.1 is plotted again, but on a much more expanded scale, in order to show the full profile. For comparison, this time the dashed line reproduces the same potential in absence of gravity. We can see from this plot that the effect of the term mgz on the potential is to reduce its depth U_0 by tilting the Gaussian profile of the beam intensity. Therefore, in order to account for the measured trap frequency, and for the apparent trap depth, the beam waist at the position where the atoms are trapped must be about $w \simeq 58 \mu\text{m}$. This is very close to the value already indicated by the considerations of section 6.2.

6.5 Summary

This chapter has described how the crossed-beam optical dipole trap used in this experiment has been set up and aligned onto the atoms. We have also discussed the loading parameters and how a lifetime for the trap, of about 3 s, has been measured. The measurement of the trap frequencies has been presented, and it

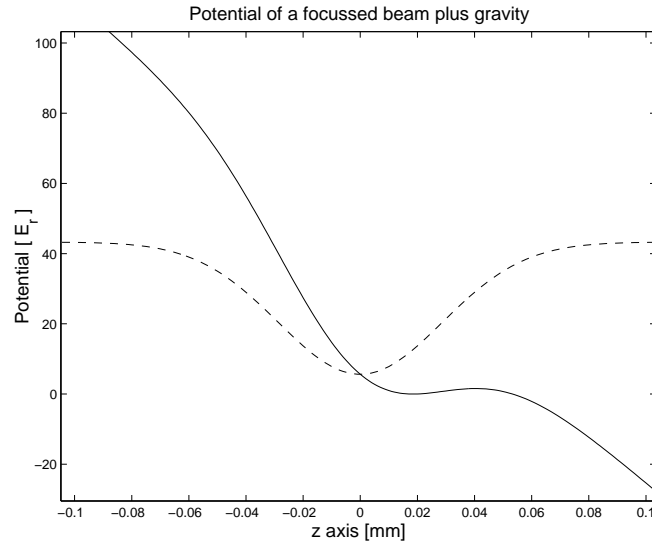


Figure 6.6: Extended plot of the potential of the horizontal beam as a function of z . The dashed line represents the optical potential without gravity.

has led to a discussion on the effect of gravity on the depth of the potential. This discussion has shown that the trap depth is dramatically reduced by gravity.

Observing a Feshbach resonance

This chapter describes the experimental work performed to localize and characterize the Feshbach resonance that occurs around 1007 G in the state $|F = 1, m_F = 1\rangle$ of ^{87}Rb . I would like to stress, yet again, that this state cannot be trapped in the magnetic trap, therefore these experiments are performed keeping the atoms in the optical traps described in chapters 5 and 6.

In order to look for the resonance, the first step is the transfer of the atoms from the state $|F = 1, m_F = -1\rangle$, where they are when we make the condensate, to the state $|F = 1, m_F = 1\rangle$. This transfer is achieved with an RF sweep at low field, and is described in section 7.1. Then, section 7.2 will deal with the observation of the Feshbach resonance. Lastly, section 7.3 will report on the measured increase in the 3-body loss rate when approaching the resonance.

7.1 RF transfer

After loading the atoms in one of the two optical traps, and before performing the actual transfer of atomic state, we must switch the direction of the current flow in one of the two magnetic coils to generate a homogeneous field rather than a quadrupole field, as described in section 3.4.5 of chapter 3. The switching of the connections to the coils is carried out while the current is zero, and then it is raised again, this time to generate a weak uniform field of 10 G. The reason for doing the transfer at low field is that the Zeeman effect is linear, and the splitting between the levels $m_F = -1$ and $m_F = 0$, and the levels $m_F = 0$ and $m_F = 1$ is the same. To estimate the efficiency of the transfer we put the atoms back in the magnetic trap (after the RF sweep); the magnetic field gradient has different effects on the three different m -states, so that these appear as distinct clouds in the t.o.f. images.

At a field of 10 G the Zeeman splitting between the sub-levels of the $F = 1$ level in ^{87}Rb , in frequency units, is given by $\frac{\mu B}{h} = \frac{\mu_B B}{2h} \simeq 7$ MHz. Therefore, in such a magnetic field, atoms initially in the state $m_F = -1$ will undergo transitions into the other magnetic levels when in the presence of RF at 7 MHz.

In order to obtain a complete transfer from the initial state to the final desired state we use an adiabatic RF sweep. This allows us to follow the avoided crossing of the levels as we sweep down the frequency through the point where the RF-coupling is maximum (7 MHz), as illustrated in fig. 7.1. To determine how slow the ramp must be to be adiabatic, we use the relationship $\tau = 2\Delta\nu/\Omega_R^2$ [89], where $\Delta\nu$ is the frequency range of the sweep, and Ω_R is the Rabi frequency (proportional to the amplitude of the RF).

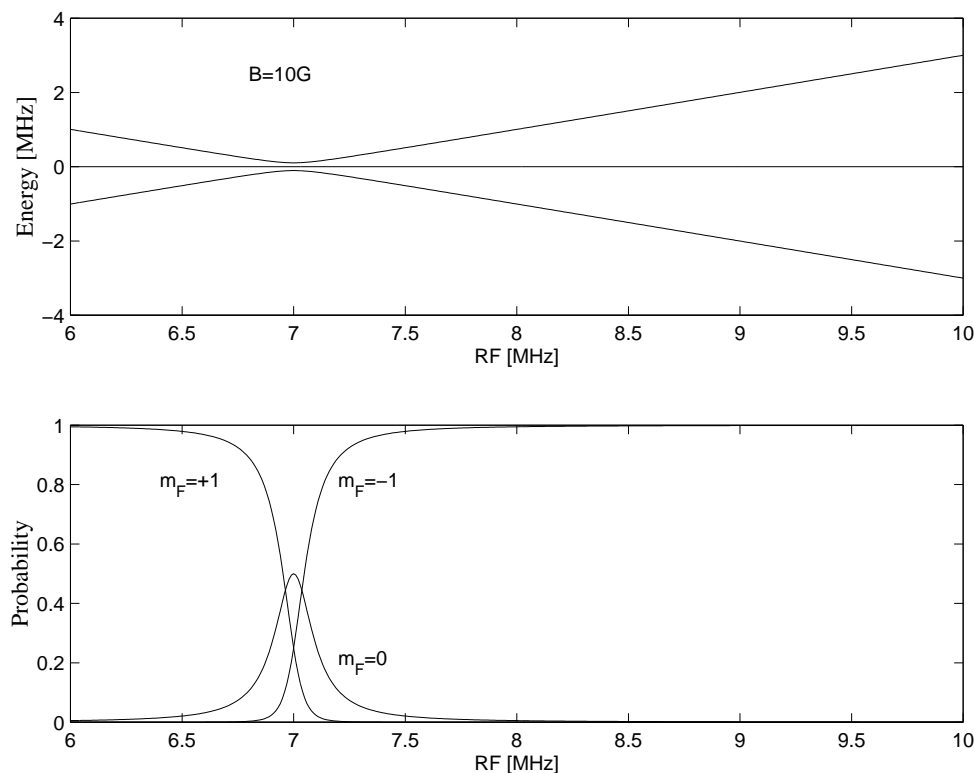


Figure 7.1: (Above) Zeeman energy levels in the presence of RF at 7 MHz (the zero is the energy of $m_F = 0$). (Below) The evolution of the population during the downward frequency scan, when starting with all the atoms in the level with $m_F = -1$

The strength of the RF field was estimated for the geometry of the coils and the maximum driving current; this very rough calculation suggested that τ must be longer than 0.4 ms. What we do in practice is to set the sweep time to be 20 ms and then reduce the intensity of the RF signal to the lowest possible that still allows a transfer efficiency into the level $m_F = 1$ of nearly 100%. The advantage of using a low power is that it makes the coupling region of the lower plot in fig. 7.1 narrower,

thus the end of the ramp is in a region where the interaction is practically absent.

After the transfer, the magnetic field was increased from 10 G towards the position of the resonance at 1007 G. Although at the end of the ramp the amplitude of the RF is turned to zero, we ramp the frequency from higher values to lower values, so that the system is insensitive to an accidental overlap of the end of the transfer stage with the beginning of the magnetic field ramp.

The timings of the complete transfer sequence are as follows: after switching to the Helmholtz configuration we ramp up the field to 10 G in 10 ms, wait for 1 ms, and then apply the RF signal, ramping its frequency from 10 MHz down to 6 MHz in 20 ms. The asymmetry of the frequency range with respect to the 7 MHz is an extra safety feature to make sure that all the population initially in the $m_F = -1$ is transferred. At the end of this process the fraction of atoms remaining in other states is not measurable, and we see that more than 99% of the atoms are transferred into the level $m_F = 1$ where the Feshbach resonance at 1007 G occurs.

We use a Stanford Research System frequency generator (DS-345) to generate the RF sweep, which is applied through a 10 turn coil of 2 cm internal diameter placed about 6 cm away from the atoms. To increase the RF amplitude, the frequency generator is attached to a home-made RF-amplifier, built using a Motorola 40 dB amplifier accepting maximum input 0 dBm. We found optimum transfer efficiency when using the RF amplifier with an input power of -3 dBm, i.e. about 37 dBm of output.

7.2 Localizing the resonance

Once the atoms are all in the desired state, we need to raise the magnetic field to the value where the resonance had been predicted and observe the atom loss. In practice we have to localize the resonance position within our own calibration of the magnetic field.

The experimental procedure is schematically illustrated in fig. 7.2. The cloud is subjected to a homogenous magnetic field, B_f , for a fixed time and the reduction of the number of atoms by collisions was recorded. The enhanced scattering length, as the field gets closer to the resonance, causes greater losses. During the entire procedure, which lasts 200 ms, the atoms are trapped in the standing wave. The magnetic field is ramped up linearly in 50 ms from the initial value of 10 G (used for the transfer) to a few Gauss above or below the resonance, so that the ramp speed of 20 G/ms makes the cloud insensitive to the other narrow resonances found at lower fields [34]. Then the field is ramped in 2 ms to the final value B_f close to the expected position of the resonance. The magnetic field magnitude is then kept at the final value B_f for 100 ms, before ramping it down to zero, again in 50 ms. The optical trap at this point is turned off, and after 15 ms of time of flight the atoms are imaged using the usual technique.

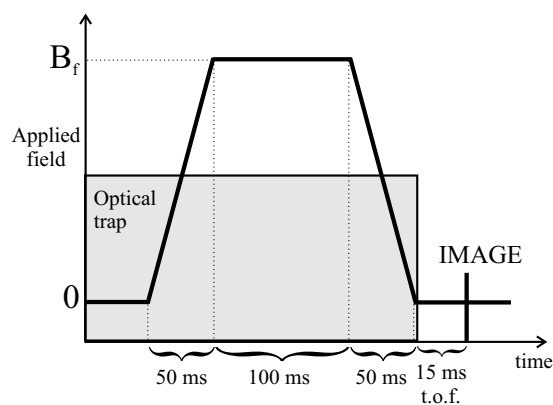


Figure 7.2: Time scheme of the procedure used to localize the Feshbach resonance.

The procedure described above is then used to localize the resonance by looking at the minimum of the plot of the number of atoms as a function of the final magnetic field of the ramp. Such a plot is shown in fig. 7.3.

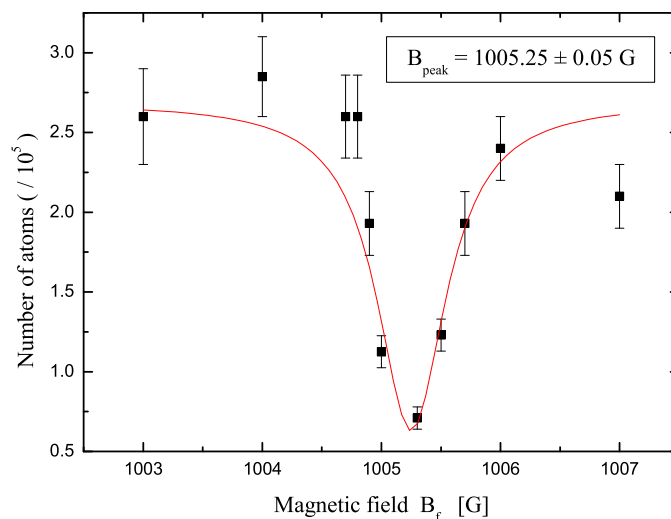


Figure 7.3: Number of atoms left in the trap after being exposed to a homogeneous magnetic field of magnitude B_f for 100 ms. The solid line is a Lorentzian fit used only to determine the position of the peak of the loss curve.

The asymmetry of the number of atoms probed below and above the resonance is due to the 2 ms ramp crossing the resonance to reach the field above. A Lorentzian fit of these data gives an estimate for the position of the centre of the loss curve as 1005.25 G. But, as explained in section 3.4.5, at around 1000 G our calibration of the magnetic field was accurate to about 3 G, therefore this must be

the resonance that was predicted to occur at 1007.4 G. A similar loss curve centred at 1007.34 G was obtained in the work presented in [34] where the observation of this resonance was first reported. A few months later the same group reported a complete characterization of this resonance [64] by obtaining a plot of the scattering length as a function of the magnetic field. The width ΔB was found to be 0.2 G, and the value for the centre of the resonance B_0 was found to be 1007.4 G, in good agreement with the theoretical predictions [34].

7.3 Measurement of the 3-body loss rate

To take into account the effect of the enhanced scattering length on the trapped atoms at the resonance position when looking for the formation of molecules, we have to understand what sort of losses are induced on the cloud as we sweep through the resonance. To this end, two types of measurement have been performed.

The first of these two studies provides us with a measurement of the dependence of the 3-body loss rate on the increased scattering length for magnetic fields close to the resonance. The second study measures the atom loss as a function of the magnetic field ramp speed when swept upwards across the resonance. This is described in the next chapter together with the loss curve due to a downward ramp where the molecules should be formed.

The rate equation for the 3-body losses (see eq. 2.52) can be integrated over the time $\Delta t = 0.1$ s during which the atoms are held at the field B_f (assuming that the trap volume stays constant whilst the number decreases), to find that K_3 is related to the losses observed by:

$$K_3^c = \frac{\left[\left(\frac{N_0}{N_f} \right)^2 - 1 \right]}{2 \langle n_0^2 \rangle \Delta t} \quad (7.1)$$

The initial mean square density in the trap is $\langle n_0^2 \rangle$, and N_0 and N_f are the number of atoms at the beginning and end of the time interval Δt . The experiment was performed with condensed atoms, therefore the rate constant obtained is K_3^c , which is the rate of 3-body collisions in the BEC (six times smaller than K_3 for a thermal cloud). The presence of this factor 1/6 had already been experimentally shown in [65]. It arises from the third order correlation function for ideal bosons. This can be understood in terms of an analogy with the intensity fluctuations present in a beam of photons, where the same physics accounts for the short-time photon bunching in a thermal light beam demonstrated by the Hanbury-Brown-Twiss experiment. In a thermal cloud of bosonic atoms, it is 3! times more likely that three atoms will be found together than in a BEC of the same mean density.

To determine the initial number N_0 we performed the process described above to obtain the loss dip (from where we get the values for N_f), but without the

pausing for 100 ms at the B_f , and without quite reaching the resonance position; in this way any losses that do not occur in the 100 ms wait period are excluded from consideration. The other parameter that we need is the initial mean square density ($\langle n_0^2 \rangle$) in the trap, which is obtained for the atoms loaded in the lattice as explained in appendix C.

Applying eq. 7.1 to the data plotted in fig. 7.3, along with $N_0 = 3.2 \times 10^5$ and $\langle n_0^2 \rangle = 2 \times 10^{29} \text{ cm}^{-6}$, we obtain the values of K_3^c for different magnitude of the magnetic field. These are plotted in fig. 7.4.

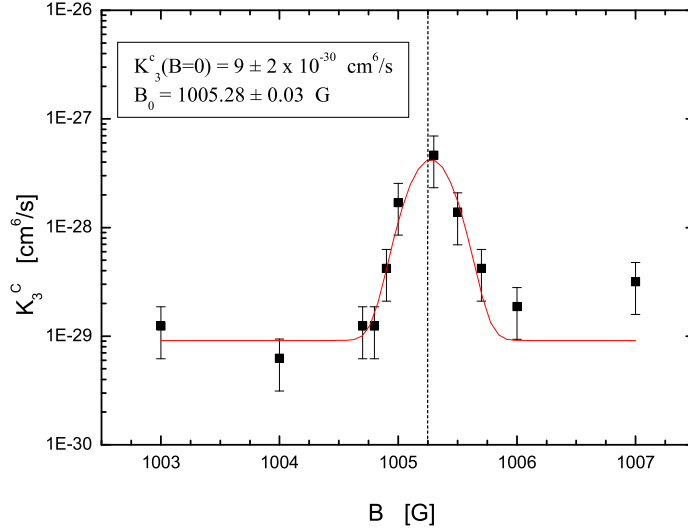


Figure 7.4: The dependence of the 3-body collision rate K_3^c on the magnitude of the magnetic field in a ^{87}Rb BEC.

The value for K_3^c away from the resonance is obtained using a Gaussian fit with a floating background (this has the sole purpose of determining the position of the centre and the asymptotic value of the wings). From the fit we obtain $K_3^c = 9 \pm 2 \cdot 10^{-30} \text{ cm}^6/\text{s}$ far away from the resonance, which increases by nearly 2 orders of magnitude as we get to the resonance centre. The position of the centre is also determined from the fit, and its value $B_0 = 1005.28 \pm 0.03 \text{ G}$ obviously matches the one determined from the atom loss curve of fig. 7.3. An estimate of the value of K_3 is $6K_3^c$. This gives $5 \times 10^{-29} \text{ cm}^6/\text{s}$ away from the resonance and a peak value of $5 \times 10^{-27} \text{ cm}^6/\text{s}$. The error bars in fig. 7.4 only account for the statistic uncertainty of the measurements. The experiment was performed in an optical lattice (not in the crossed-beam trap), and the mean square density of $\langle n_0^2 \rangle = 2 \times 10^{29} \text{ cm}^{-6}$ given above is an average of the mean square densities across the 30 wells populated.

In fig. 7.5 the three-body loss rate obtained for ^{87}Rb ($K_3 = 6K_3^c$) is compared

with a theoretical curve that comes from a 3-body calculation (provided by T. Köhler, Oxford). In fig. 7.5 an offset was added to the magnetic field in order to have the resonance at 1007.4 G and allow a direct comparison with the theory.

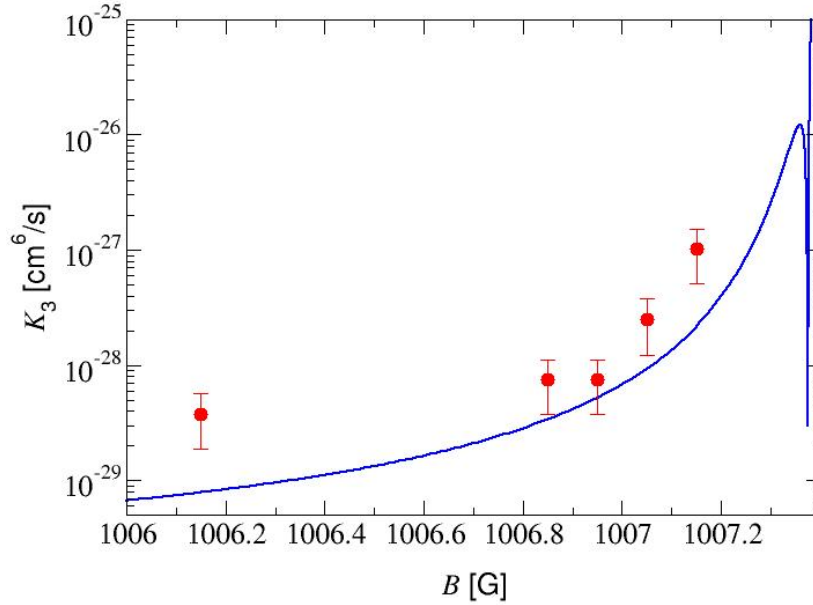


Figure 7.5: Comparison between the experimental values and the theoretical plot of the dependence of the 3-body collision rate K_3 on the magnitude of the magnetic field in ^{87}Rb .

Theory and experiment show a good agreement relative to previous comparisons found in the literature, as one can see, for example, in [90, 91]. The first of these two papers compares experimental and theoretical three-body recombination constants in a system without resonance enhancement, whilst the second is about fermions, and reports on p-wave resonance enhanced three-body recombination. Although these results are not directly comparable to ours, they give an idea to what extent three-body recombination processes can be predicted. Going back to our plot, we can see that the agreement improves going towards the resonance; this is due to the fact that the 3-body collisions play a more significant role in the losses as we get closer to the resonance. More details on the theoretical approach to the calculation can be found in [92, 93].

7.4 Summary

This chapter has described how atoms in an optical trap are transferred from the atomic state $|F = 1, m_F = -1\rangle$, in which they are in the TOP trap, into the state $|F = 1, m_F = 1\rangle$ where a number of Feshbach resonances in ^{87}Rb have been found.

The experimental procedure used to localize the Feshbach resonance at 1007 G is explained, and a measurement of the 3-body collision rate is reported as a function of the magnetic field close to the resonance. The measured values for K_3 show reasonable agreement with the theory.

Search for Molecules

This chapter deals with the experiments performed to investigate the formation of ultracold molecules exploiting the Feshbach resonance around 1007.4 G studied in the previous chapter. To this end, sections from 8.1 to 8.3 discuss the choice of the ramp speeds used when crossing the resonance both upwards and downwards, and section 8.3 also shows the experimental study performed in order to understand the role of density in the production mechanisms during the magnetic field ramps. Once the key points for the molecule production have been established, section 8.5 presents the experimental protocols used to look for the molecules, while the detection methods employed are explained in section 8.4. Unfortunately none of the measurements performed by us showed conclusive evidence of the production of ultracold molecules. The causes that we believe to be responsible for this are discussed in section 8.6.

8.1 Introduction

From the theory of the molecular formation with the Feshbach resonance, discussed in the last section of chapter 2, we see that in order to form molecules we need to cross the resonance going from negative to positive scattering length. In our case this means that we need to start with a magnetic field higher than the resonance value. Since we start at zero field, this means that we need to cross the resonance as we sweep upward to reach the starting point. Our apparatus cannot detect molecules directly, for example through photo-ionization. Thus the strategy was to produce the molecules, separate them from the remaining atoms, and then convert the molecules back into atoms by reversing the field ramp before probing at zero field. This can be achieved by the ramps shown in fig. 8.1, explained in detail at the end of this section.

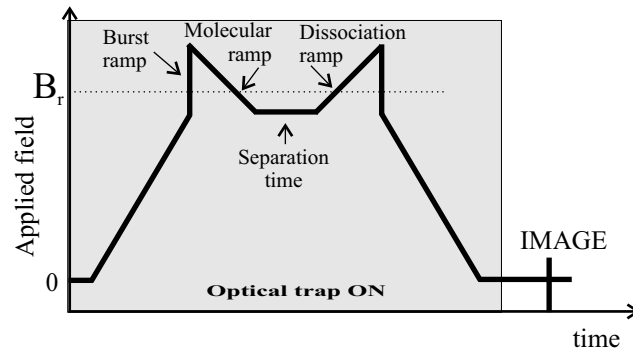


Figure 8.1: Schematic of the experiment. After ramping the magnetic field to 1000 G, a *burst* ramp (the name is justified later in this section) is used to go above the resonance very quickly to reduce losses. Then the molecular ramp crosses the resonance at a certain speed to form as many molecules as possible. These, during a separation time spent a few Gauss below the resonance need to be separated from the atoms using one of the methods described later in this chapter. Subsequently an upward ramp across the resonance is needed to dissociate the molecules again into atoms for probing. Finally, the magnetic field is switched off to be able to use the usual imaging technique for the atoms.

A diagram showing the energy levels of the channels involved as a function of the applied magnetic field is reproduced in fig. 8.2. The open channel corresponds to unbound atoms in the state labelled by $|F = 1, m_F = +1\rangle$ at low fields. The closed channel corresponds to the bound molecular state which is coupled to the $|F = 1, m_F = +1\rangle|F = 1, m_F = +1\rangle$ channel by an s-wave Feshbach resonance at 1007 G.

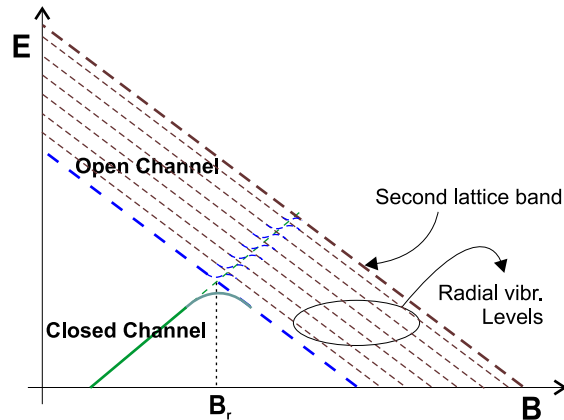


Figure 8.2: Diagram of the energy levels in the open and closed channels around the resonance as a function of the magnetic field.

In an upward sweep (see fig. 8.3 A), if atoms in the open channel adiabatically follow the energy level across the region of the avoided level-crossings, they end up

in excited trap levels, and possibly in untrapped levels. In both cases these atoms will not contribute to the molecule formation during the molecular ramp, as the molecular state can only be reached from the ground state (see fig. 8.3 B). To stay in the ground state we have to cross the resonance fairly quickly in order to *jump* the avoided crossing.

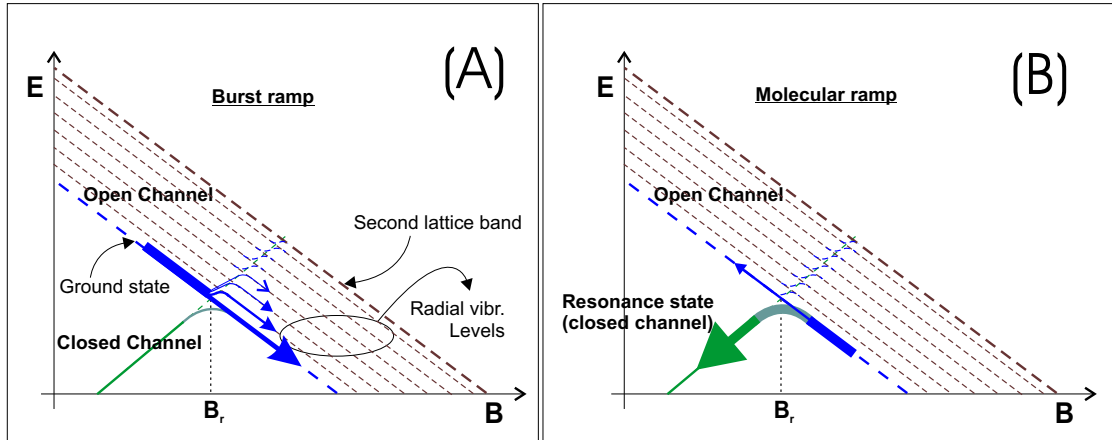


Figure 8.3: Diagram illustrating the effect on the atoms in the ground state of the open channel (BEC) of: (A) the upwards (burst) ramp, and (B) the downwards (molecular) ramp.

The basic steps for the production and detection of molecules can thus be summarized as follows:

1. Sweep the magnetic field up to a few Gauss above the resonance ramping the field very quickly through the resonance itself. This is usually referred to as a *burst ramp*, because the loss during this ramp arises from the enhanced energy of some atoms with respect to the energy of the condensate, and these atoms escape from the optical trap. So the name is used in analogy to an effect studied at JILA [94], where it was used to address the loss of atoms in a similar experiment with ^{85}Rb .
2. Ramp back down across the resonance at the most favourable speed (to be determined experimentally) to produce molecules. This ramp will be referred to as the *molecular ramp* (see fig. 8.3 B).
3. Separate the associated molecules from the remaining atoms.
4. Ramp back up in order to dissociate the molecules back into atoms.
5. Ramp the magnetic field quickly down to zero and probe the atoms in the usual way.

Before looking at the specific production protocols adopted, let us examine the effect of the burst and molecular ramps on the atoms.

8.2 Burst ramps

The first study performed was the measurement of the loss of atoms during the burst ramps to determine the initial number of atoms remaining before the actual molecular ramp.

The ramp used for this part of the experiment is shown schematically in the diagram of fig. 8.4. After ramping the magnetic field up to 2 G below the resonance at a rate of about 20 G/ms, we pause for 5 ms to make sure that the current has reached the asymptotic value (i.e. that the magnetic field does follow the signal from the computer). Then we increase the magnetic field by 4 G (to 2 G above the resonance) in time τ_{ramp} , pause at this upper value of B for 3 ms before ramping the magnetic field down (crossing the resonance as fast as we can: about 100 G/ms) and then we finish by ramping back to zero field in a further 20 ms before detecting the remaining atoms.

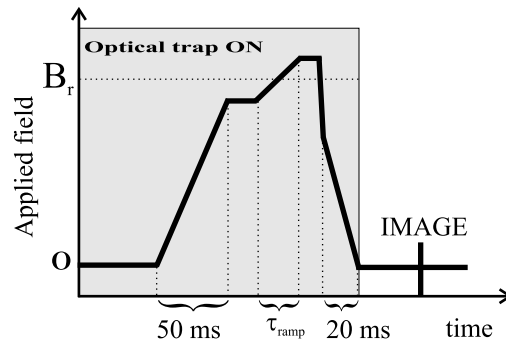


Figure 8.4: Schematic of the magnetic field ramp used in experiments to observe the effect of the burst ramp.

Fig. 8.5 shows the measured relative atom loss: $[N_c(t_i) - N_c(t_f)]/N_c(t_i)$, as a function of the inverse ramp speed during a linear ramp. For this set of data a typical number of atoms was $N_c(t_i) = 5 \times 10^4$. The dotted line shows the expected value for the atom loss of the ground state during the burst as calculated using the many body theory while the dash-dotted line shows the same parameter as obtained using the Landau-Zener result given in eq. 2.57, where δ_{LZ} is obtained from eq. 2.58 (both courtesy of K. Góral). The solid line (half of the many body value) is printed only to guide the eye through the trend of the experimental points, and is not a fit to our data. To hold the atoms during the ramps we used a lattice of potential depth $11 E_r$. The measured loss is smaller than the theoretical curves. This is probably due to the fact that the formula gives the loss from the ground state whether the atoms are expelled from the trap or are only promoted to an excited trapped state which is still present in the absorption picture. Unfortunately there is no clear bimodal distribution that distinguishes them from the atoms in the BEC, therefore we were not able to count them as lost. We only performed this

measurement with the crossed-beam dipole trap at two ramp speeds: 0.05 ms/G and 1 ms/G. Both traps exhibited comparable loss at these two speeds: about 15% for the fast burst ramp (0.05 ms/G), and about 40% at 1 ms/G.

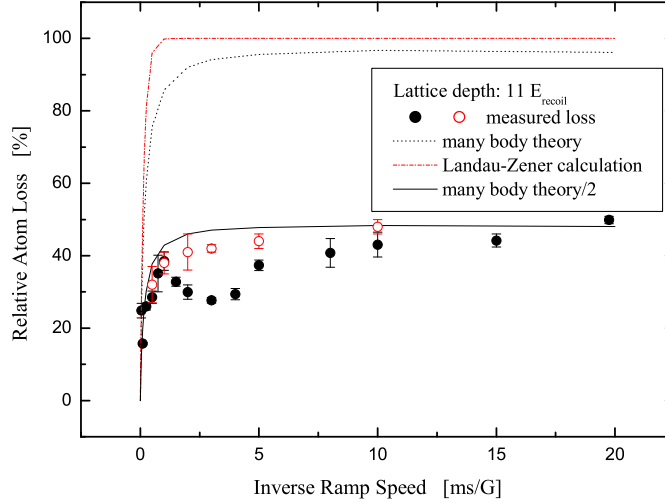


Figure 8.5: The fraction of atoms lost during the burst ramp; (\bullet) with a longitudinally misaligned lattice, (\circ) with a better aligned lattice. The dotted line shows the expected value using the many body theory while the dash-dotted line shows the Landau-Zener calculation [Courtesy of K. Góral]. The solid line (half of the many body value) is printed only to guide the eye, and is not a fit to the data.

The dip around 3 ms/G, seen in fig. 8.5 (solid circles), was consistently observed in the first batch of data taken at this lattice depth. But this effect disappeared after having improved the overlap along the longitudinal axis of the waists of the down-going and retro-reflected beams (open circles). This mismatch was partly the reason why initially we could not achieve standing waves deeper than $11 E_r$. The data shown as open circles were taken after improving the longitudinal alignment (but reducing the intensity to have again the same depth), and the feature was never observed again. We speculate that it may be due to the fact that when the retro beam forms its minimum waist in a different longitudinal position from the down-going beam, the overall optical potential has a larger radial extent. This situation may let atoms which have been promoted to even more excited radial vibrational states of the potential remain trapped and be probed (see fig. 8.2). For very fast or very slow ramps the two alignment configurations lead to the same observed losses. In the case of very fast ramps this can be explained because more highly excited states can be populated that are not kept by either trap. In the case of a slow ramp it is mostly the low-lying radial vibrational states that are excited, which are probably safely trapped by both traps. Although the exact mechanism

is not clear, the fact remains that the atoms detected include some which are not in the ground state, but, as said above, there is no clear bimodal distribution that distinguishes them from the atoms in the BEC.

To make molecules, the burst ramp is needed to reach magnetic fields above the resonance prior to molecule formation. For this we wanted the smallest losses, so we chose the fastest ramp speed of about 0.05 ms/G, giving losses only around 15%. We also used an upward ramp to dissociate molecules back into atoms. This required slower ramp speeds of around 1 ms/G, where the loss is as high as 40%. This loss is not a problem because this ramp acts as a burst only on the atoms that were never converted into molecules and which we do not want to detect anyway.

8.3 Molecular ramps

The second study was performed with downward ramps, or molecular ramps, at different speeds. The magnetic field was swept from above the Feshbach resonance to below, as illustrated in fig. 8.6. After ramping the magnetic field magnitude in 50 ms to about 10 G below the resonance, we suddenly jump to a value some 50 G above the resonance (at 0.05 ms/G) to make sure that the burst ramp has little effect on the initial number of atoms. Then we allow a settling time of 3 ms at 5 G above the resonance before ramping down to 1 G above the resonance in 0.5 ms. The molecular ramp linearly crosses the resonance, in variable times, to end 1 G below it. After a short waiting time at this final value of the magnetic field (typically 1 ms, and at this stage the optical trap had already been turned off), we ramp the field down to zero over 10 ms, and allow a further 4 ms of time of flight before imaging. The total time of flight is counted from when the optical trap is switched off.

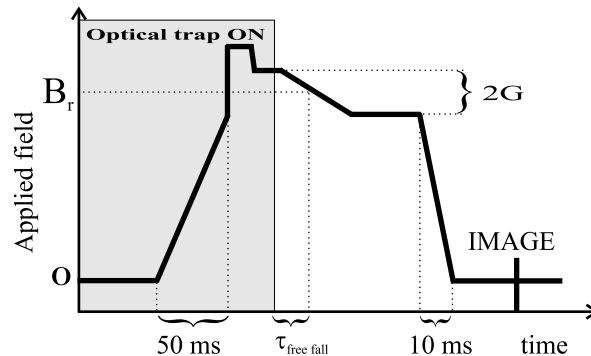


Figure 8.6: Schematic of the experiment to observe the effect of the molecular ramp.

The density of the cloud at the time of crossing the resonance depends on the parameter $\tau_{\text{free fall}}$, which indicates the time between the moment when the optical trap is switched off and the time when the magnetic field crosses the resonance

position; we can estimate the density at that stage from the expansion of the released condensate (as explained below). When the resonance is crossed while the atoms are still held in the trap, there is no free fall, and a negative number is used to indicate the amount of time the atoms and molecules formed have been together in the trap (see fig. 8.7). The number of atoms before the molecular ramp was about 9×10^4 for atoms held in a lattice, and 4×10^4 for atoms in the crossed-beam dipole trap.

The relative atom loss induced by the molecular ramp is plotted in fig. 8.7 for different traps and free fall times. Denser atomic clouds show higher losses due to higher rates of molecule formation. For a lattice released 1 ms before crossing the resonance the dependence of the relative atom loss as a function of the ramp speed is also reported on the graph. Slower sweeps lead to more adiabatic transfer into molecules, and hence to higher atom loss. Two theoretical calculations for this case are also shown in fig. 8.7. The dotted line represents the Landau-Zener result (namely, the evaluation of eq. 2.57 with the Landau-Zener parameter given by eq. 2.58 reported in chapter 2), while the solid line represents the result of a many-body calculation (microscopic quantum dynamics approach) described in [66]. These theoretical curves have been calculated by K. Góral (Oxford) for a mean density of 10^{13} cm^{-3} and agree reasonably well with the 1 ms expansion lattice curve, at least for slow ramp.

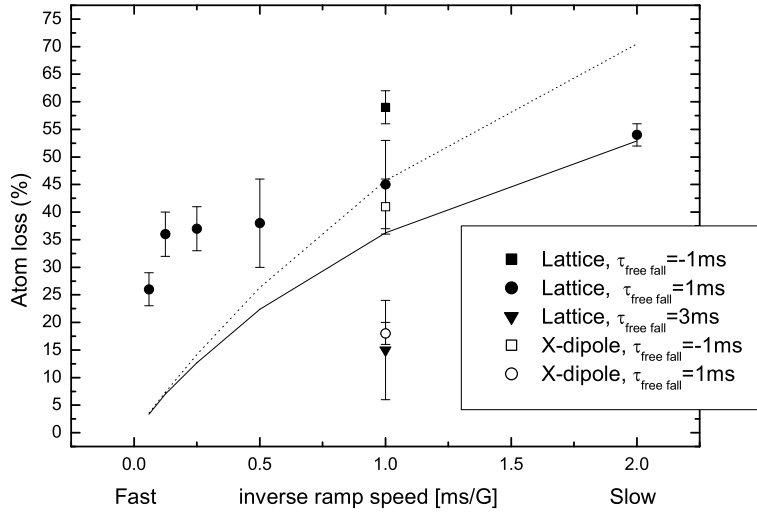


Figure 8.7: Measurement showing the percentage atom loss versus the inverse ramp speed during a molecular ramp; for an inverse ramp speed of 1 ms/G measurement at different densities are shown. [X-dipole indicates the crossed-beam dipole trap]. The dotted line is the Landau-Zener theoretical calculation for the lattice after 1 ms t.o.f., and the solid line is the many-body calculation (by K. Góral).

For the BEC released from the crossed dipole trap, the density has been calculated using the expansion law given in [95]. For the experiments with atoms released from the standing wave we estimate the density considering that the cloud has very quick expansion in the tightly squeezed axial direction, while the expansion in the radial direction can be neglected over 1 or 3 ms. In table 8.1 are reported the number densities obtained from this calculation for the different cases examined experimentally.

$\tau_{\text{free fall}}$ (ms)	$n/10^{12} \text{ cm}^{-3}$ (Lattice)	$n/10^{12} \text{ cm}^{-3}$ (X-dipole)
-1	150	50
1	13	30
3	8	-

Table 8.1: Densities of the atom cloud at the moment the magnetic field was crossing the resonance during the molecular ramp. Positive free fall times mean that the optical trap had been switched off $\tau_{\text{free fall}}$ ms before crossing the resonance, whilst a negative time means that the optical trap was switched off $\tau_{\text{free fall}}$ ms after having crossed the resonance.

Within the two channel approach used in [66] to describe the adiabatic association of molecules by ramping linearly through the resonance, the losses in the atomic cloud are supposedly caused by the association of the atoms into molecules. Therefore we see that a slow ramp is best, and that the slower the ramp the better the molecule production. Bearing in mind the hypothesis that losses are due to molecule formation, we can deduce from fig. 8.7 that, the denser is the cloud, the more efficient is the production of molecules. But there are some practical considerations to be made. The lifetime of these molecules is very short. As explained in chapter 2, this arises because the most likely separation of the two associating atoms is so small that the de-excitation of the molecules to lower bound states due to 3-body collisions between free atoms and the coupled pairs is highly probable. This de-excitation becomes more probable in denser systems. These considerations, and the lack of a complete theory describing such loss mechanisms, mean that a range of ramp speeds must be experimentally investigated in order to determine the optimum balance between the requirements of (a) reducing the losses due to de-excitation by increasing the ramp speed, and (b) increasing the efficiency of the production of molecules by reducing the ramp speed.

The experience of a similar experiment [63] suggests that a ramp speed of 1 ms/G to cross the resonance and go 2 G below it converts 10% of the atoms into molecules. We found higher losses for the same ramp speed. As for the atom density, we explore all the possibilities, but the density reported in [63], for the atoms at the moment of crossing the resonance, has the same order of magnitude as that of our atoms trapped in the crossed-beam dipole trap.

8.4 Separation methods

As already stated, we cannot detect molecules directly, but must dissociate them back into pairs of free atoms before imaging. The fraction of atoms associated into molecules must be spatially separated before dissociation and imaging. At least two methods are possible for distinguishing the molecules from the atoms. One exploits the difference in the magnetic moments of the atoms and molecules: the Stern-Gerlach method adopted in [63]. The other relies on the diffraction of the atoms and molecules from a pulse of the standing-wave potential, which works if the molecules retain some of the coherence of the original condensate. These two methods are described in detail here, while the complete experimental protocols for both, and the observations will be left to the next sections.

8.4.1 Diffraction

The idea behind this method is to flash the standing wave onto the atoms and molecules to observe diffraction as shown in section 5.4. Provided the molecules and the atoms are still coherent they should also spatially separate from each other due to their different masses (resulting in the diffracted momentum states of the molecules having half the velocity of the atoms) as described below.

The procedure itself is very simple. At the end of the molecular ramp we sit for 1 or 2 ms at the final field (1 or 2 G below the resonance) and during this time the standing wave is flashed on the mixture of atoms and molecules. Molecules have twice the mass of the atoms, hence the separation between the diffracted orders should be half the separation between the diffracted orders of the atoms. The central orders will always be superimposed, but the first diffracted order of the molecular cloud should sit in the gap between the zeroth and the first order of the atoms. After the pulse we need to ramp up the magnetic field to dissociate the molecules and then switch it off very quickly, and allow some further time of flight before detection.

The experiment is a very ambitious one, because it would separate spatially the atoms from the molecules only if the whole system remains coherent. It is also very tricky from the point of view of the signal to noise ratio, as it aims to detect a small fraction of atoms coming from the dissociation of the molecules in each diffracted order. Even assuming that all the molecules, for a specific pulse length, populate the first order, and that 7% of the initial atoms are converted into molecules, we would only have about 3000 atoms in each of the two diffracted orders of the molecular cloud (the number of the condensate atoms held in the crossed dipole trap before the molecular ramp is about 4×10^4). Moreover, after a sufficiently long time of flight so that the atomic orders are separated enough to show the presence of the molecular diffracted order, the optical density of such a tiny number of atoms would be almost at our detection limit. The positive aspect

of this experimental approach, however, is that the standing wave can be applied very quickly after the molecular production so that the atoms and molecules can begin to separate immediately, thus reducing the number of de-excitation collisions.

8.4.2 Stern-Gerlach experiment

This method was successfully used in [63] to show evidence of the formation of molecules in a similar experiment, and whilst it does not give information on the degree of coherence of the associated molecules, it has the advantage of creating only one molecular cloud (which increases the signal to noise ratio in the images) and allows the atoms and the molecules to be separated further apart than can be achieved with the other method during a typical experimental time-of-flight.

The technique relies on the different magnetic moment of molecules and atoms to separate them with a magnetic field gradient. Experimentally, at the end of the molecular ramp, the field sits at the final value for a variable time, typically 2 ms, during which an inhomogeneous magnetic field with a gradient of 21 G/cm along the vertical axis is applied to decelerate the gravitational fall of the molecules whilst it further accelerates the atoms in the direction of \vec{g} . Just before ramping up again for the dissociation of the molecules, the Stern-Gerlach field (gradient) is turned off. In the meantime the molecules should have fallen only a small amount, whilst the atoms have moved downwards a large amount. At this point the experiment can continue as usual, with dissociation ramp and imaging, and all the atoms imaged in the upper cloud should have previously been molecules.

The value of the magnetic field gradient to levitate molecules for the Stern-Gerlach separation is obtained experimentally by looking at the gradient for which the molecules are supported against gravity, when in a field 2 G below the resonance. This is calculated from the requirement:

$$mg = \frac{dE}{dz} = \frac{dE}{dB} \frac{dB}{dz} \quad (8.1)$$

where m is the mass of the molecule, $\frac{dB}{dz}$ is the field gradient, and the slope $\frac{dE}{dB}$ depends on the magnetic field as shown in fig. 2.9. For the resonance state, the slope $\frac{dE}{dB}$ was measured in [63] as a function of B , and 2 G below the resonance it is about 1.2 MHz/G. This requires the gradient of the levitating field to be about 35 G/cm. Unfortunately, we cannot reach that field with our Stern-Gerlach coil. For the atoms in the state $|F, m_F\rangle = |1, +1\rangle$ the magnetic moment (obtained by taking the first derivative with respect to B of the Breit-Rabi formula given in equation 3.3) is about -1 MHz/G, leading to a required levitating gradient of 21 G/cm, and in the opposite direction as the one required to levitate the molecules. We can produce 21 G/cm, and we applied this gradient in the direction that opposes the free fall of the molecules (being only 3/5 of the required levitating field), whilst pushing down the atoms with an extra force. To prevent further collisions between

the atoms and the molecules we need to separate completely the two clouds as soon as possible. This is safely achieved by applying the field gradient for 2 ms, as shown by the following simple calculation. The size along z of the probed cloud after 3 ms of time of flight is $\sigma_z = 13 \mu\text{m}$, therefore to separate the atomic cloud from the molecules, i.e. to achieve $\Delta\bar{z} = 2\sigma_z$, we need to apply the Stern-Gerlach field for a time t such that the distance fallen by the molecules during that time is at least $\Delta\bar{z}$ shorter than the distance covered by the atoms. For the atoms we have $\Delta z_A = gt^2$, while for the molecules we have $\Delta z_M = \frac{1}{5}gt^2$, so the difference in position will be $\Delta z = \frac{4}{5}gt^2$. Therefore, the minimum time for which we have to apply the field, in order to separate the two clouds by at least $2\sigma_z$, is $t = 1.3$ ms.

8.5 Experimental protocols

The initial part of the protocol is identical to the one described in section 8.3, up to the time when we get to 1 G above the resonance. Up to this stage the optical trap is always present. Next, the molecular ramp follows, in which the magnetic field is ramped linearly down to 2 G below the resonance, i.e. 1003.25 G, since in our calibration the resonance is centred at 1005.25 G (see section 7.2). Alternatively we would ramp linearly to just above, at, or below the resonance and then jump to 1003.25 G in 0.1 ms (see fig. 8.8).

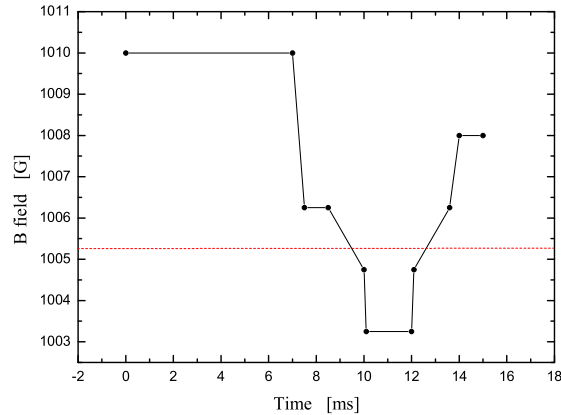


Figure 8.8: Magnetic field ramps for associating and dissociating molecules.

This field was kept for 2 ms before starting the dissociation ramp with a shape symmetric to the molecular ramp. During these 2 ms either of the two separation methods described above were applied in order to spatially isolate the associated molecules. Next, the magnetic field is ramped down to zero for detection in about 10 ms.

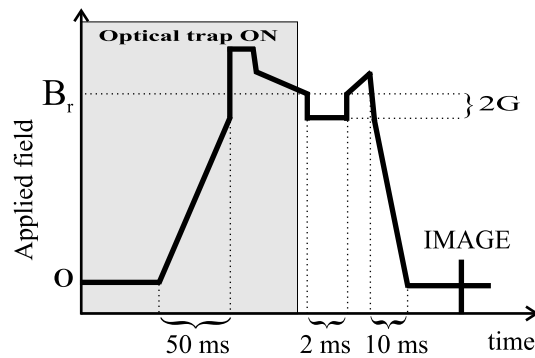


Figure 8.9: Schematic of the experimental routine for the production of molecules.

In a first series of experiments aimed at observing the formation of molecules (see fig. 8.9), the optical trap was switched off at different times during the molecular ramp in order to vary the density of the atoms when crossing the resonance, as discussed in section 8.3. No molecules were seen to be converted back to atoms.

Performing the experiment in free fall has the advantage of giving a handle on the density of the atoms at the moment of the association, but has the disadvantage of making us rush through all the sequence due to the long time required to turn off the magnetic field.

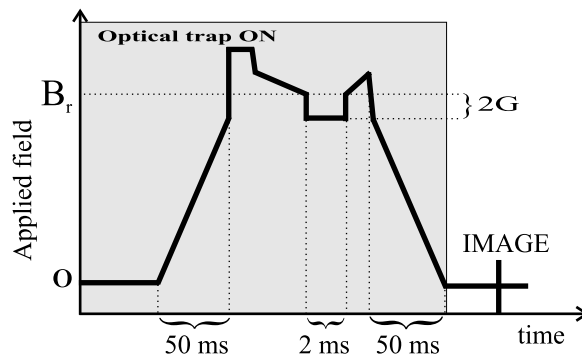


Figure 8.10: Schematic of the experimental routine for the production of molecules in the optical trap. To separate the atoms from the molecules, a Stern-Gerlach is applied during the 2 ms stage before the molecules are converted back into atoms.

To eliminate the long time of flight problem, we tried experiments entirely in the optical trap (see fig. 8.10). In this case we used the Stern-Gerlach field gradient to selectively get rid of the non-associated atoms from the trap during the 2 ms stage before the dissociation ramp. No molecules were observed using a crossed-beam dipole trap. We also tried with the standing wave, but this time before the molecular ramp started we reduced the intensity of the optical trap beam to a value such that it was possible to expel atoms from it with the 21 G/cm field gradient. No signal was observed this way either. But this method was never very

reproducible because the amount of losses was very sensitive to the depth of the lattice.

We must therefore analyze the possible causes of the non-observation of the molecules. One possibility of course is that the molecules were never produced in the first place, but this seems unlikely because the amount of 3-body loss during the molecular ramp, as we have seen, does not account for the observed loss, and two body inelastic collisions can be ruled out as they cannot lead to spin relaxation of the electronic ground state. Higher order losses at that density are even less likely. We assume then, as a starting point, that of the observed 45% atom loss during the molecular ramp, only a fraction survives the collisional de-excitation, and comparison with similar experiments would suggest that this should be at least 10% of the initial number. The question is then, where has the remaining 10% gone?

One possible explanation is that the molecules were never converted back into atoms, but this seems unlikely, because we have tried dissociation ramps for many different speeds around those for which molecules had been successfully converted into atoms in another experiment.

A second possible explanation is that the dissociation energy was so high that due to the long time of flight the optical density of the small atomic cloud coming from the dissociated molecules was too small to emerge over the background noise. In order to avoid this we should take images after a shorter time of flight. This means either probing at high field, or switching off the magnetic field more quickly. Unfortunately we are not able to do the latter due to the long decay time of our magnetic field. The causes of this long decay time must be looked for in the features of our experimental apparatus discussed in the next section. While as far as the former option is concerned, it would have involved setting up a different laser system to realize a closed loop transition for the atomic level splitting around 1000 G, and locking these lasers nearly 1 GHz away from their low-field resonance (which would have also required some expensive pieces of apparatus). This option was not pursued because, by the time we had got to this stage, the experiment had already been performed successfully at *Max-Planck Institute for Quantum-Optics* (MPQ) in Garching [63]. It did not seem that, with our apparatus, our method would have explored enough interesting new physics to justify the effort and the expense required. We then decided to move on to a different experiment, for which our apparatus is more suitable, as it is explained in the last chapter.

8.6 Limitations of the experimental setup

I should recall that the initial option we pursued to probe the molecules had been to separate them from the unconverted atoms, dissociate them back into atoms and then probe these atoms using the usual probing transition at zero field. Our experiment showed no evidence of these atom clouds coming from the converted

molecules, but the overall time of flight after dissociation had been always at least 15 ms. This long time was dominated by the 13 ms needed to make sure that the field was down to zero at the moment of taking the image. In the experiment performed at MPQ the equivalent ramp takes only 2 ms. Our coils though, are made of 400 turns, so that the effect of the inductance is large. We considered completely opening the circuit which takes the current to zero within the response time of the control box (about 1 ms), however, a Hall probe detector placed at various locations along the vertical direction near the coils detected a residual field caused by eddy currents which decayed with a time constant of about 10 ms. This resulted in an even longer time for the final field to fall to zero than by ramping the current in the coils. We tried to reduce the eddy currents by dismantling the support for the coils and optics, and cutting slots in various places to prevent closed loops that could act as an electrical circuit. This did not help much because the radial component of the magnetic field created eddy currents that circulate along vertical planes on the metallic mount supporting the coils.

A different design of the coils, with less turns and more current could have allowed the field to be ramped down more quickly, and eddy currents could have been reduced with non metallic coil-supports. This again would have required a large change to the apparatus, which did not seem justified after molecules had already been created at MPQ. The existing coils had only been designed to produce a quadrupole field, and in that case the field at the centre is always zero so there would never be problems with imaging after a short time of flight. Moreover the current for our strongest TOP trap is about 10 A, which is two thirds of the current needed to generate 1000 G, and so also the eddy currents generated during the quadrupole field phase decay much more quickly, and no effect was ever observed on the atoms.

8.7 Summary

This section has described the experimental procedures used to exploit the Feshbach resonance at 1007 G in ^{87}Rb to associate condensed atoms into molecules. The relative atom loss in ramping the field across the resonance has been measured in both upwards ramps and downwards ramps. In these latter ramps the association is supposed to be the only possibility for losses in a two-body treatment of the dynamics, but, although about 45% of the atoms were observed to be lost during this molecular ramp, no signal was observed if the non-associated atoms were removed before dissociating the molecules again into atoms.

Conclusions and outlook

This thesis has presented the construction, optimization, and operation of an apparatus capable of producing Bose-Einstein condensates of about half a million ^{87}Rb atoms in a TOP trap in under a minute, reliably on a daily basis. The work required to obtain BEC in the $|F = 1, m_F = -1\rangle$ atomic state, together with a brief characterization of the condensates, has been reported. Two types of optical potentials have been set up, and integrated with the BEC apparatus, that are capable of trapping the condensates in either a vertical standing wave or a crossed-beam dipole trap. Both traps have been characterized in terms of their depths, frequencies, and lifetimes. The optical potentials have been employed to hold the atoms while they are transferred into the $|F = 1, m_F = 1\rangle$ atomic state, where they cannot be kept in the magnetic trap. This transfer is achieved with radio frequency ramps, and has proved to be almost 100% efficient.

The reason for transferring the atoms into this atomic state is that a number of Feshbach resonances had been predicted to occur for ^{87}Rb in this state [33]. Once the atoms were optically trapped, the magnetic trap coils became available to be used to generate a homogeneous magnetic field on the atoms by reversing the current in one of the two coils. This was done and the resulting field was calibrated by means of RF spectroscopy.

Finding a Feshbach resonance gave us the chance to tune the scattering length and induce the formation of ultracold molecules by adiabatically associating atoms in the ground state. The resonance close to 1000 G for ^{87}Rb atoms in the ground state has been localized. The width of this resonance is only about 0.2 G [34], which means that a stability of the magnetic field of at least one part in 10^5 is needed to appreciate the varying strength of the interaction across the resonance. This stability has been achieved thanks to feedback control electronics that uses a Hall-effect probe sensor and a MOSFET to regulate the amount of current flowing through the coils.

A study of the loss due to 3-body collisions around the resonance has been performed, measuring the three-body loss rate constant and comparing the result with the theory by T. Köhler [92, 93].

In order to investigate the formation of molecules using the Feshbach resonance, the losses of atoms from the BEC while ramping the magnetic field up and down across the resonance were measured and the results obtained were presented. Several attempts at observing evidence for the formation of molecules have been carried out, leading to no direct evidence of molecules being formed. Two different methods have been employed to try and separate the atoms from the molecules before detection. The first tried to diffract atoms and molecules with a pulse of the standing-wave potential, which should spatially separate them due to the different mass of atoms and molecules; this would have also required that the molecules had preserved a certain degree of coherence. The second is based on a Stern-Gerlach field being applied just after the production to separate the atoms from the molecules due to their different magnetic moments. Neither method showed an atomic cloud in the location where a molecular cloud should have been before dissociation. The second method in the meantime was successfully employed elsewhere [63], giving evidence of molecule formation.

We believe that the reason we did not observe the molecules was because the eddy currents circulating in the metallic part of the apparatus near the cell made the magnetic field turn-off times too long. This caused the molecular cloud to be freely expanding for longer and hence the absorption signal would be too weak to detect, given the energy of the released molecules. This limitation of our BEC machine makes it very hard to perform experiments in which such a high magnetic field needs to be turned off relatively quickly. For this reason we had to give up these attempts with the existing apparatus. Changes to the apparatus that could have been implemented in order to detect the molecules were a new laser system to detect the atoms from the dissociated molecules at high field, or new trap coils with less metallic components near the cell. These have not been implemented because, as mentioned earlier, by the time we had reached this stage another group had successfully observed $^{87}\text{Rb}_2$ molecules using a slightly different apparatus, but all the same demonstrating the validity of our experimental approach. Also, there were several other experiments which produced molecules by associating pairs of fermions near a Feshbach resonance; these have been found to be very long-lived molecules, i.e. stable against collisions. Paradoxically, the tighter binding of molecules formed from two bosonic atoms leads to a shorter lifetime. To understand this we must remember that in these molecules the two bosonic atoms have a small separation, and hence the Franck-Condon factors (overlap) with other vibrational levels is large; this means that collisions cause the population to spread out over many vibrational levels. We cannot detect molecules in any vibrational state other than the one involved in the Feshbach resonance, so transfer to another vibrational level is effectively a loss in our experiment.

The decision was made for our apparatus to be used to pursue experiments for which its design is more suitable. Our group had also been engaged during the last two years in a project to design, test and build a spatial light modulator (SLM) to trap the atoms in an array of dipole traps which can be moved and brought closer to enhance the interactions between two traps. SLMs are widely employed in optical-tweezers experiments and were recently proposed as a versatile tool to create optical potentials for cold atoms [96]. Examples include liquid crystal devices with a matrix of pixels each of which can be programmed to induce a given retardation on an incoming laser beam. The result is a generalized phase grating that is able to produce an arbitrary light pattern, i.e. a computer generated hologram. This pattern can be varied in time, generating a dynamic optical potential for atoms [97].

The implementation of the SLM on our apparatus is not part of this thesis, but is the next experiment for which our setup can be employed. In the last few months it has been mounted on our apparatus, and preliminary experiments have been performed on trapping our ^{87}Rb BEC. These experiments already show that the condensate can be loaded into a double-well potential, and that the two components can subsequently be split apart over distances of the order of 50 microns. This result is promising for the realization of an interferometer with trapped atoms. Possible future experiments could be on deformable optical lattices, with applications to quantum information processing.

Rubidium data

Relevant physical properties for ^{87}Rb atoms are given below. For the cases where these depend on the specific atomic transition, they are given for the D_2 line of ^{87}Rb , for which a diagram of its hyperfine structure is shown in figure A.1, and which has specific relevance to this thesis.

Quantity	Symbol	Value
Atomic number	Z	37
Nuclear spin	I	$3/2$
Mass	m	1.443×10^{-25} kg
Wavelength (vacuum)	λ	780.241 nm
Wave number (vacuum)	$k/2\pi$	12816.5 cm^{-1}
Natural linewidth (FWHM) Decay rate	Γ	$2\pi \cdot 6.065$ MHz 38.11×10^{-9} s
Saturation intensity π -pol ($F = 2 \rightarrow F' = 3$)	I_{sat}	2.503 mW cm^{-2}
Resonant cross section π -pol	σ_0	1.938×10^{-9} cm^2
Saturation intensity σ -pol ($ F = 2, m_F = \pm 2\rangle \rightarrow F' = 3, m_{F'} = \pm 3\rangle$)	I_{sat}	1.67 mW cm^{-2}
Resonant cross section σ -pol	σ_0	2.907×10^{-9} cm^2
Recoil velocity	$v_r = \hbar k/m$	5.88 mm s^{-1}
Recoil temperature	$T_r = mv_r^2/k_B$	362 nK
Zeeman shift of $5S_{1/2}$ $F = 2$	$1/2 \mu_B \times m_F$	700 kHz $\text{G}^{-1} \times m_F$
Zeeman shift of $5P_{3/2}$ $F = 3$	$2/3 \mu_B \times m_F$	933 kHz $\text{G}^{-1} \times m_F$
Scattering length at $B = 0$ $ F = 1, m_F = 1\rangle$	a	5.31 nm

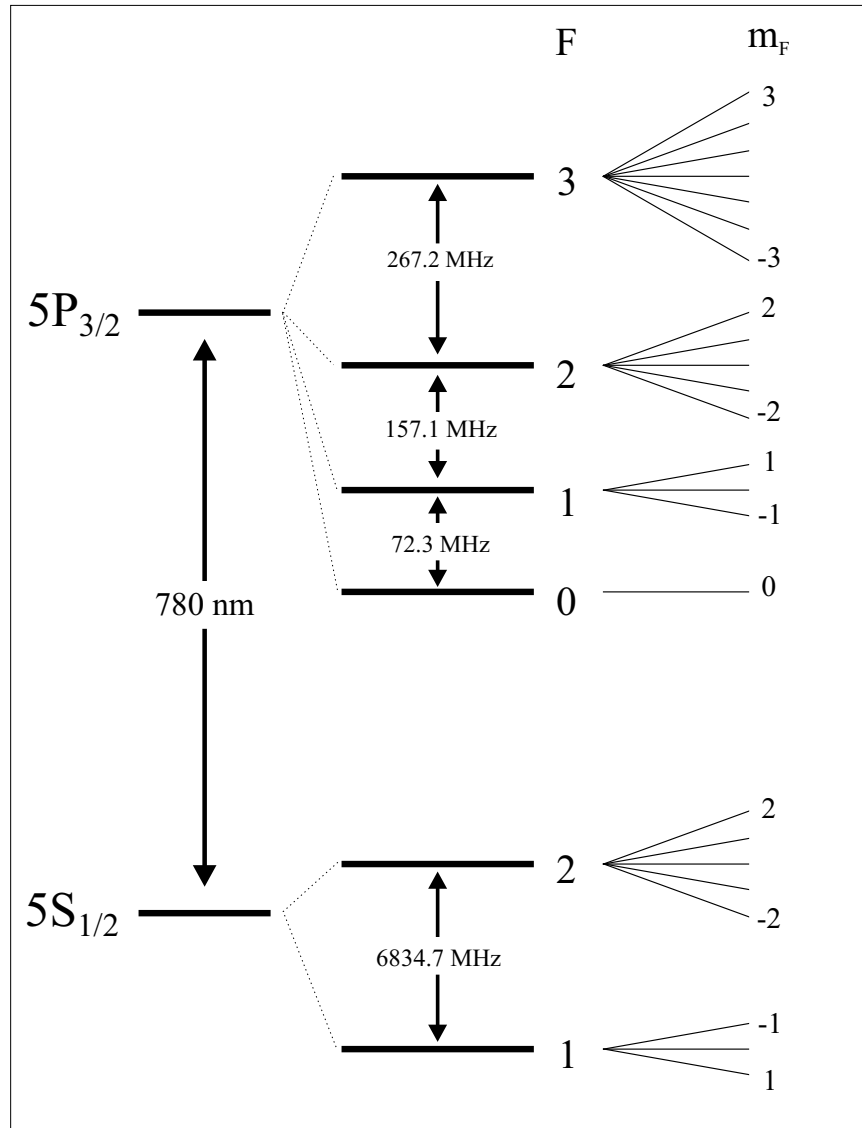


Figure A.1: Hyperfine structure of the D_2 line in ^{87}Rb .

Image analysis

We record absorption images of ^{87}Rb atoms in the hyperfine level $5S_{1/2}$, $F = 2$ using light tuned on the resonance of the $F = 2 \rightarrow F' = 3$ transition of the D2 line. The setup used, and the relevant physical quantities have been described in chapter 3. Our CCD camera records frames of 768×512 square pixels of side length $9 \mu\text{m}$. The procedure to obtain such pictures from the three images taken, was also described in section 3.7. The atom number is proportional to the optical density $D(x, z)$ (see eq. 3.7), and so we analyse the image by determining the optical density value at each pixel.

Our starting point for the analysis is therefore to obtain the number of atoms imaged at each pixel, whose effective area is taken to be: $A' = \frac{\text{pixel area}}{\text{mag}^2}$. The measured magnification of our imaging telescope is $\text{mag} = 2.59$, the pixel area is $A = 81 \mu\text{m}^2$, hence $A' = \frac{A}{2.59^2} = 12 \mu\text{m}^2$. The total number of atoms is then

$$N = \frac{A'}{\sigma} \sum_p D(p) \quad (\text{B.1})$$

where the sum is extended over all the pixels $p(x, z)$ within a selected region of interest. The absorption cross-section σ was defined in eq. 3.6. To take into account the effect of the remaining background, a Gaussian fit is performed on both the x and z profiles, and the offset of the resulting Gaussian is taken as the zero optical density value. This offset is subtracted from the signal obtained from each pixel within the region of interest.

The radii σ_x and σ_z of an atom cloud are given by the $1/e$ radii of the Gaussian fit on the two profiles obtained by summing in the two directions (and then multiplied by $\frac{9\mu\text{m}}{2.59}$ to convert them from pixels into μm).

The temperature of the thermal cloud is obtained, for clouds in the magnetic trap, directly from the fitting parameters, assuming

$$\frac{3}{2}k_{\text{B}}T = \frac{1}{2} \frac{\mu b'^2}{4B_0} (2\sigma_x^2 + 8\sigma_z^2) \quad (\text{B.2})$$

where the additional factor $1/2$ comes from the choice of the fitting function. The density of the atoms is calculated as

$$n = \frac{N}{\pi^{3/2}\sigma_x^2\sigma_z} \quad (\text{B.3})$$

and the density in phase space is calculated as:

$$\rho = n\lambda_{\text{dB}}^3 = n\left(\frac{2\pi\hbar^2}{mk_{\text{B}}T}\right)^{3/2}. \quad (\text{B.4})$$

We have used a Gaussian fit to extract properties of both the thermal and condensate clouds because the difference with the parameters extracted by fitting with an inverted parabola was within the shot to shot fluctuation.

Most of the pictures were taken after a time-of-flight expansion τ of the atomic cloud. To infer the temperature using eq.B.2 we need the size of the cloud whilst still in the trap, i.e. for $t = 0$. These were calculated assuming that the cloud, during the time τ , had undergone a ballistic expansion according to the relationship

$$\sigma_i(t = 0) = \frac{\sigma_i(\tau)}{\sqrt{1 + \omega_i^2\tau^2}}. \quad (\text{B.5})$$

Calculation of the number density per lattice well

In this appendix, the number density in the individual lattice sites is calculated. The experimental inputs will be the measured lattice depth, the size of the condensate in the TOP trap at the time of the transfer, and the total number of atoms. Moreover, each well is considered as a 2D pancake-shaped cloud. This assumption will now be justified.

The important scaling lengths in a trapped 3D gas are the radius of the cloud, R , the scattering length, a , and $\xi = (8\pi na)^{-1/2}$ [3], called the healing length, which represents the distance over which the wavefunction recovers its bulk value when subjected to a localized perturbation. For ^{87}Rb atoms at a number density of $n \simeq 10^{14} \text{ cm}^{-3}$, the healing length is $\xi \simeq 200 \text{ nm}$. We see then, that for a 3D condensate these three quantities are such that $R \gg \xi \gg a$, and the Thomas-Fermi approximation describes the system well. When the radial dimension of the cloud, or its axial one, becomes smaller than the value ξ defined above, the BEC is restricted to one or two dimensions, respectively [98].

The case of interest to us, is when $R_{\perp} > \xi > R_z$. This regime is reached, in a harmonic trap, when the chemical potential for the 3D cloud is such that $\mu_{3D} = \frac{4\pi\hbar^2}{m}an \leq \hbar\omega_z$. In chapter 2 we obtained an expression for ω_z in the lattice in eq. 2.40, which yields, for $U = 14E_r$ the frequency $\omega_z = 2\pi \times 24 \text{ kHz}$, and hence $\hbar\omega_z = 1.6 \times 10^{-29} \text{ J}$. This is about one order of magnitude bigger than μ_{3D} , and almost 3 orders of magnitude bigger than $\hbar\omega_r$.

Our condensates trapped in the standing wave are therefore 2D gases. The axial profile is assumed Gaussian and it extends itself over the length of the harmonic oscillator in the z direction. The radial profile, however, is still parabolic like in the Thomas-Fermi regime, and is given by [98]:

$$R_{2D} = \left(\frac{128}{\pi}\right)^{1/8} \left(Na \frac{a_{\text{h.o.r}}^4}{a_{\text{h.o.z}}}\right)^{1/4}. \quad (\text{C.1})$$

The in-lattice parameters are evaluated using the equations reported in [99]. The number of atoms in each lattice site is given by the total number of atoms in the condensate divided among the wells populated according to the relationship $N_k = \frac{15N}{16k_M} \left(1 - \frac{k^2}{k_M^2}\right)$, where k is the site index and ranges between $-k_M$ and $+k_M$. The value of k_M is extracted from its expression given in [99], and it depends on the initial cloud parameters (as it comes from the magnetic trap) as well as the lattice parameters. For our typical condensate and lattice parameters the value of k_M is about 14, leading to approximately 30 wells being populated.

The condition required for the atoms in the lattice to remain a superfluid BEC is that the tunnelling rate is higher than the interaction energy between two adjacent wells. Here follows a calculation of the tunnelling rate in a lattice with a potential well depth of $14 E_r$. To obtain the tunnelling rate, as well as the density distribution in each well, we use a Thomas-Fermi profile for the radial direction and a Gaussian profile for the axial direction, normalized to the number of atoms. For each well the number density is locally given by:

$$n_k(\vec{r}) = \frac{2N_k}{\pi^{3/2} a_{\text{h.o.z.}} R_{2\text{D}}^2} \left[1 - \frac{r_{\perp}^2}{R_{2\text{D}}^2} \right] \exp\left(-\frac{(z - k\lambda/2)^2}{a_{\text{h.o.z.}}^2}\right). \quad (\text{C.2})$$

where $R_{2\text{D}}$ is the 2D-Thomas-Fermi radius given above, for the individual lattice site k . The mean density per site is obtained as

$$\langle n \rangle = \frac{1}{N} \int n^2(\vec{r}) d\vec{r}. \quad (\text{C.3})$$

Using cylindrical coordinates, the volume element can be expressed as $d\vec{r} = d\vec{r}_{\perp} dz = 2\pi \cdot r dr dz$. The Josephson tunnelling rate is obtained again from [99] as:

$$E_J = \frac{\hbar^2}{m} \int |\Psi_k(\vec{r}_{\perp}) \Psi_{k+1}(\vec{r}_{\perp})| d\vec{r}_{\perp} [\phi_k(z) \phi'_{k+1}(z) - \phi_{k+1}(z) \phi'_k(z)]_{z=0} \quad (\text{C.4})$$

where $\Psi_k(\vec{r}_{\perp}) \phi_k(z) = \Psi_k(\vec{r})$ is the wavefunction of the atoms in each lattice site so that $|\Psi_k(\vec{r})|^2 = n_k(\vec{r})$, and $\phi_k(z)$ indicates the Gaussian term

$$\phi_k(z) = \exp\left(-\frac{(z - k\lambda/2)^2}{2a_{\text{h.o.z.}}^2}\right) \quad (\text{C.5})$$

while the term $\Psi_k(\vec{r}_{\perp})$ is given by the rest of the wavefunction, including the normalization factor, so that

$$|\Psi_k(\vec{r}_{\perp})|^2 = \frac{2N_k}{\pi^{3/2} a_{\text{h.o.z.}} R_{\text{TF}k}^2} \left[1 - \frac{\vec{r}_{\perp}^2}{R_{\text{TF}k}^2} \right]. \quad (\text{C.6})$$

In the specific case of our condensate, the tunnelling rate for the central wells ($k \ll k_M$) is given by eq. C.4 to be about $E_J = 2\pi\hbar \times 40$ kHz. This number must

be compared to the interaction energy, which for two neighboring lattice sites can be obtained as $2\partial\mu_k/\partial N_k$ [99], where μ_k is the chemical potential of the atoms in the k^{th} well (for details of the expression of the chemical potential for each well see [99]). For the central wells this leads to about $E_{\text{int}} = 2\pi\hbar \times 0.2$ Hz. The comparison confirms that the tunnelling is dominant and the system can still be treated as a superfluid condensate.

From the equations given in this appendix we can obtain one more useful quantity, the mean square density $\langle n^2 \rangle$, which is needed to evaluate the 3-body loss rate as given in chapter 7. This is given by

$$\langle n^2 \rangle = \frac{1}{N} \int n^3(\vec{r}) d\vec{r}. \quad (\text{C.7})$$

Stabilization of the magnetic field

The electronics for stabilizing the magnetic field was designed by D.T. Smith, in the Electronics Workshop of the Physics Department in Oxford, on the model of a similar design used at JILA, Colorado. The circuit, redesigned to fit on two PCI cards, is much more compact than the original design and is placed in one single box. We assembled together the components and calibrated the box on our experiment.

A diagram of the electronic scheme of the circuit is reproduced here as a complement to the description given in chapter 3. The whole circuit is made up of two boards, a reference board (fig. D.2), and a feedback board (fig. D.3). Looking at the scheme of fig. D.1 that illustrates how the two boards are included in the experiment, we can follow the main steps of the stabilization mechanisms.

The control voltage coming from the computer to the LV terminal on the reference board gives the reference voltage for the feedback loop. The actual value of the reference voltage depends on whether the input enable (I/E) TTL switch is *on* or *off* (this also comes from LabView). If it is *off*, the control voltage is directly sent as the reference voltage, otherwise the reference voltage is determined by adding a variable offset to a pre-determined internal reference voltage that is set through the potentiometer RV1 (see the scheme of fig. D.2).

The output of the reference board acts as the control input of the feedback board, where it is compared to the voltage across R15 coming from the Hall sensor through the OP270 *IC1A*. The difference is converted into the output going to the gate of the MOSFET to regulate the amount of current flowing through the coils. This conversion is done by the three operational amplifiers OP270 *IC1B*, *IC2A*, and *IC2B*.

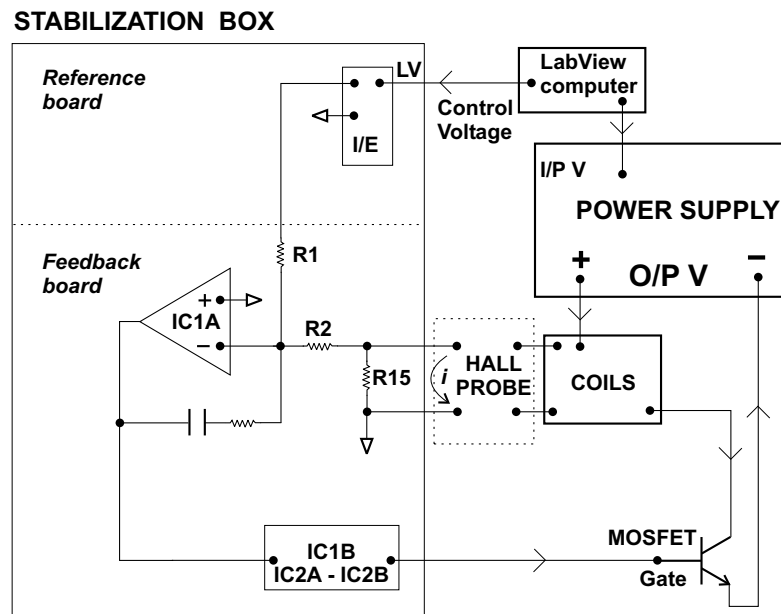


Figure D.1: Schematic of the whole magnetic field production and stabilization circuit.

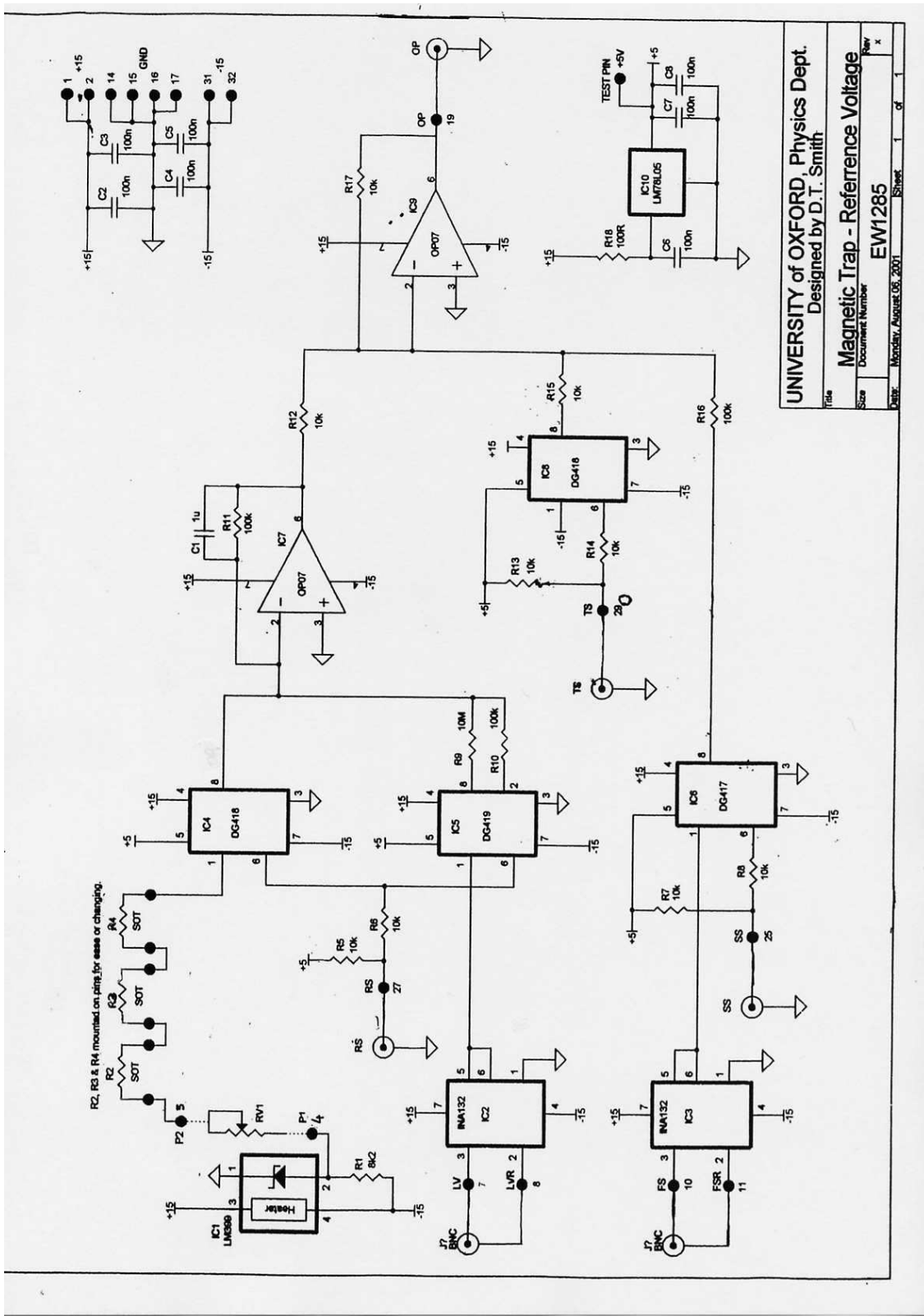
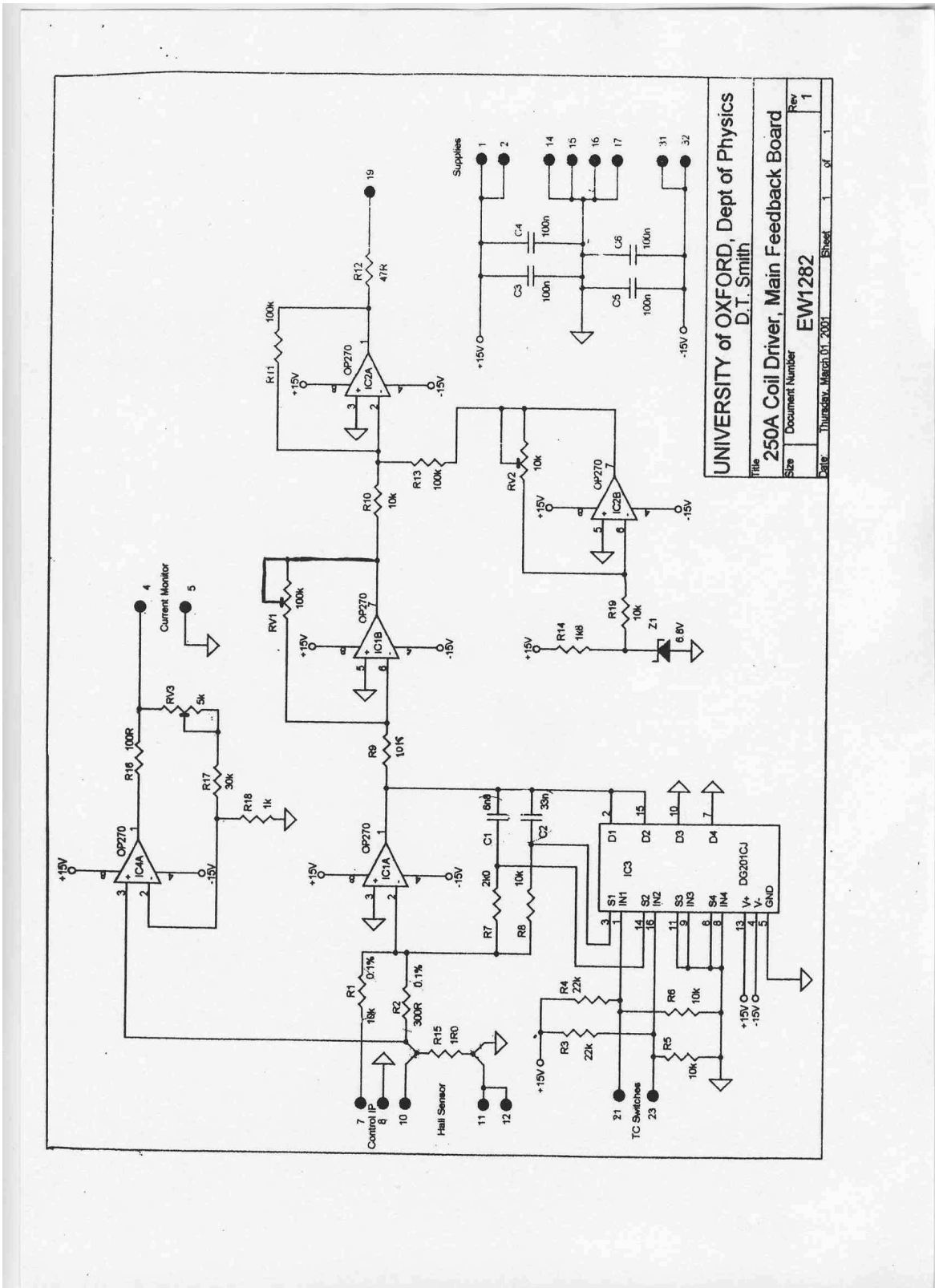


Figure D.2: Electronic circuit scheme of the reference board.



UNIVERSITY of OXFORD, Dept of Physics
 D.T. Smith
 File 250A Coil Driver, Main Feedback Board
 Size Document Number EW1282
 Date Thursday, March 01, 2001 Sheet 1 of 1

Figure D.3: Electronic circuit scheme of the feedback board.

Bibliography

- [1] M. H. Anderson, J. R. Ensher, M. R. Matthews, C. E. Wieman, and E. A. Cornell. *Observation of Bose-Einstein condensation in a dilute atomic vapor*. Science, **269**, 198 (1995).
- [2] W. Ketterle, D.S. Durfee, and D.M. Stamper-Kurn. *Making, probing and understanding Bose-Einstein condensates*. In: "Bose-Einstein Condensation in Atomic Gases". M. Inguscio, S. Stringari, and C. Wieman, editors. *Societ a Italiana di Fisica*, Amsterdam: IOS Press, 1999.
- [3] F. Dalfovo, S. Giorgini, L. P. Pitaevskii, and S. Stringari. *Theory of Bose-Einstein condensation in trapped gases*. Rev. Mod. Phys., **71**, 463 (1999).
- [4] A. Einstein. *Quantentheorie des einatomigen idealen gases: Zweite abhandlung*. Sitzungsber. Preuss. Akad. Wiss., **1**, 3 (1925).
- [5] S. Bose. *Plancks Gesetz und Lichtquantenhypothese*. Z. Phys., **26**, 178 (1924).
- [6] N. Bogoliubov. *On the theory of superfluidity*. J. Phys., **11**, 23 (1947).
- [7] F. London. *The λ -phenomenon of liquid helium and the Bose-Einstein degeneracy*. Nature, **141**, 643 (1938).
- [8] D. A. Bell, H. F. Hess, G. P. Kochanski, Buchman S, L. Pollack, Y. M. Xiao, D. Kleppner, and T. J. Greytak. *Relaxation and recombination in spin-polarized atomic hydrogen*. Phys. Rev. Lett., **34**, 7670 (1986).
- [9] D. G. Fried, T. C. Killian, L. Willmann, D. Landhuis, S. C. Moss, D. Kleppner, and T. J. Greytak. *Bose-Einstein condensation of atomic hydrogen*. Phys. Rev. Lett., **81**, 3811 (1998).
- [10] E. L. Raab, M. Prentiss, A. Cable, S. Chu, and D. E. Pritchard. *Trapping of neutral sodium atoms with radiation pressure*. Phys. Rev. Lett., **59**, 2631 (1987).
- [11] K. B. Davis, M.-O. Mewes, M. A. Joffe, M. R. Andrews, and W. Ketterle. *Evaporative cooling of sodium atoms*. Phy. Rev. Lett., **74**, 5202 (1995).

-
- [12] K. B. Davis, M.-O. Mewes, M. R. Andrews, N. J. van Druten, D. S. Durfee, D. M. Kurn, and W. Ketterle. *Bose-Einstein Condensation in a gas of sodium atoms*. Phys. Rev. Lett., **75**, 3969 (1995).
- [13] C. C. Bradley, C. A. Sackett, J. J. Tollett, and R. G. Hulet. *Evidence of Bose-Einstein condensation in an atomic gas with attractive interactions*. Phys. Rev. Lett., **75**, 1687 (1995), *ibid.* **79**, 1170 (1997).
- [14] Y. Takasu, K. Maki, K. Komori, T. Takano, K. Honda, M. Kumakura, T. Yabuzaki, and Y. Takahashi. *Spin-Singlet Bose-Einstein Condensation of Two-Electron Atoms*. Phys. Rev. Lett., **91**, 040404 (2003).
- [15] M. R. Andrews, C. G. Townsend, H.-J. Miesner, D. S. Durfee, D. M. Kurn, and W. Ketterle. *Observation of Interference Between Two Bose-Einstein Condensates*. Science, **275**, 637 (1997).
- [16] B. P. Anderson and M. A. Kasevich. *Macroscopic Quantum Interference from Atomic Tunnel Arrays*. Science, **282**, 1686 (1998).
- [17] E. W. Hagley, L. Deng, M. Kozuma, J. Wen, K. Helmerson, S. L. Rolston, and W. D. Phillips. *A Well-Collimated Quasi-Continuous Atom Laser*. Science, **283**, 1706 (1999).
- [18] I. Bloch, T. W. Hänsch, and T. Esslinger. *Atom laser with a cw output coupler*. Phys. Rev. Lett., **82**, 3008 (1999).
- [19] M.-O. Mewes, M. R. Andrews, D. M. Kurn, D. S. Durfee, C. G. Townsend, and W. Ketterle. *Output Coupler for Bose-Einstein Condensed Atoms*. Phys. Rev. Lett., **78**, 582 (1997).
- [20] M.R. Andrews, D.M. Kurn, H.-J. Miesner, D.S. Durfee, C.G. Townsend, S. Inouye, and W. Ketterle. *Propagation of sound in a Bose-Einstein condensate*. Phys. Rev. Lett., **79**, 549 (1997). Erratum: Phys. Rev. Lett. **80**, 2967 (1998).
- [21] M. R. Matthews, B. P. Anderson, P. C. Haljan, D. S. Hall, C. E. Wieman, and E. A. Cornell. *Vortices in a Bose-Einstein Condensate*. Phys. Rev. Lett., **83**, 2498 (1999).
- [22] K. W. Madison, F. Chevy, W. Wohlleben, and J. Dalibard. *Vortex Formation in a Stirred Bose-Einstein Condensate*. Phys. Rev. Lett., **84**, 806 (2000).
- [23] O.M. Maragò, S. Hopkins, J. Arlt, E. Hodby, G. Hechenblaikner, and C.J. Foot. *Observation of the Scissors Mode and Evidence for Superfluidity of a Trapped Bose-Einstein Condensed Gas*. Phys. Rev. Lett., **84**, 2056 (2000).

-
- [24] M. Greiner, O. Mandel, T. Esslinger, T. W. Hänsch, and I. Bloch. *Quantum phase transition from a superfluid to a Mott insulator in a gas of ultracold atoms*. Nature, **415**, 39 (2002).
- [25] R. Dumke, M. Volk, T. Müther, F.B.J. Buchkremer, G. Birkl, and W. Ertmer. *Micro-optical Realization of Arrays of Selectively Addressable Dipole Traps: A Scalable Configuration for Quantum Computation with Atomic Qubits*. Phys. Rev. Lett., **89**, 097903 (2002).
- [26] M. Greiner, C. A. Regal, and D. S. Jin. *Emergence of a molecular Bose-Einstein condensate from a Fermi gas*. Nature, **426**, 537 (2003).
- [27] S. Jochim, M. Bartenstein, A. Altmeyer, G. Hendl, S. Riedl, C. Chin, J. H. Denschlag, and R. Grimm. *Bose-Einstein Condensation of Molecules*. Science, **302**, 2101 (2003).
- [28] M. W. Zwierlein, C. A. Stan, C. H. Schunck, S. M. F. Raupach, S. Gupta, Z. Hadzibabic, and W. Ketterle. *Observation of Bose-Einstein Condensation of Molecules*. Phys. Rev. Lett., **91**, 250401 (2003).
- [29] H. R. Thorsheim, J. Weiner, and P. S. Julienne. *Laser-induced photoassociation of ultracold sodium atoms*. Phys. Rev. Lett., **58**, 2420 (1987).
- [30] P. D. Lett, K. Helmerson, W. D. Phillips, L. P. Ratliff, S. L. Rolston, and M. E. Wagshul. *Spectroscopy of Na₂ by Photoassociation of Laser-Cooled Na*. Phys. Rev. Lett., **71**, 2200 (1993).
- [31] Roahn Wynar, R. S. Freeland, D. J. Han, C. Ryu, and D. J. Heinzen. *Molecules in a Bose-Einstein Condensate*. Science, **287**, 1016 (2000).
- [32] P. D. Lett, P. S. Julienne, and W. D. Phillips. *Photoassociative Spectroscopy of Laser-Cooled Atoms*. Annu. Rev. Phys. Chem., **46**, 423 (1995).
- [33] J. M. Vogels, C. C. Tsai, R. S. Freeland, S. J. J. M. F. Kokkelmans, B. J. Verhaar, and D. J. Heinzen. *Prediction of Feshbach resonances in collisions of ultracold rubidium atoms*. Phys. Rev. A, **56**, R1067 (1997).
- [34] A. Marte, T. Volz, J. Schuster, S. Dürr, G. Rempe, E.G.M. van Kempen, and B.J. Verhaar. *Feshbach Resonances in Rubidium 87: Precision Measurement and Analysis*. Phys. Rev. Lett., **89**, 283201 (2002).
- [35] T. W. Hänsch and A. Schawlow. *Cooling of Gases by Laser Radiation*. Opt. Commun., **13**, 68 (1975).
- [36] D. Wineland and H. Dehmelt. *Proposed $10^{14}\delta\nu/\nu$ Laser Fluorescence Spectroscopy on Tl^+ Mono-Ion Oscillator*. Bull. Am. Phys. Soc., **20**, 637 (1975).

-
- [37] D. Wineland and W. Itano. *Laser Cooling of Atoms*. Phys. Rev. A, **20**, 1521 (1979).
- [38] J. Dalibard and C. Cohen-Tannoudji. *Laser Cooling Below the Doppler Limit by Polarization Gradients - Simple Theoretical-Models*. J. Opt. Soc. Am. B, **6**, 2023 (1989).
- [39] A. Aspect, E. Arimondo, R. Kaiser, N. Vansteenkiste, and C. Cohen-Tannoudji. *Laser Cooling below the One-Photon Recoil Energy by Velocity-Selective Coherent Population Trapping*. Phys. Rev. Lett., **61**, 826 (1988).
- [40] M. Kasevich and S. Chu. *Laser Cooling Below a Photon Recoil with 3-Level Atoms*. Phys. Rev. Lett., **69**, 1741 (1992).
- [41] H. J. Metcalf and P. van der Straten. *Laser Cooling and Trapping*. Springer, 1999.
- [42] P. D. Lett, R. N. Watts, C. E. Tanner, S. L. Rolston, W. D. Phillips, and C. I. Westbrook. *Optical Molasses*. J. Opt. Soc. Am. B, **6**, 2084 (1989).
- [43] C. J. Pethick and H. Smith. *Bose-Einstein Condensation in Dilute Gases*. Cambridge University Press, 2002.
- [44] W. Ketterle and D. E. Pritchard. *Trapping and focussing Ground state Atoms with static fields*. Appl. Phys. B, **54**, 403 (1992).
- [45] J. R. Ensher. *The First Experiments with Bose-Einstein Condensation of ^{87}Rb* . PhD thesis, University of Colorado, 1998.
- [46] L. P. Pitaevskii. *Vortex lines in an imperfect Bose gas*. Sov. Phys. JETP, **451**, 13 (1961).
- [47] G. Baym and C. Pethick. *Ground-State Properties of Magnetically Trapped Bose-Condensed Rubidium Gas*. Phys. Rev. Lett., **76**, 6 (1996).
- [48] W. Ketterle and N. J. Van Druten. *Evaporative cooling of trapped atoms*. Advances in Atomic, Molecular, and Optical Physics, **37**, 181 (1996).
- [49] A. G. Martin, K. Helmerson, V. S. Bagnato, G. P. Lafyatis, and D. E. Pritchard. *rf Spectroscopy of Trapped Neutral Atoms*. Phys. Rev. Lett., **61**, 2431 (1988).
- [50] R. Grimm, M. Weidemüller, and Y. B. Ovchinnikov. *Optical Dipole Traps for Neutral Atoms*. Adv. At. Mol. Opt. Phys., **42**, 95 (2000).

-
- [51] J. Hecker Denschlag, J. E. Simsarian, H. Häffner, C. McKenzie, A. Browaeys, D. Cho, K. Helmerson, S. L. Rolston, and W. D. Phillips. *A Bose-Einstein condensate in an optical lattice*. J. Phys. B: At. Mol. Opt. Phys., **35**, 3095 (2002).
- [52] E. G. M. van Kempen, S. J. J. M. F. Kokkelmans, D. J. Heinzen, and B. J. Verhaar. *Inerisotope Determination of Ultracold Rubidium Interactions from Three High-Precision Experiments*. Phys. Rev. Lett., **88**, 093201 (2002).
- [53] A. J. Moerdijk, B. J. Verhaar, and A. Axelsson. *Resonances in ultracold collisions of ^6Li , ^7Li , and ^{23}Na* . Phys. Rev. A, **51**, 4852 (1995).
- [54] S. Inouye, M. R. Andrews, J. Stenger, H.-J. Miesner, D. M. Stamper-Kurn, and W. Ketterle. *Observation of Feshbach resonances in a Bose-Einstein condensate*. Nature, **392**, 151 (1998).
- [55] Ph. Courteille, R. S. Freeland, D. J. Heinzen, F. A. van Abeelen, and B. J. Verhaar. *Observation of a Feshbach Resonance in Cold Atom Scattering*. Phys. Rev. Lett., **81**, 69 (1998).
- [56] J. L. Roberts, N. R. Claussen, J. P. Burke, Jr., C. H. Greene, E. A. Cornell, and C. E. Wieman. *Resonant Magnetic Field Control of Elastic Scattering in Cold ^{85}Rb* . Phys. Rev. Lett., **81**, 5109 (1998).
- [57] V. Vuletić, A. J. Kerman, C. Chin, and S. Chu. *Observation of Low-Field Feshbach Resonances in Collisions of Cesium Atoms*. Phys. Rev. Lett., **82**, 1406 (1999).
- [58] T. Loftus, C. A. Regal, C. Ticknor, J. L. Bohn, and D. S. Jin. *Resonant Control of Elastic Collisions in an Optically Trapped Fermi Gas of Atoms*. Phys. Rev. Lett., **88**, 173201 (2002).
- [59] K. E. Strecker, G. B. Partridge, A. G. Truscott, and R. G. Hulet. *Formation and propagation of matter-wave soliton trains*. Nature, **417**, 150 (2002).
- [60] L. Khaykovich, F. Schreck, G. Ferrari, T. Bourdel, J. Cubizolles, L. D. Carr, Y. Castin, and C. Salomon. *Formation of a Matter-Wave Bright Soliton*. Science, **296**, 1290 (2002).
- [61] N. R. Newbury, C. J. Myatt, and C. E. Wieman. *S-wave elastic collisions between cold ground-state ^{87}Rb atoms*. Phys. Rev. A, **51**, R2680 (1995).
- [62] E. A. Donley, N. R. Claussen, S. L. Cornish, J. L. Roberts, E. A. Cornell, and C. E. Wieman. *Dynamics of collapsing and exploding Bose-Einstein condensates*. Nature, **412**, 295 (2002).

-
- [63] S. Dürr, T. Volz, A. Marte, and G. Rempe. *Observation of Molecules Produced from a Bose-Einstein Condensate*. Phys. Rev. Lett., **92**, 020406 (2004).
- [64] T. Volz, S. Dürr, S. Ernst, A. Marte, and G. Rempe. *Characterization of elastic scattering near a Feshbach resonance in ^{87}Rb* . Phys. Rev. A, **68**, 010702-1 (2003).
- [65] E. A. Burt, R. W. Ghrist, C. J. Myatt, M. J. Holland, E. A. Cornell, and C. E. Wieman. *Coherence, Correlations, and Collisions: What One Learns about Bose-Einstein Condensates from Their Decay*. Phys. Rev. Lett., **79**, 337 (1997).
- [66] K. Góral, T. Köhler, S. Gardiner, E. Tiesinga, and P. S. Julienne. *Adiabatic association of ultracold molecules via magnetic-field tunable interactions*. J. Phys. B: At. Mol. Opt. Phys., **37**, 3457 (2004).
- [67] D. R. Bates. *Quantum Theory - volume I. Elements*. ACADEMIC PRESS New York and London, 1961.
- [68] F. H. Mies, E. Tiesinga, and P. S. Julienne. *Manipulation of Feshbach resonances in ultracold collisions using time-dependent magnetic fields*. Phys. Rev. A, **61**, 022721 (2000).
- [69] T. Köhler and K. Burnett. *Microscopic quantum dynamics approach to the dilute condensed Bose gas*. Phys. Rev. A, **65**, 033601 (2002).
- [70] K. Xu, T. Mukaiyama, J. R. Abo-Shaeer, J. K. Chin, D. E. Miller, and W. Ketterle. *Formation of Quantum-Degenerate Sodium Molecules*. Phys. Rev. Lett, **91**, 210402 (2003).
- [71] S. Dürr. Personal communication.
- [72] C.J. Myatt, N.R. Newbury, R.W. Ghrist, S. Loutzenhiser, and C.E. Wieman. *Multiply loaded magneto-optical trap*. Opt. Lett., **21**, 290 (1996).
- [73] J. Yarwood. *High Vacuum Technique*. High Vacuum Series. Chapman and Hall LTD, 4th edition, 1967.
- [74] J. Arlt. *Experiments on Bose-Einstein Condensation*. PhD thesis, University of Oxford, 2000.
- [75] R. N. Watts and C.E. Wieman. *Manipulating atomic velocities using diode lasers*. Opt. Lett., **11**, 291 (1986).
- [76] D. Sesko, C.G. Fan, and C.E. Wieman. *Production of a cold atomic vapour using diode-laser cooling*. J. Opt. Soc. Am., **5**, 1225 (1988).

-
- [77] W. Demtröder. *Laser Spectroscopy*. Springer, 1996.
- [78] L. Ricci et al. *A compact grating-stabilized diode-laser for atomic physics*. Opt. Comm., **117**, 541 (1995).
- [79] J.L. Martin. *Magnetic Trapping and Cooling in Caesium*. PhD thesis, University of Oxford, 1997.
- [80] A. Thomas. *Towards BEC in Caesium!* First year report, University of Oxford, 2001.
- [81] K.I. Lee, J.A. Kim, H.R. Noh, and W. Jhe. *Single-beam atom trap in a pyramidal and conical hollow mirror*. Opt. Lett., **21**, 1177 (1996).
- [82] J. Arlt, O. Marago, S. Webster, S. Hopkins, and C.J. Foot. *A pyramidal magneto-optical trap as a source of slow atoms*. Opt. Comm., **157**, 303 (1998).
- [83] A. C. Hardy and F.H. Perrin. *The Principles of Optics*. McGraw-Hill Book Company, Inc., 1932.
- [84] C. J. Myatt. *Bose-Einstein Condensation Experiments in a dilute vapor of Rubidium*. PhD thesis, JILA - University of Colorado, Boulder, 1997.
- [85] M.-O. Mewes. *Bose-Einstein Condensation of Sodium Atoms*. PhD thesis, Massachusetts Institute of Technology, 1997.
- [86] H. Wu, E. Arimondo, and C. J. Foot. *Dynamics of evaporative cooling for Bose-Einstein condensation*. Phys. Rev. A, **56**, 560 (1997).
- [87] C. Orzel, A. K. Tuchman, M. L. Fenselau, M. Yasuda, and M. A. Kasevich. *Squeezed States in a Bose-Einstein Condensate*. Science, **291**, 2386 (2001).
- [88] D. M. Stamper-Kurn, M. R. Andrews, A. P. Chikkatur, S. Inouye, H.-J. Miesner, J. Stenger, and W. Ketterle. *Optical Confinement of a Bose-Einstein Condensate*. Phys. Rev. Lett., **80**, 2027 (1998).
- [89] M.-O. Mewes, M. R. Andrews, D. M. Stamper-Kurn, D. S. Durfee, C. G. Townsend, and W. Ketterle. *Output Coupler for Bose-Einstein Condensed Atoms*. Phys. Rev. Lett., **78**, 582 (1996).
- [90] B. D. Esry, C. H. Greene, and J. P. Burke Jr. *Recombination of Three Atoms in the Ultracold Limit*. Phys. Rev. Lett., **83**, 1751 (1999).
- [91] H. Suno, B. D. Esry, and C. H. Greene. *Recombination of Three Ultracold Fermionic Atoms*. Phys. Rev. Lett., **90**, 053202 (2003).
- [92] M. Stoll and T. Köler. *Production of three-body Efimov molecules in an optical lattice*. Cond-mat/0410765, (2004).

-
- [93] G. Smirne, K. Góral, and T. Köler *et al.* *Resonance enhanced three-body recombination in cold gases of ^{87}Rb : Experiment versus theory.* in preparation, (2005).
- [94] E. A. Donley, N. R. Claussen, S. L. Cornish, J. L. Roberts, Eric A. Cornell, and Carl E. Wieman. *Dynamics of collapsing and exploding Bose-Einstein condensates.* Nature, **412**, 295 (2001).
- [95] Y. Castin and R. Dum. *Bose-Einstein Condensates in Time Dependent Traps.* Phys. Rev. Lett., **77**, 5315 (1996).
- [96] D. McGloin, G.C. Spalding, H. Melville, W. Sibbett, and K. Dholakia. *Applications of spatial light modulators in atom optics.* Optics Express, **11**, 158 (2003).
- [97] V. Boyer, C.M. Chandrashekar, C.J. Foot, and Z.J. Laczik. *Dynamic optical trap generation using FLC SLMs for the manipulation of cold atoms.* Journal of Modern Optics, **51**, 2235 (2004).
- [98] A. Görlitz, J. M. Vogels, A. E. Leanhardt, C. Raman, T. L. Gustavson, J. R. Abo-Shaeer, A. P. Chikkatur, S. Gupta, S. Inouye, T. Rosenband, and W. Ketterle. *Realization of Bose-Einstein Condensates in Lower Dimension.* Phys. Rev. Lett., **87**, 130402 (2001).
- [99] P. Pedri *et al.* *Expansion of a Coherent Array of Bose-Einstein Condensates.* Phys. Rev. Lett., **87**, 220401 (2001).